

Advances in Civil Engineering

Landslide Hazard Assessment in Hillslopes Associated with Underground Mining

Lead Guest Editor: Shengli Yang

Guest Editors: Gaofeng Song, Dezhong Kong, Xinfeng Wang, and Zhanbo Cheng





**Landslide Hazard Assessment in Hillslopes
Associated with Underground Mining**

Advances in Civil Engineering

Landslide Hazard Assessment in Hillslopes Associated with Underground Mining

Lead Guest Editor: Shengli Yang

Guest Editors: Gaofeng Song, Dezhong Kong,
Xinfeng Wang, and Zhanbo Cheng



Copyright © 2021 Hindawi Limited. All rights reserved.

This is a special issue published in "Advances in Civil Engineering." All articles are open access articles distributed under the Creative Commons Attribution License, which permits unrestricted use, distribution, and reproduction in any medium, provided the original work is properly cited.






Chief Editor

Cumaraswamy Vipulanandan, USA










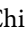



Associate Editors

Chiara Bedon , Italy
Constantin Chaliotis , Greece
Ghassan Chehab , Lebanon
Ottavia Corbi, Italy
Mohamed ElGawady , USA
Husnain Haider , Saudi Arabia
Jian Ji , China
Jiang Jin , China
Shazim A. Memon , Kazakhstan
Hossein Moayedi , Vietnam
Sanjay Nimbalkar, Australia
Giuseppe Oliveto , Italy
Alessandro Palmeri , United Kingdom
Arnaud Perrot , France
Hugo Rodrigues , Portugal
Victor Yepes , Spain
Xianbo Zhao , Australia

Academic Editors

José A.F.O. Correia, Portugal
Glenda Abate, Italy
Khalid Abdel-Rahman , Germany
Ali Mardani Aghabaglou, Turkey
José Aguiar , Portugal
Afaq Ahmad , Pakistan
Muhammad Riaz Ahmad , Hong Kong
Hashim M.N. Al-Madani , Bahrain
Luigi Aldieri , Italy
Angelo Aloisio , Italy
Maria Cruz Alonso, Spain
Filipe Amarante dos Santos , Portugal
Serji N. Amirkhanean, USA
Eleftherios K. Anastasiou , Greece
Panagiotis Ch. Anastasopoulos , USA
Mohamed Moafak Arbili , Iraq
Farhad Aslani , Australia
Siva Avudaiappan , Chile
Ozgur BASKAN , Turkey
Adewumi Babafemi, Nigeria
Morteza Bagherpour, Turkey
Qingsheng Bai , Germany
Nicola Baldo , Italy
Daniele Baraldi , Italy

Eva Barreira , Portugal
Emilio Bastidas-Arteaga , France
Rita Bento, Portugal
Rafael Bergillos , Spain
Han-bing Bian , China
Xia Bian , China
Huseyin Bilgin , Albania
Giovanni Biondi , Italy
Hugo C. Biscaia , Portugal
Rahul Biswas , India
Edén Bojórquez , Mexico
Giosuè Boscato , Italy
Melina Bosco , Italy
Jorge Branco , Portugal
Bruno Briseghella , China
Brian M. Broderick, Ireland
Emanuele Brunesi , Italy
Quoc-Bao Bui , Vietnam
Tan-Trung Bui , France
Nicola Buratti, Italy
Gaochuang Cai, France
Gladis Camarini , Brazil
Alberto Campisano , Italy
Qi Cao, China
Qixin Cao, China
Iacopo Carnacina , Italy
Alessio Cascardi, Italy
Paolo Castaldo , Italy
Nicola Cavalagli , Italy
Liborio Cavaleri , Italy
Anush Chandrappa , United Kingdom
Wen-Shao Chang , United Kingdom
Muhammad Tariq Amin Chaudhary, Kuwait
Po-Han Chen , Taiwan
Qian Chen , China
Wei Tong Chen , Taiwan
Qixiu Cheng, Hong Kong
Zhanbo Cheng, United Kingdom
Nicholas Chileshe, Australia
Prinya Chindaprasirt , Thailand
Corrado Chisari , United Kingdom
Se Jin Choi , Republic of Korea
Heap-Yih Chong , Australia
S.H. Chu , USA
Ting-Xiang Chu , China

Zhaofei Chu , China
Wonseok Chung , Republic of Korea
Donato Ciampa , Italy
Gian Paolo Cimellaro, Italy
Francesco Colangelo, Italy
Romulus Costache , Romania
Liviu-Adrian Cotfas , Romania
Antonio Maria D'Altri, Italy
Bruno Dal Lago , Italy
Amos Darko , Hong Kong
Arka Jyoti Das , India
Dario De Domenico , Italy
Gianmarco De Felice , Italy
Stefano De Miranda , Italy
Maria T. De Risi , Italy
Tayfun Dede, Turkey
Sadik O. Degertekin , Turkey
Camelia Delcea , Romania
Cristoforo Demartino, China
Giuseppe Di Filippo , Italy
Luigi Di Sarno, Italy
Fabio Di Trapani , Italy
Aboelkasim Diab , Egypt
Thi My Dung Do, Vietnam
Giulio Dondi , Italy
Jiangfeng Dong , China
Chao Dou , China
Mario D'Aniello , Italy
Jingtao Du , China
Ahmed Elghazouli, United Kingdom
Francesco Fabbrocino , Italy
Flora Faleschini , Italy
Dingqiang Fan, Hong Kong
Xueping Fan, China
Qian Fang , China
Salar Farahmand-Tabar , Iran
Ilenia Farina, Italy
Roberto Fedele, Italy
Guang-Liang Feng , China
Luigi Fenu , Italy
Tiago Ferreira , Portugal
Marco Filippo Ferrotto, Italy
Antonio Formisano , Italy
Guoyang Fu, Australia
Stefano Galassi , Italy

Junfeng Gao , China
Meng Gao , China
Giovanni Garcea , Italy
Enrique García-Macías, Spain
Emilio García-Taengua , United Kingdom
DongDong Ge , USA
Khaled Ghaedi, Malaysia
Khaled Ghaedi , Malaysia
Gian Felice Giaccu, Italy
Agathoklis Giaralis , United Kingdom
Ravindran Gobinath, India
Rodrigo Gonçalves, Portugal
Peilin Gong , China
Belén González-Fonteboa , Spain
Salvatore Grasso , Italy
Fan Gu, USA
Erhan Güneyisi , Turkey
Esra Mete Güneyisi, Turkey
Pingye Guo , China
Ankit Gupta , India
Federico Gusella , Italy
Kemal Hacıefendioğlu, Turkey
Jianyong Han , China
Song Han , China
Asad Hanif , Macau
Hadi Hasanzadehshooiili , Canada
Mostafa Fahmi Hassanein, Egypt
Amir Ahmad Hedayat , Iran
Khandaker Hossain , Canada
Zahid Hossain , USA
Chao Hou, China
Biao Hu, China
Jiang Hu , China
Xiaodong Hu, China
Lei Huang , China
Cun Hui , China
Bon-Gang Hwang, Singapore
Jijo James , India
Abbas Fadhil Jasim , Iraq
Ahad Javanmardi , China
Krishnan Prabhakan Jaya, India
Dong-Sheng Jeng , Australia
Han-Yong Jeon, Republic of Korea
Pengjiao Jia, China
Shaohua Jiang , China

MOUSTAFA KASSEM , Malaysia
Mosbeh Kaloop , Egypt
Shankar Karuppannan , Ethiopia
John Kechagias , Greece
Mohammad Khajehzadeh , Iran
Afzal Husain Khan , Saudi Arabia
Mehran Khan , Hong Kong
Manoj Khandelwal, Australia
Jin Kook Kim , Republic of Korea
Woosuk Kim , Republic of Korea
Vaclav Koci , Czech Republic
Loke Kok Foong, Vietnam
Hailing Kong , China
Leonidas Alexandros Kouris , Greece
Kyriakos Kourousis , Ireland
Moacir Kripka , Brazil
Anupam Kumar, The Netherlands
Emma La Malfa Ribolla, Czech Republic
Ali Lakirouhani , Iran
Angus C. C. Lam, China
Thanh Quang Khai Lam , Vietnam
Luciano Lamberti, Italy
Andreas Lampropoulos , United Kingdom
Raffaele Landolfo, Italy
Massimo Latour , Italy
Bang Yeon Lee , Republic of Korea
Eul-Bum Lee , Republic of Korea
Zhen Lei , Canada
Leonardo Leonetti , Italy
Chun-Qing Li , Australia
Dongsheng Li , China
Gen Li, China
Jiale Li , China
Minghui Li, China
Qingchao Li , China
Shuang Yang Li , China
Sunwei Li , Hong Kong
Yajun Li , China
Shun Liang , China
Francesco Liguori , Italy
Jae-Han Lim , Republic of Korea
Jia-Rui Lin , China
Kun Lin , China
Shibin Lin, China

Tzu-Kang Lin , Taiwan
Yu-Cheng Lin , Taiwan
Hexu Liu, USA
Jian Lin Liu , China
Xiaoli Liu , China
Xuemei Liu , Australia
Zaobao Liu , China
Zhuang-Zhuang Liu, China
Diego Lopez-Garcia , Chile
Cristiano Loss , Canada
Lyan-Ywan Lu , Taiwan
Jin Luo , USA
Yanbin Luo , China
Jianjun Ma , China
Junwei Ma , China
Tian-Shou Ma, China
Zhongguo John Ma , USA
Maria Macchiaroli, Italy
Domenico Magisano, Italy
Reza Mahinroosta, Australia
Yann Malecot , France
Prabhat Kumar Mandal , India
John Mander, USA
Iman Mansouri, Iran
André Dias Martins, Portugal
Domagoj Matesan , Croatia
Jose Matos, Portugal
Vasant Matsagar , India
Claudio Mazzotti , Italy
Ahmed Mebarki , France
Gang Mei , China
Kasim Mermerdas, Turkey
Giovanni Minafò , Italy
Masoomah Mirrashid , Iran
Abbas Mohajerani , Australia
Fadzli Mohamed Nazri , Malaysia
Fabrizio Mollaioli , Italy
Rosario Montuori , Italy
H. Naderpour , Iran
Hassan Nasir , Pakistan
Hossein Nassiraei , Iran
Satheeskumar Navaratnam , Australia
Ignacio J. Navarro , Spain
Ashish Kumar Nayak , India
Behzad Nematollahi , Australia

Chayut Ngamkhanong , Thailand
Trung Ngo, Australia
Tengfei Nian, China
Mehdi Nikoo , Canada
Youjun Ning , China
Olugbenga Timo Oladinrin , United Kingdom
Oladimeji Benedict Olalusi, South Africa
Timothy O. Olawumi , Hong Kong
Alejandro Orfila , Spain
Maurizio Orlando , Italy
Siti Aminah Osman, Malaysia
Walid Oueslati , Tunisia
SUVASH PAUL , Bangladesh
John-Paris Pantouvakis , Greece
Fabrizio Paolacci , Italy
Giuseppina Pappalardo , Italy
Fulvio Parisi , Italy
Dimitrios G. Pavlou , Norway
Daniele Pellegrini , Italy
Gatheeshgar Perampalam , United Kingdom
Daniele Perrone , Italy
Giuseppe Piccardo , Italy
Vagelis Plevris , Qatar
Andrea Pranno , Italy
Adolfo Preciado , Mexico
Chongchong Qi , China
Yu Qian, USA
Ying Qin , China
Giuseppe Quaranta , Italy
Krishanu ROY , New Zealand
Vlastimir Radonjanin, Serbia
Carlo Rainieri , Italy
Rahul V. Ralegaonkar, India
Raizal Saifulnaz Muhammad Rashid, Malaysia
Alessandro Rasulo , Italy
Chonghong Ren , China
Qing-Xin Ren, China
Dimitris Rizos , USA
Geoffrey W. Rodgers , New Zealand
Pier Paolo Rossi, Italy
Nicola Ruggieri , Italy
JUNLONG SHANG, Singapore


Nikhil Saboo, India
Anna Saetta, Italy
Juan Sagaseta , United Kingdom
Timo Saksala, Finland
Mostafa Salari, Canada
Ginevra Salerno , Italy
Evangelos J. Sapountzakis , Greece
Vassilis Sarhosis , United Kingdom
Navaratnarajah Sathiparan , Sri Lanka
Fabrizio Scozzese , Italy
Halil Sezen , USA
Payam Shafigh , Malaysia
M. Shahria Alam, Canada
Yi Shan, China
Hussein Sharaf, Iraq
Mostafa Sharifzadeh, Australia
Sanjay Kumar Shukla, Australia
Amir Si Larbi , France
Okan Sirin , Qatar
Piotr Smarzewski , Poland
Francesca Sollecito , Italy
Rui Song , China
Tian-Yi Song, Australia
Flavio Stochino , Italy
Mayank Sukhija , USA
Piti Sukontasukkul , Thailand
Jianping Sun, Singapore
Xiao Sun , China
T. Tafsirojjaman , Australia
Fujiao Tang , China
Patrick W.C. Tang , Australia
Zhi Cheng Tang , China
Weerachart Tangchirapat , Thailand
Xiixin Tao, China
Piergiorgio Tataranni , Italy
Elisabete Teixeira , Portugal
Jorge Iván Tobón , Colombia
Jing-Zhong Tong, China
Francesco Trentadue , Italy
Antonello Troncone, Italy
Majbah Uddin , USA
Tariq Umar , United Kingdom
Muahmmad Usman, United Kingdom
Muhammad Usman , Pakistan
Mucteba Uysal , Turkey

Ilaria Venanzi , Italy
Castorina S. Vieira , Portugal
Valeria Vignali , Italy
Claudia Vitone , Italy
Liwei WEN , China
Chunfeng Wan , China
Hua-Ping Wan, China
Roman Wan-Wendner , Austria
Chaohui Wang , China
Hao Wang , USA
Shiming Wang , China
Wayne Yu Wang , United Kingdom
Wen-Da Wang, China
Xing Wang , China
Xiuling Wang , China
Zhenjun Wang , China
Xin-Jiang Wei , China
Tao Wen , China
Weiping Wen , China
Lei Weng , China
Chao Wu , United Kingdom
Jiangyu Wu, China
Wangjie Wu , China
Wenbing Wu , China
Zhixing Xiao, China
Gang Xu, China
Jian Xu , China
Panpan , China
Rongchao Xu , China
HE YONGLIANG, China
Michael Yam, Hong Kong
Hailu Yang , China
Xu-Xu Yang , China
Hui Yao , China
Xinyu Ye , China
Zhoujing Ye, China
Gürol Yildirim , Turkey
Dawei Yin , China
Doo-Yeol Yoo , Republic of Korea
Zhanping You , USA
Afshar A. Yousefi , Iran
Xinbao Yu , USA
Dongdong Yuan , China
Geun Y. Yun , Republic of Korea

Hyun-Do Yun , Republic of Korea
Cemal YİĞİT , Turkey
Paolo Zampieri, Italy
Giulio Zani , Italy
Mariano Angelo Zanini , Italy
Zhixiong Zeng , Hong Kong
Mustafa Zeybek, Turkey
Henglong Zhang , China
Jiupeng Zhang, China
Tingting Zhang , China
Zengping Zhang, China
Zetian Zhang , China
Zhigang Zhang , China
Zhipeng Zhao , Japan
Jun Zhao , China
Annan Zhou , Australia
Jia-wen Zhou , China
Hai-Tao Zhu , China
Peng Zhu , China
QuanJie Zhu , China
Wenjun Zhu , China
Marco Zucca, Italy
Haoran Zuo, Australia
Junqing Zuo , China
Robert Černý , Czech Republic
Süleyman İpek , Turkey


Contents

Research on Technology of Supporting in Super-Large Section Cut in Working Face with Large Mining Height

Zhicheng Ren and Minghui Zuo 







Research Article (6 pages), Article ID 3304049, Volume 2021 (2021)

Research on the Rock Pressure Behavior at Close-Distance Island Working Faces under Deep Goaf

Shoulong Ma 


Research Article (11 pages), Article ID 4714012, Volume 2021 (2021)

Research on the Influence Mechanism of the High-Steep Slope on the Deformation Characteristics of Bridge Substructure

Yufang Zhang , Hongyu Liu , Jian Li , Jiaming Li , Qidi Huang , and Xianjie Ma 


Research Article (13 pages), Article ID 9037680, Volume 2021 (2021)

Study on the Stability of Slopes Reinforced by Composite Vegetation Combined with a Geogrid under Rainfall Conditions

Qizhi Hu , Yong Zhou, and Gaoliang Tao


Research Article (10 pages), Article ID 8058009, Volume 2021 (2021)

Welding Deformation of Hydraulic Support Measurements by Using FBG Sensors

Shangyu Du , Guofa Wang, Yajun Xu, Ying Ma, Desheng Zhang, Qiang Ma, and Xingtong Yue

Research Article (10 pages), Article ID 5405597, Volume 2021 (2021)

Numerical Simulation of Surface Movement and Deformation Caused by Underground Mining with Complex Stratigraphic Boundary

Liang Wang, Chao He, Songjun Cui, and Feifei Wang 

Research Article (14 pages), Article ID 9967071, Volume 2021 (2021)

Research Article

Research on Technology of Supporting in Super-Large Section Cut in Working Face with Large Mining Height

Zhicheng Ren and Minghui Zuo 

School of Energy and Mining, China University of Mining and Technology (Beijing), Beijing 100083, China

Correspondence should be addressed to Minghui Zuo; 263232856@qq.com

Received 8 May 2021; Accepted 17 August 2021; Published 14 October 2021

Academic Editor: Dezhong Kong

Copyright © 2021 Zhicheng Ren and Minghui Zuo. This is an open access article distributed under the Creative Commons Attribution License, which permits unrestricted use, distribution, and reproduction in any medium, provided the original work is properly cited.

For the support problem of the super-large section cut in working face with large mining height, the 1105 cut pilot chamber of Zhaogu No. 2 Mine, the roof strata structure detection and the strata movement rule research were conducted. The results prove that concentrate fracture area, gradually sparse fracture area, and rare fracture area regularly distributed from the surface to the deep area of the roof of 1105 cut, and less fracture exists in the rock stratum of roof above 3.5 m, and the stratum of roof within the range of 4–6 m is stable. Authors propose the long bolt and cable combined supporting technology and optimized the design plan applying theoretical calculation and computer numerical simulation. The scheme has been applied in the field of the 1105 super-large section cut in Zhaogu No. 2 Mine. The monitoring results show that the scheme can effectively control surrounding rock of roadway, and the support with long bolt has good effectiveness.

1. Introduction

As the coal mine high yield and high efficient working face advance and further improve the degree of mechanization, especially the use of large mining heights, working face equipment is becoming larger and larger, and the open cut span of working face is also increasing, which increases the difficulty of support and maintenance. The support problem of the super-large cross-section open cut has become an important problem in the field of coal mine safety [1–11]. In terms of technology, the research on the prevention and control measures of rock burst has also been constantly improved, and the pressure relief method has made rapid progress. A variety of methods have been successfully used to prevent rock burst at home and abroad [10, 12, 13]. In this study, the large-diameter boreholes in the coal roadway pressure relief mechanism and reasonable parameters further research will be conducted. At the same time, it analyzes the layout direction, diameter, hole spacing, hole depth parameters, and their reasonable combinations of large-diameter boreholes, so that to provide extremely important theoretical support for the practical application and

popularization of large-diameter borehole pressure relief technology and has great practical application value.

2. Project Overview

The 1105 working face is the first large mining height working face of the Zhaogu No. 2 Mine, with an elevation of –636 to –618 m, which is a typical deep buried layout. The No. 2 coal seam is mainly mined at the 1,105 large mining height working face. The average thickness of the No. 2 coal seam is 6.32 m. The false roof is mainly mudstone and carbonaceous mudstone less than 0.5 m, which are only scattered in this area and generally fall with the mining. The thickness of the direct roof is generally 1.0–6.5 m, which is dominated by mudstone roof and accounts for 70% of the coal bearing area. The distribution area of sandstone is about 20% of the coal bearing area and sandy mudstone accounts for 15% of the coal bearing area. The old roof thickness is 0.94–19.85 m, and the average thickness is 7.46 m siltstone. The mechanical strength of the roof sandstone is medium, and the mudstone siltstone is medium-low, which belongs to the roof with medium-low management degree. The floor of

the second coal seam is dominated by mudstone and sandy mudstone, with a thickness of 9.1–17.27 m, with an average of 12.84 m. The comprehensive coal and rock layer of the working face is shown in Figure 1.

The cutout of the 1105 working surface is a rectangular section with a design length of 180 m, a height of 4.62 m, a normal section width of 9.2 m, and a nose and tail section width of 10.2 m. During tunneling construction, the small section guide adit shall be tunneled first, the width of which is 4.8 m, and the support shall be expanded to the normal section before installation.

3. Supporting Mechanism of 1105 Super-Large Section Open Cut

3.1. Fine Detection of Roof Rock Structure. Thickness of roof strata and the intensity have an important effect on roof stability, but due to the complexity of coal-forming environment and geological changes, different positions of roof rock strata thickness and strength can produce a very big change; in order to get the roof strata structure features of 1105 cut, thirteen roof detection boreholes are uniformly arranged in the guide tunnel of the off-cut, and the rock structure peeping instrument is used to detect the roof layering, layer thickness, rock cracks, and lithology to provide a basis for the design of the later off-cut support. The fine detection results of the roof rock formations show that the lithology within 10 m above the roof of the 1105 notch is relatively simple, the lower part is sandy mudstone with low strength and low cohesion, and the upper part is fine-grained sandstone; along the axial direction of the notch, the roof sandy mudstone layers at both ends are thinner than the middle part of the cut, and the ends of the fine-grained sandstone layers are slightly thicker than the middle. There are many cracks in the shallow part of the roof. The closer the roof is to the surface, the more fractured the surrounding rock is. From the surface of the roof to the deep part, there are different characteristics, such as dense fracture zone, sparse fracture zone, and rare fracture zone. In most boreholes, the fractures above 3.5 m are not particularly obvious. Based on the above rock structure characteristics, the length of anchor rod should be increased after the brush cross-section, and the anchorage end should be extended above the fissure dense area to ensure the stability of the roof in the shallow fissure dense area.

3.2. Movement Law of Rock Stratum on the Roof of Guide Tunnel. After the excavation of the guide tunnel, the original design plan is adopted for the combined support of bolts and cables. The bolt specifications are 20 mm × 2400 mm rebar resin bolts, the row spacing between the top bolts is 800 mm × 800 mm, and the anchor cable specification is 21.6 mm × 8250 mm anchor cable, with a row spacing of 1,600 mm × 1,600 mm. After the excavation of the roadway, the stress of the surrounding rock on the roof is transferred and concentrated, and the layered roof is prone to separation failure after

deformation. In order to grasp the separation failure area of the guide tunnel of the cutoff cut and judge the support effect, it is the bolt (cable) parameter that optimizes and determines the reasonable length of the anchor rod to obtain basic field data. Set up rock movement measurement stations on the roof of the guide tunnel and install 2.0 m, 4.0 m, 6.0 m, and 10.0 m at each measurement station. Observe base points at different depths. The monitoring curve of multibase displacement in the roof of the guide adit is shown in Figure 2.

The monitoring data show that the overall deformation of the roof increases rapidly after the opening of the open-hole guide adit and gradually slows down. After 20 d, the deformation of the roof is stable at about 150 mm. The deformation of the roof mainly occurs within 4 m of the depth of the roof, accounting for about 80 of the overall deformation of the roof. Among them, the displacement of roof in the range of 2–4 m is about 50 mm because the common short bolt is not long enough to control the stability of rock stratum in this range. The displacement of the roof rock in the range of 4 m is close to coincide with the displacement of the rock in the range of 6 m, and the displacement change trend is synchronized, indicating that the rock formation in the range of 4–6 m from the roof of the 1105 cutoff cut is relatively stable. The anchor end of the rod is extended to a range of 4–6 m, and the rock formation with a large displacement within the range of 4 m is suspended on the stable rock formation. Mechanically calculate stability of roof rock beam. After roadway excavation, the roof will bend and sink to a certain extent under the action of overlying strata load. With the increase of roadway section, the total subsidence of the roof will increase and the stability will be greatly reduced. The ultimate span formula of the simply supported beam of material mechanics was used to calculate the subsidence amount of the roadway roof, and a coordinate system is established as shown in Figure 3. The deflection at the left and right hinge supports of the boundary condition was equal to zero.

The bending moment equation of the beam is

$$M(X) = \frac{ql}{2}x - \frac{1}{2}qx^2, \quad (1)$$

where M is the bending moment of the beam, q is the load of overlying strata, and l is the rock beam span.

Substitute formula (1) into the approximate differential equation of the deflection curve of a straight beam:

$$EI\omega'' = -M(X), \quad (2)$$

where ω'' is the second derivative of beam deflection, E is the elastic modulus of roof rock mass, and I is the moment of inertia of the roof rock beam.

The deflection curve equation of the roof beam is

$$\omega = \frac{qx}{24EI}(l^3 - 2lx^2 + x^3). \quad (3)$$

Therefore, it is judged that the maximum deflection must be in the middle of the beam span, that is, at $x = l/2$. At this time,

legend	Thickness (m)	Lithology	Description
	10.37	Siltstone	Dark gray, Containing plant fossils, Argillaceous cement
	6.5	Mudstone, Sandy mudstone	Dark gray, Containing plant fossils and a large number of siderite nodules
	6.32	Coal	Black, Blocky, Metallic luster
	7.3	Sandy mudstone	Black gray, Contains plant fossils and nodules
	5.41	Mudstone	Dark gray, Containing plant fossils, Silica cement

FIGURE 1: Comprehensive histogram of working face.

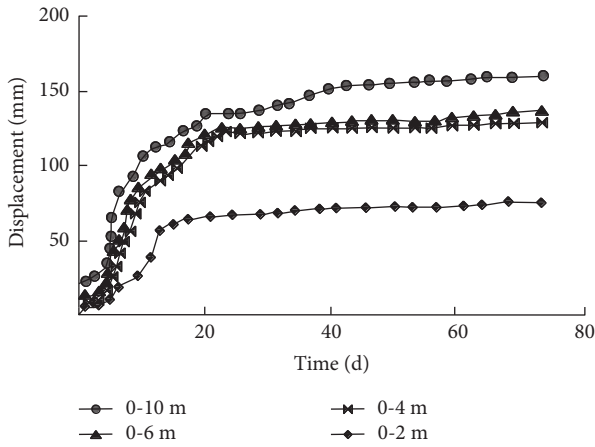


FIGURE 2: Multibase point displacement monitoring curve in the deep part of the guide tunnel roof.

$$\omega_{\max} = \omega|_{x=l/2} = \frac{5ql^4}{384EI} \quad (4)$$

As the height of the roof rock beam remains unchanged, the moment of inertia of the roof rock beam is proportional to the span l of the rock beam, namely,

$$I = \frac{h^3}{12}l \quad (5)$$

Substituting equation (5) into equation (4), that is, the maximum deflection of a rock beam with a roadway roof is

$$\omega_{\max} = \frac{5ql^3}{32Eh^3} \quad (6)$$

It can be seen from equation (6) that the maximum sinking deformation of the roadway roof is proportional to the third power of the roadway span l . For the 1105 cutoff, the previous monitoring data show that the deformation of the guide way roof is about 150 mm, which is extended to normal. After the cross-section, the deformation of the top plate of the open cut will increase by 6–9 times, and the safety of the top

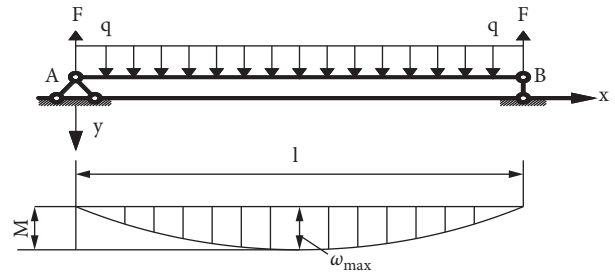


FIGURE 3: Mechanics model of simply supported beam of roadway roof.

plate cannot be guaranteed. Therefore, for the support of the super-large cross-section open cut, it is necessary to adopt measures such as erecting a column to reduce the span.

4. Large Section Open Cut Support Plan

4.1. Numerical Calculation of Long Bolt Support Scheme. Use FLAC numerical simulation software to calculate and compare the supporting effect of the long bolt support scheme and the original guide tunnel support scheme and further study the deformation displacement and stress distribution of the surrounding rock of the super-large section cutout. Establish a calculation model for the 1105 cut, the cut length is 180 m, and the average thickness of the coal seam is 6.32 m. The cutout section is rectangular, 9.20 m wide, and 4.72 m high. Both sides of the cut are solid coal. The calculation model selects the x -axis direction as the advancing direction along the working face and the y -axis direction as the vertical direction. In the x -axis direction, take 50 m to the left from the center line of the roadway and 50 m to the right. In the direction of the y -axis, take 36.5 m toward the top rock layer, add a uniform load to the upper boundary, and take 30.0 m toward the bottom rock layer. The constitutive relationship of the surrounding rock of the cut hole adopts the Mohr–Coulomb model. The mechanical parameters of coal and rock in the model are given in Table 1. Figure 4 is

TABLE 1: Mechanical parameters of rock and coal in the calculation model.

Rock formation name	Density (kg m^{-3})	Shear modulus (GPa)	Bulk modulus (GPa)	Cohesion (MPa)	Internal friction angle($^{\circ}$)	Tensile strength (MPa)
Medium sandstone	2420	9.477	10.264	12.18	40.33	3.536
Coarse sandstone	2392	4.450	5.632	8.37	44.52	1.758
2-1 coal	1450	2.130	6.389	4.2	32	1.050
Sandy mudstone	2560	3.23	4.18	6.51	36	1.12
Mudstone	2593	2.02	3.70	5.01	38	0.64

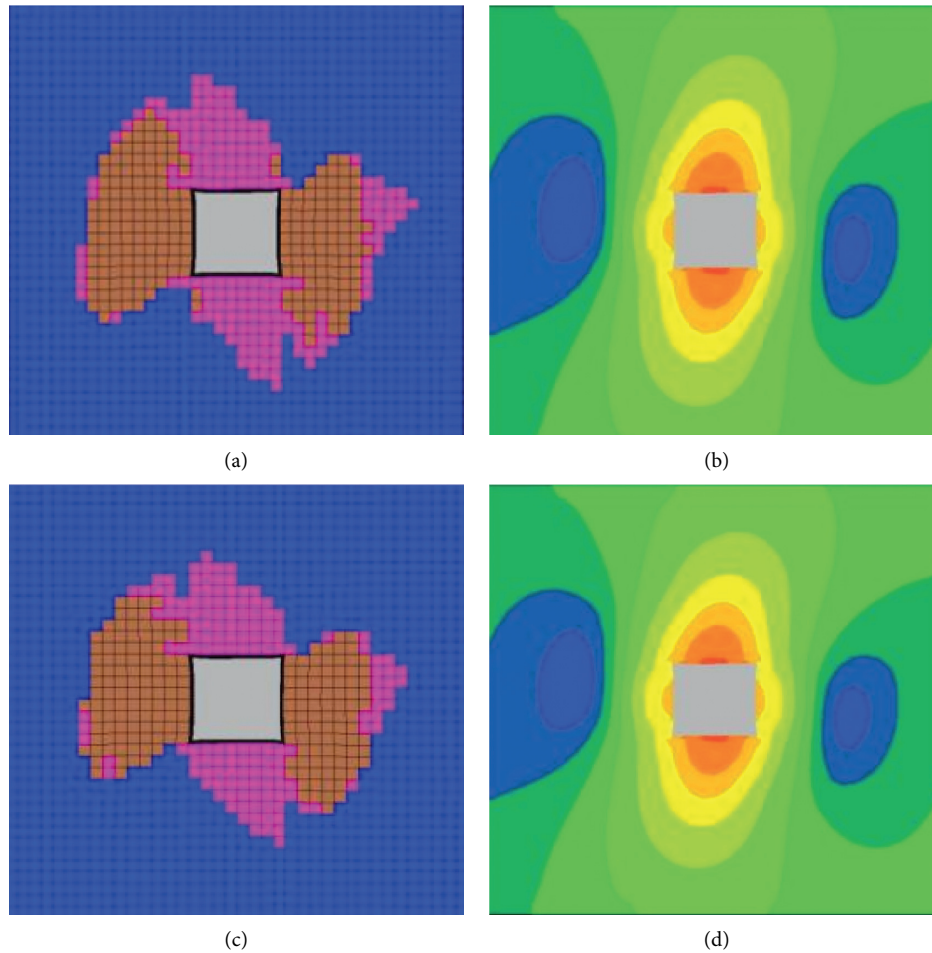


FIGURE 4: Simulation of the plastic zone and stress distribution of different lengths of bolt support in the surrounding rock. (a) Ordinary bolt support scheme shaping area. (b) Stress distribution of ordinary bolt support scheme. (c) Long bolt support scheme shaping area. (d) Stress distribution of long bolt support scheme.

a simulation diagram of the shaping zone and stress distribution in the surrounding rock with different length bolts.

Figures 4(a) and 4(b) show that the maximum shaping area of the top plate in the middle of the original support plan is 5 m, and the shaping range of the top plates near the two banks is gradually smaller than the middle. Due to the many cracks in the shallow part of the eye roof and the decrease in rock strength, the stress at 2 m from the roof reaches 10 MPa, and the stress at 3.2–6 m reaches 20 MPa. Figure 4(c) shows that the plastic failure of the top plate near the two sides is only 2 m, and the plastic failure of the top

plate in the middle of the cut reaches 4 m, which is 1 m less than the plastic failure range when ordinary bolts are used (Figure 4(d)). It shows that as the distance between the top plates increases, the stress rises significantly. The stress rises to 10 MPa in the range of 1–2 m and reaches 22.5 MPa above 6.2 m.

The above analysis shows that the surrounding rock shaping zone of the long bolt support scheme is smaller than the surrounding rock shaping zone of the original scheme. The ordinary bolts are all located in the plastic zone, while the long bolts can be anchored to the stable rock formation outside the plastic zone.

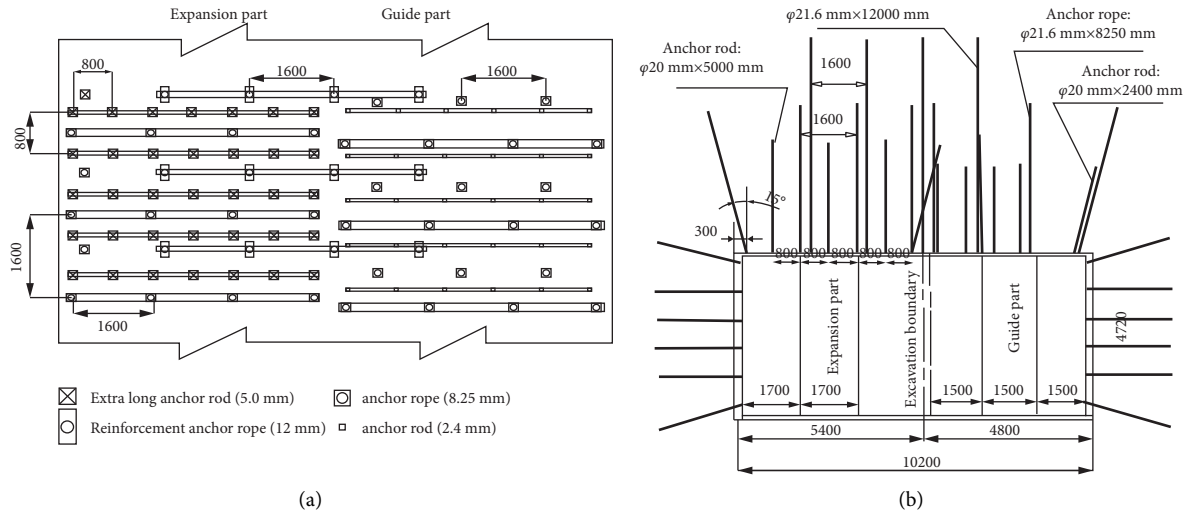


FIGURE 5: Layout of 1105 incisional eye support. (a) Layout plan of 1105 notch roof support. (b) Section view of top plate support layout of 1105 cut.

4.2. 1105 Super-Large Section Open Cut Support Plan. According to the results of fine detection of roof strata and numerical simulation of rock strata movement, the support scheme of 1105 super-large section cut holes with superlong bolt and anchor cable combined with rows of single pillar is determined.

- (1) Roof support: the roof of the cutoff guide tunnel adopts 21.6 mm to construct 6 anchor rods, as shown in Figure 5(a). In addition, two rows of single pillars are erected to support the roof. The top plate after the cutout is enlarged, uses 20 mm × 5000 mm superlong bolts with a row spacing of 800 mm × 800 mm, and each row at the top is constructed with 7 bolts; the anchor cables are in the middle of the cutout except for the anchor cables used on the roof of the guide tunnel. In addition, a 16 mm × 12,000 mm reinforced anchor cable is installed, with a row spacing of 1,600 mm × 1,600 mm, and a pallet of 12 mm × 400 mm × 400 mm, 12 mm × 200 mm × 200 mm × 200 mm steel plates, and 50 mm × 200 mm. Use wooden pads together. At the same time, erect two rows of single pillars to support the roof.
- (2) Lane support: the bolt specifications are 20 mm × 2400 mm rebar resin bolts, with a row spacing of 700 mm × 800 mm, and each row is constructed with 6 bolts. As shown in Figure 5(b), the pallet is made of W-shaped steel belt and 10 mm × 150 mm. The 150 mm anchor rod tray is used in conjunction with the anchor rod and steel ladder to hit the stubble mesh. The metal mesh is welded with 5.6 mm steel bars, the mesh size is 900 mm × 1700 mm, the mesh is overlapped by 100 mm, and each grid is tied with 14[#] lead wire.
- (3) Supplementary materials: each top bolt uses one Z2360 resin anchoring agent and one CK2360 resin anchoring agent; each anchor bolt uses one Z2345

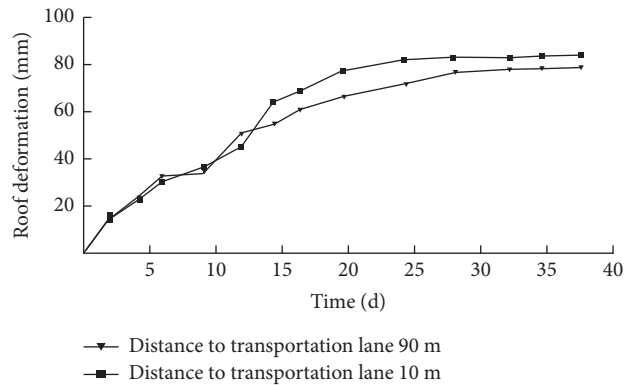


FIGURE 6: Deformation curve of the top plate of the open cut.

resin anchoring agent and one CK2345 resin anchoring agent; each anchor used two pieces of Z2360 resin anchoring agent and two pieces of CK2360 resin anchoring agent. The steel ladder is made of 14 mm round steel bars, the length of the steel ladder is 4160 mm, and the width is 70 mm.

5. Support Effect Monitoring

5.1. Displacement Monitoring of Open Cut Roof. In order to master the activity rule and supporting effect of the surrounding rock controlled by the long bolt and anchor cable supporting scheme and to provide data for the further improvement and optimization of supporting parameters in the future, the surface displacement of surrounding rock was observed during the construction process of extending the wall to the normal section. It can be seen from Figure 6 that after the secondary construction of the cutoff cut adopts the long anchor rod and the anchor cable support scheme, the overall roof deformation is small, and the displacement of the cutoff cut near the end of the mining roadway is greater than the top displacement in the middle of the cutoff cut and

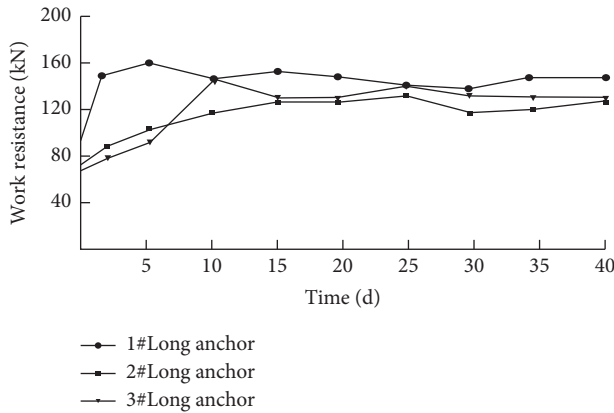


FIGURE 7: Working resistance curve of long anchor rod.

is closed to the end of the transportation roadway. The deformation becomes stable when the deformation reaches about 90 mm, and the roof deformation in the middle of the cut (90 m away from the transportation lane) becomes stable when it reaches 75 mm, which is less than the deformation of the guide tunnel roof of the cut (about 150 mm).

5.2. Simulation Diagram of the Plastic Zone and Stress Distribution Generated in the Rock. During the construction process from the cut to the normal section, the support resistance of the superlong bolts used was monitored. In Figure 7, the 1[#], 2[#], and 3[#] long bolts are the supporting resistance curves of the long bolts at the center of the cut at 10 m, 90 m, and 150 m away from the transportation roadway. The initial anchoring force of the extralong bolt is in the range of 50–100 kN, and it starts to receive the force stably when it reaches about 100–150 kN, and the overall supporting effect is good.

6. Conclusion

- (1) According to the fine detection of the rock structure and the study on the law of rock strata movement, the shallow fractures in the roof of the super-large section 1105 of Zhaogu No. 2 mine densely developed, the fractures above 3.5 m are gradually sparse, and there is basically no separation in the ceiling within the range of 4–6 m. In order to ensure the stability of the rock strata, long bolts should be used to anchor the shallow surrounding rocks to the stable rock strata.
- (2) Superlong bolt combined with anchor cable support technology effectively controls the surrounding rock deformation of the super-large cross-section in Zhaogu No. 2 mine, solving the support problem of the super-large cross-section in Zhaogu No. 2 mine.
- (3) The superlong bolt combined with anchor cable support technology is suitable for the roadway with great difficulty in surrounding rock control, such as the intersection of roadway with large broken

overhanging roof area in the shallow section of large section. This technology has strong pertinence and wide application scope.

Data Availability

The data used to support the findings of this study are included within the article.

Conflicts of Interest

The authors declare that they have no conflicts of interest.

References

- [1] Q. Liu and G. Xie, "Research and application of anchor mesh (cable) support for large cross-section cut holes in deep wells," *China Coal*, vol. 35, no. 7, 2009.
- [2] H. Cui and Y. Hu, "Open-open cut support plan for large mining height working face," *Coal Mine Safety*, vol. 44, no. 2, 2013.
- [3] H. Wang, Y. Yang, and J. Xi, "Research and application of anchor mesh (cable) support technology for long-span cut-off holes with composite roof," *China Coal*, vol. 2011, no. 2, pp. 59–62, 2011.
- [4] J. Li, A. Li, and G. Wang, "Research on bolt support technology for large section open-cut coal roadway," *Coal Engineering*, no. 3, 2010.
- [5] H. Wang, Y. Chen, and D. Zhang, "Combined support and effect analysis of large section open-open cut," *China Coal*, no. 9, 2010.
- [6] S. Xie, F. He, and S. Zhang, "Combined support technology of open-cut truss and anchor cable for large-section composite mudstone roof," *China Mining*, vol. 17, no. 9, 2008.
- [7] L. Xing, *Research on Bolt (cable) Support Technology for Large-Span Open-Cut Roadway*, Xi'an University of Science and Technology, Xi'an, China, 2008.
- [8] Y. Wang, F. Wei, and J. Bai, "Large-section open-cut support technology for fully mechanized mining face under the goaf," *Coal Science and Technology*, vol. 39, no. 6, 2011.
- [9] J. Wang, S. Yang, W. Wei, J. Zhang, and Z. Song, "Drawing mechanisms for top coal in longwall top coal caving (LTCC): a review of two decades of literature," *International Journal of Coal Science Technology*, 2021.
- [10] D. Z. Kong, S. J. Pu, Z. H. Cheng, G. Y. Wu, and Y. Liu, "Coordinated deformation mechanism of the top coal and filling body of gob-side entry retaining in a fully mechanized caving face," *International Journal of Geomechanics*, vol. 21, no. 4, Article ID 04021030, 2021.
- [11] J. F. Lou, F. Q. Gao, J. H. Yang et al., "Characteristics of evolution of mining-induced stress field in the longwall panel: insights from physical modeling," *International Journal of Coal Science Technology*, 2021.
- [12] Z. Jiang, K. Lei, and D. Liu, "Bolt and cable support technology for thick-top coal and large-span open-off cut," *Coal Mine Safety*, vol. 43, no. 2, 2012.
- [13] H. Liu, *Mechanics of Materials*, Higher Education Press, Beijing, China, 4th edition, 2003.

Research Article

Research on the Rock Pressure Behavior at Close-Distance Island Working Faces under Deep Goaf

Shoulong Ma ^{1,2}

¹School of Civil Engineering and Architecture, Anhui University of Science and Technology, Huainan, Anhui 232001, China

²China Coal Xinji Energy Co.,Ltd., Huainan, Anhui 232001, China

Correspondence should be addressed to Shoulong Ma; 2020100046@aust.edu.cn

Received 15 April 2021; Revised 3 August 2021; Accepted 21 August 2021; Published 20 September 2021

Academic Editor: Dezhong Kong

Copyright © 2021 Shoulong Ma. This is an open access article distributed under the Creative Commons Attribution License, which permits unrestricted use, distribution, and reproduction in any medium, provided the original work is properly cited.

In order to realize the safe and efficient mining of the short-distance isolated island working face under the deep goaf area, the 120502 isolated island working face of Liuzhuang Mine was taken as the engineering background. The method of combining numerical simulation and field measurement were used comprehensively to systematically simulate and study the spatial evolution of the stress field, plastic strain field, and fracture field of coal rock during the mining process. The leading support pressure and the vertical displacement of the roof in the overlapping section and noncoinciding section of the isolated working face and the goaf above were measured on site. The results are that the peak value of the advanced support pressure of the overlap section and the nonoverlapping section is 10 m before the coal wall of the working face; the advanced support pressure of the nonoverlapping section is 33.3 MPa, and the vertical displacement of the roof is 300 mm. The advanced support pressure and the vertical displacement of the roof in the noncoincidence section were significantly higher than those in the coincidence section of 18.2 MPa and 210 mm. The results are consistent with those predicted by numerical simulation. This provides theoretical support for the safe mining of the 120502 isolated island working face in Liuzhuang Mine and, at the same time, provides a reference for the study of similar working faces in other domestic mining areas.

1. Introduction

As the mining of coal resources in our country continues to move to the depths, due to the influence of geological conditions and the need for safe mining in the mines, it is inevitable that deep mine isolated islands are formed [1–4]. The coal rock masses in many mines have a certain tendency to impact, so the mining of isolated island working faces will encounter more complicated safety problems. Due to the open space on both sides of the isolated working face, the surrounding rock of the roadway is under a high-stress environment for a long time. As a result, the pressure of the mine becomes obvious, and the surrounding rock is deformed and damaged seriously [5–7]. It is difficult to support and maintain the two lanes and the open-off cut. The adjacent rock mass is in a rheological state after being destroyed and affected by dynamic pressure. Therefore, the behavior of mine pressure is complicated, which affects the

safe advancement of the working face [8]. To this end, researchers have conducted a lot of research on the behavior of rock pressure on the isolated island working face and rock burst problems.

Liu et al. [9] and Lu and Shi [10] analyzed the support pressure distribution characteristics of the ultralong-isolated island working face and the rock pressure behavior when the island working face crosses the fault structure. Wang et al. [11] established a thin plate mechanics model and analyzed the distribution behavior of the roof bending moment of the isolated island working face. Wang et al. [12, 13] studied the behavior of rock pressure in the short-walled coal pillar working face of an isolated island. Zhao et al. [14] studied the behavior of rock pressure in a typical coal seam island face in western China. Yang et al. [15] comprehensively considered overlying rock movement, geological structure, mining and space, and other factors and classified isolated working faces based on scour prevention. The isolated island working face

is divided into six types: full mining, insufficient mining, full-insufficient mining, three-dimensional, “recessive,” and compound type. In order to carry out the prevention and control of rock burst in different types of isolated island working faces, Dou [16, 17] proposed the detection and prediction and control technology of rock burst hazard in isolated island working face [18–20]. Wang et al. [21] analyzed the roof rupture height of the isolated island working face and the temporal and spatial distribution characteristics of microseismic events in the “square” area of the working face. Zhang et al. [22] used elastic plate theory to analyze the elastic energy value released during the fracture of the hard roof and used FLAC^{3D} numerical simulation to divide the high-stress area during the mining face. At the same time, according to the fractal theory, the internal correlation between the time distribution and spatial distribution of microseismic events and rock bursts was analyzed.

The above research studies have analyzed the appearance behaviors of rock pressure in different types of isolated island working faces and the prevention and control of rock bursts and have achieved good results. However, there is little research on island working faces under some complex conditions, especially those under the goaf. Based on the engineering background of 120502 isolated island working face in Liu Zhuang Coal Mine, this paper analyzes the behavior of underground pressure on the isolated island working face under the goaf of the deep close coal seam group through numerical simulation and field measurement.

2. Project Overview

The research working face is 120502 isolated island working face of Liu Zhuang Coal Mine. 120502 isolated island working face is located in the first level and second mining area. The south of the working face is the goaf of 120503 working face, the north is near the goaf of 120501 working face, and the above is the 6-1 and 8 coal goaf. Also, the vertical distance between the overlying 6-1# coal seam goaf and the 5# coal seam is 18 m, which is an isolated island working face under the short-distance goaf. The specific spatial position relationship is shown in Figure 1.

The 120502 working face is a monoclinic structure with an average dip angle of 13.0°, the coal thickness of the working face is 0.98 ~ 5.58 m, and the average thickness is 4.05 m. 120502 working face 5 coal false roof is not developed, the direct roof is mudstone, the upper part contains a small amount of sandy content, and the average thickness is 8.73 m. The main roof is fine sandstone. The geological histogram of the coal roof and floor of the working face is shown in Figure 2. This working face is a low-gas working face, and the coal seam is easy to combust spontaneously.

3. Numerical Simulation

In order to simulate the stress and deformation characteristics of the overlying strata in different spatial layers during the mining process and to reproduce the spatial change process of the entire overlying strata movement and

deformation, this paper uses FLAC^{3D} software to carry out a numerical simulation.

3.1. Model Building. A numerical model is established on the fully mechanized mining face of the 120502 isolated island with main goafs on the left, right, and upper sides. The model is 550 m long, 360 m wide, and 200 m high. The Mohr–Coulomb constitutive model is adopted for coal and rock mass, and its physical and mechanical parameters are shown in Table 1. The characteristics of the top and bottom of the working face are shown in Figure 2. Displacement boundary conditions are applied around the model, and the upper part of the model is free boundary conditions. A vertical stress of 25.1 MPa is applied at the top of the model, a stress of 30.2 MPa is applied at the bottom, and the surrounding stress is 42.3 MPa. According to the geological and ground stress test report of the working face, considering the elevation of the working face and the weight of the model, a vertical stress of 9 MPa was applied to the top of the model. The elastoplastic model is adopted, and the Mohr–Coulomb failure criterion is selected. The specific mechanical parameters of the main coal and rock layers are shown in Table 1.

3.2. Simulation Scheme. In the process of numerical simulation, in order to correctly simulate the stress, displacement, and fracture deformation characteristics of the surrounding rock of the stope caused by the stopping of the isolated working face, the model reaches the initial stress balance state under the given ground stress and boundary conditions. According to the sequence of the stope, the 120501, 120601, and 120503 working faces were excavated to construct a “three-sided” isolated island working face. The stopping of the 120502 mining working face is performed step by step. The stopping distances are, respectively, 80 m, 130 m, 180 m, and 240 m, and each excavation is designed to be 3000 steps. The distribution characteristics of stress, displacement, and plastic zone during the mining process are studied from the two directions of working face inclination and alignment direction. And, the distribution cloud map is quantified, so as to conduct in-depth research on the deformation characteristics of the overlying rock fractures during the stopping process of the isolated working face.

3.3. Simulation Result Analysis

3.3.1. Analysis of Evolution Characteristics of Mining Stress Field. After the model starts excavating, the stress distribution characteristics of the central coal rock mass in the inclined direction at the coal wall position at different advancing distances are shown in Figure 3. The pressure relief area in the inclined direction moves upward in an arch shape as the mining distance increases and gradually merges into one body. The coal pillar on the right side of the working face has a high degree of stress concentration, and the stress concentration factor has been increased from 2.54 to 4.41. Because the coal pillar on the left is in the pressure relief

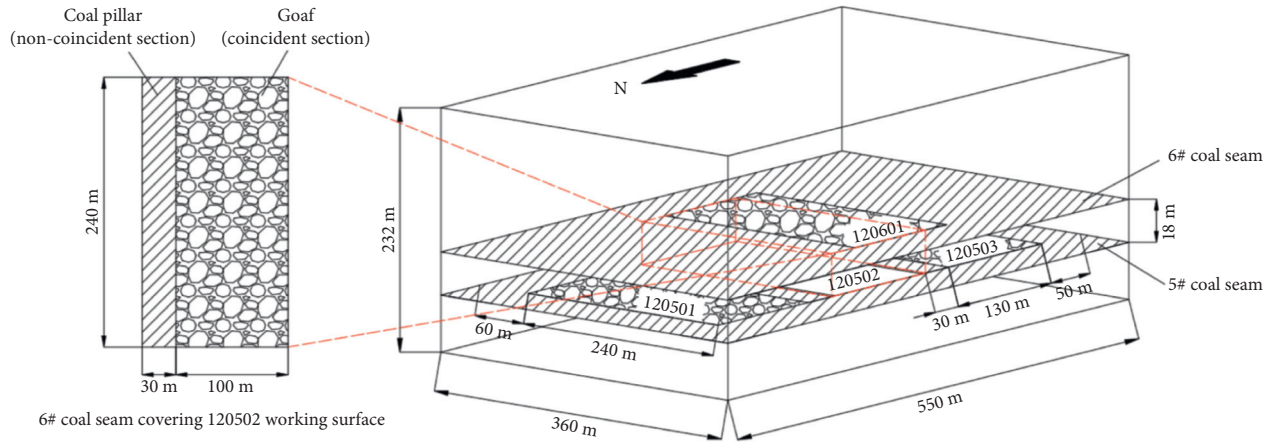


FIGURE 1: The spatial position relationship of each working face in the mining area.

Column	Rock name	Thickness (m)
	Mudstone	4.15
	Fine sandstone	4.20
	Sandy mudstone	5.10
	Siltstone	2.70
	Mudstone	2.00
	Fine sandstone	1.70
	Mudstone	2.22
	Fine sandstone	4.00
	6# coal seam	1.50
	Fine sandstone	9.40
	Mudstone	8.73
	5# coal seam	4.05
	Mudstone	1.45
	Medium-fine sandstone	13.6

FIGURE 2: Geological histogram of coal roof and floor.

TABLE 1: Physical and mechanical parameters of rock mass used in calculation.

Rock formation name	Bulk density, γ (kg/m ³)	Bulk modulus, K (GPa)	Shear modulus, G (GPa)	Cohesion, c (MPa)	Internal friction angle, φ (°)	Tensile strength, σ_t (MPa)
Middle-fine sandstone	2580	5.6	4.2	8	38	3.5
Siltstone	2680	5.6	4.2	8	38	3.5
5 coal	1410	1.73	0.82	0.18	20	0.2
6-1 coal	1390	2.0	0.88	0.42	24	0.3
Fine sandstone	2800	16.04	12.02	3.47	43	4.96
Mudstone	2567	4.3	2.8	0.7	30	1.68

range of the upper goaf, and the stress concentration is relatively weak.

Figure 4 shows the vertical stress distribution cloud diagram in the middle of the goaf in the alignment direction when advancing at different distances. It can be seen from

Figure 1 that the 120502 working face and the 120601 working face are staggered in the horizontal direction. At the square of the working face, affected by the mining of 5th coal, the vertical stress distribution range of the floor rock is enlarged. The concentrated stress inside the coal body at the

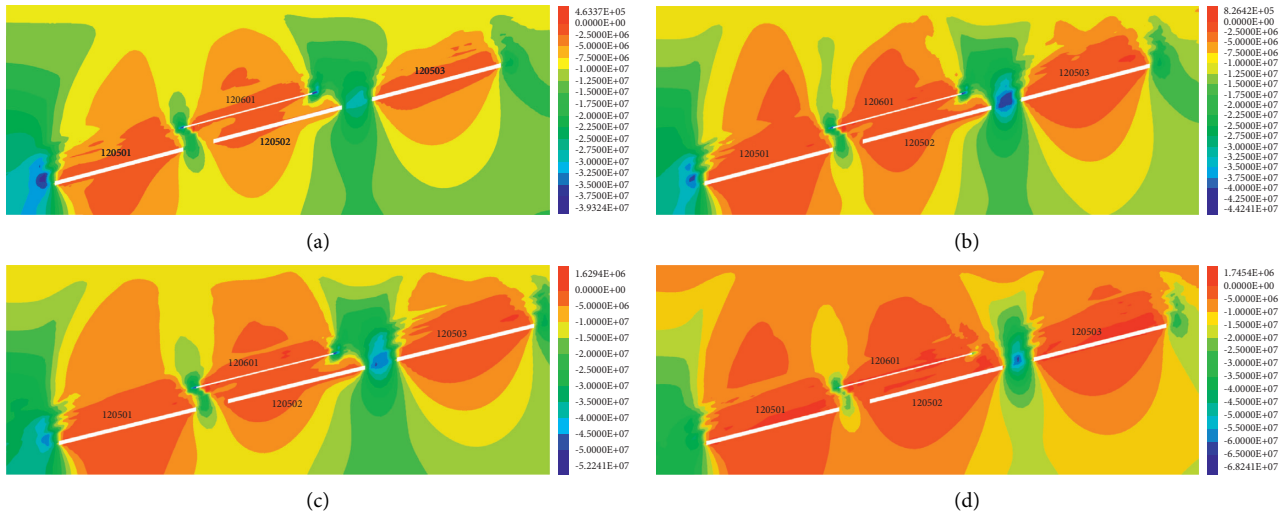


FIGURE 3: Cloud diagram of vertical stress distribution (inclination direction). (a) The working face advances 80 m, (b) the working face advances 130 m, (c) the working face advances 180 m, and (d) the working face advances 240 m.

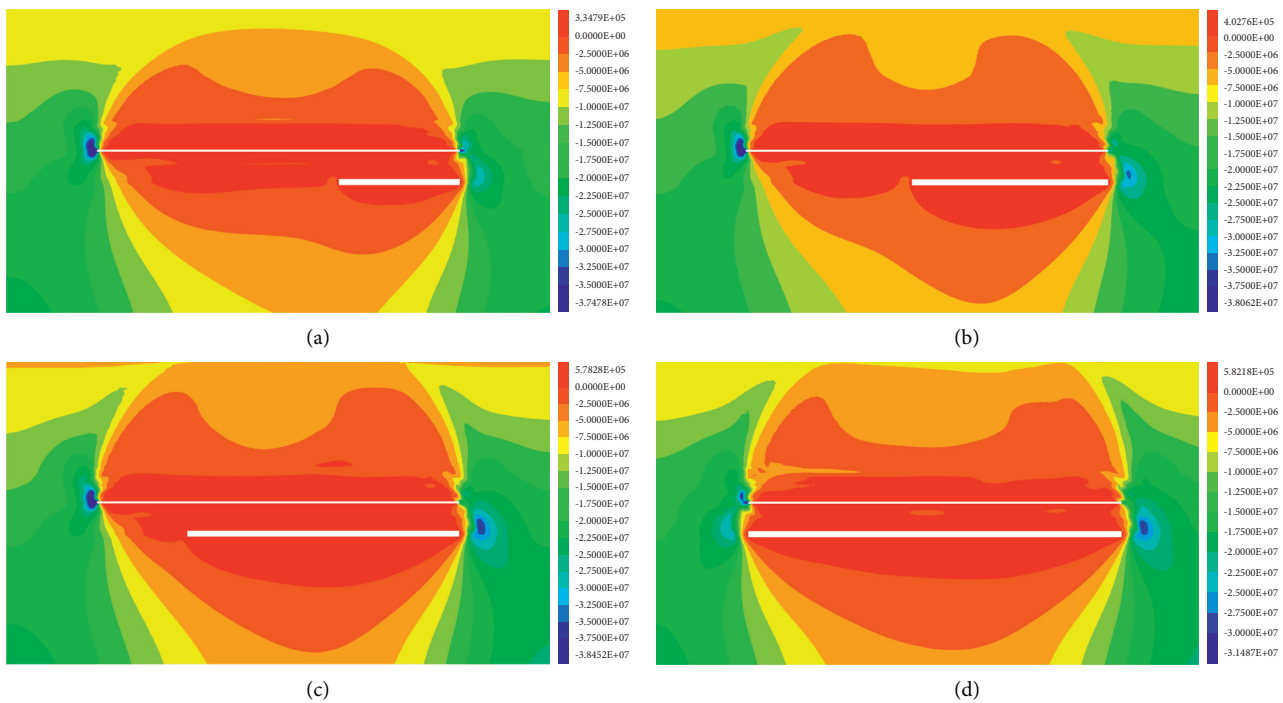


FIGURE 4: Vertical stress distribution cloud diagram (alignment direction): (a) the working face advances 80 m, (b) the working face advances 130 m, (c) the working face advances 180 m, and (d) the working face advances 240 m.

open-off cut gradually shifted from the 6th coal to the 5th coal, showing that the concentrated stress at the end of the 6th coal weakened and the concentrated stress at the 5th coal end increased. The floor is affected by the upper coal mining, and the front of the working face is in the mutual influence area between the pressure relief zone and the concentrated stress zone, and the concentrated stress is not large. When the working face advances to 240 m, the pressure at the end of coal 6 is released. The stress is concentrated at the end of

the lower layer coal 5, which increases the concentrated stress and increases the degree of damage.

The overburden strata have basically similar changes in the alignment and inclination directions. The stress concentration area and the stress reduction area are also basically the same, and they are continuously moved and expanded in an arch shape to form connections with other mining areas. The main goals on the left, right, and above all have an impact on the deformation of the overlying rock in

the goaf, but the upper main goaf has the greatest disturbance to it.

It can be seen from Figure 5 that, in the alignment direction, in the section overlapping with the upper goaf, the stress concentration areas are behind the open-off cut and in front of the working face. When the mining distance does not exceed 240 m, the distribution in front of the working face will first decrease and then increase. When the mining distance of the working face reaches 240 m, the distribution of “horizontal three areas” appears. The support pressure in front of the working face is increasing, and the distance between the peak support pressure and the coal wall is stable at about 10 m. In the noncoincident zone, it can be seen from Figure 6 that the stress concentration area remains unchanged, and the peak stress concentration is also equivalent under different advancing distances. Compared with the coincident section, the peak support pressure in the front of the working face under the same advance distance is larger. Comparing the two sections, it can be seen that the overburden stress distribution characteristics of the stope in the direction of the coincident and noncoincident sections are basically the same. The areas of stress concentration are both behind the open-off cut and in front of the working face, and the coal rock masses nearby are subject to greater stress, resulting in compression and destruction.

3.3.2. Analysis of Change Characteristics of Mining Displacement Field. Figure 7 reflects the vertical displacement change curve in the direction of the 120502 and 120601 working faces at different advancing distances in the overlapping sections. The direction of the vertical displacement in the section that coincides with the upper goaf in the alignment direction changes from downward to upward, and the vertical upward displacement peak remains stable. The change curve in the noncoincident zone is shown in Figure 8. The upper main goaf area has a great influence on the vertical displacement. The peak value of the vertical displacement increases with the increase of the mining distance, and the vertical displacement of the overlying strata in the mined-out area is downward during the whole advancement process.

From the vertical displacement curve during the advancing process of the working face, it can be seen that the vertical displacement of the overburden under different advancing distances forms the largest sinking area in the middle of the mined-out area, resulting in stress concentration in the area behind the open-off cut and near the working front.

It can be seen from Figure 9 that, during the mining process of the working face, the horizontal displacement increases continuously with the advance of the working face in the alignment direction. The changing graphics show curved sinking and symmetrical, with the center of symmetry in the middle of the goaf. The horizontal displacement changes strongly behind the open-off cut and in the goaf area in front of the working face. The horizontal deformation of

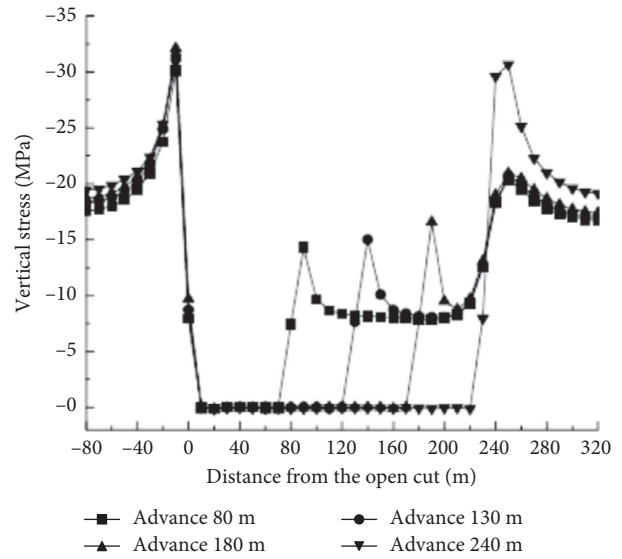


FIGURE 5: The vertical stress distribution curve of the first overlying layer (coincident section).

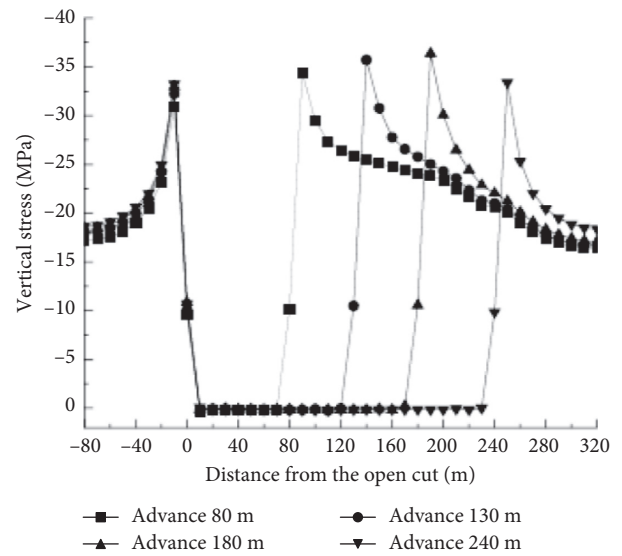


FIGURE 6: Vertical stress distribution curve of the first overlying layer (noncoincident section).

the overlying rock is relatively large, and the overlying rock is subjected to the combined action of horizontal stretching and compression, resulting in more fully developed cracks.

3.3.3. Analysis of Change Characteristics of Overlying Rock Plastic Zone. Figure 10 shows the development of the plastic zone in inclined direction when the working face is advanced at different distances. The closer to the working face, the greater the failure of coal and rock mass. H is the development height of the fracture zone, which is 101 m, 119 m, 126 m, and 130 m, respectively. When the upper part of coal reaches a certain height, it basically maintains a stable state. With the advance of the working face, the working face is in

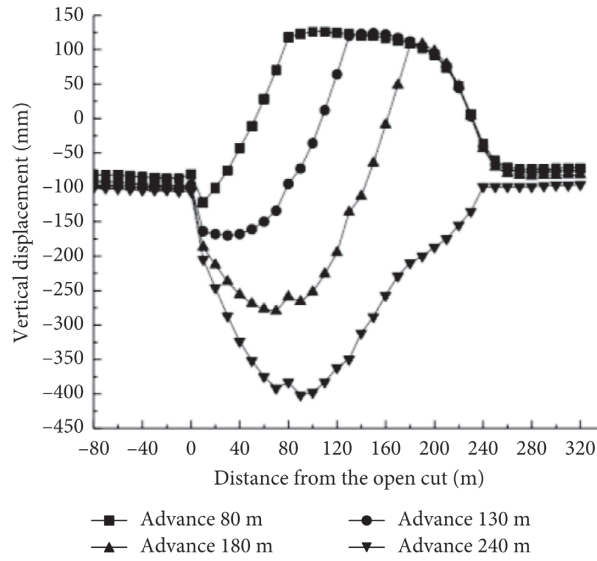


FIGURE 7: Vertical displacement distribution curve of the first overlying layer (coincident section).

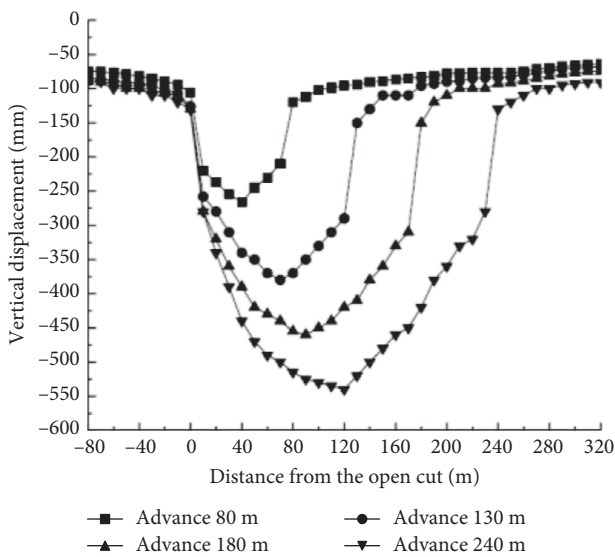


FIGURE 8: Vertical displacement distribution curve of the first overlying layer (noncoincident section).

the state of nonuniform expansion and dynamic development and gradually intersects with other plastic areas of the goaf. The plastic zones of multiple working faces are interconnected, the rock mass above the roof is in the tensile and compressive stress zone, and the surrounding rock cracks in the goaf are fully developed.

3.3.4. Determination of the Height Range of the Two Zones of the Overlying Strata. The stress discrimination method is used to divide the height range of the caving zone, the fracture zone, and the bending subsidence zone formed by the movement and deformation of the overlying rock during the mining process. The relationship between the principal stress in the middle position of the alignment and

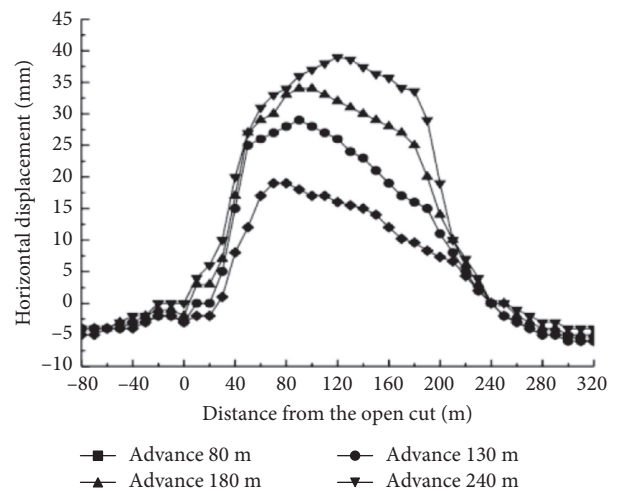


FIGURE 9: Horizontal displacement distribution curve of the first overlying layer (middle position).

the inclination directions and the distance of the roof of the goaf when the working face in the middle position of the overburden strata is mined at different distances is shown in Figure 11 and 12. As the advancing distance of the working face increases, the heights of both the caving zone and the fracture zone show a slight increase trend. In the alignment direction, the height of the caving zone ranges from 6.2 to 8.7 m, and the height of the fracture zone ranges from 33.5 to 38.6 m. In the inclination direction, the height of the caving is in the range of 6.5 to 9.2 m, and the height of the fracture zone is in the range of 34.8 to 40.5 m.

4. On-Site Measurement and Analysis

In order to further study the influence of the three-side goaf area in the mining process of the 120502 working face,

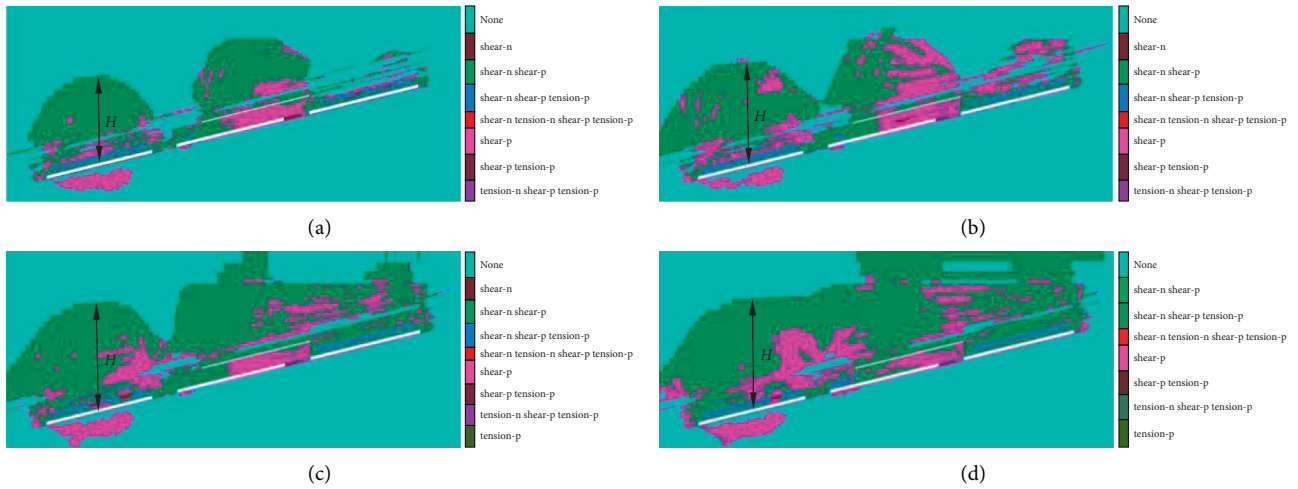


FIGURE 10: Trend of the plastic zone in the inclination direction: (a) the working face advances 80 m, (b) the working face advances 130 m, (c) the working face advances 180 m, and (d) the working face advances 240 m.

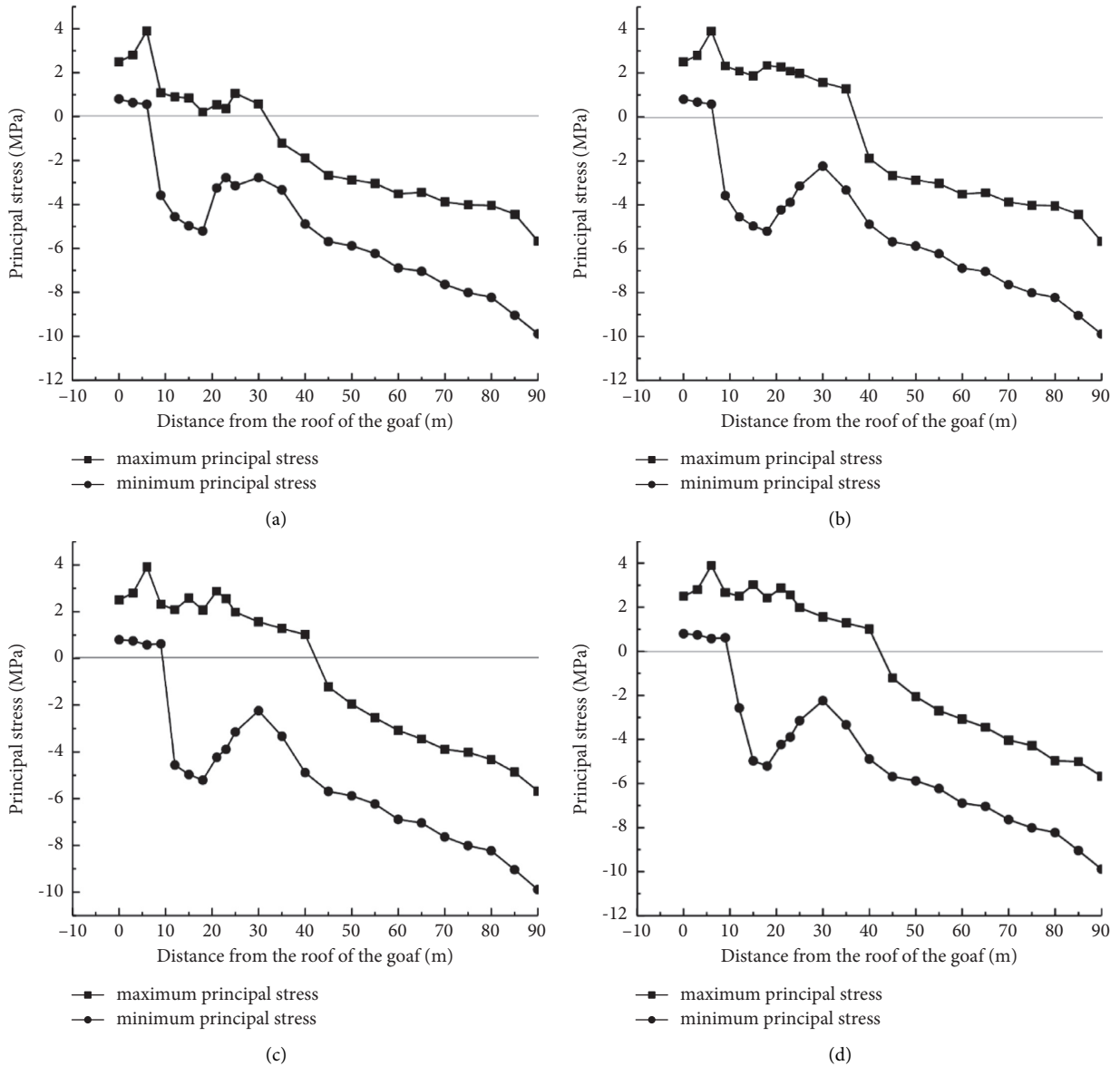


FIGURE 11: Variation curve of principal stress and the distance from the roof of the goaf (alignment direction): (a) the working face advances 80 m, (b) the working face advances 130 m, (c) the working face advances 180 m, and (d) the working face advances 240 m.

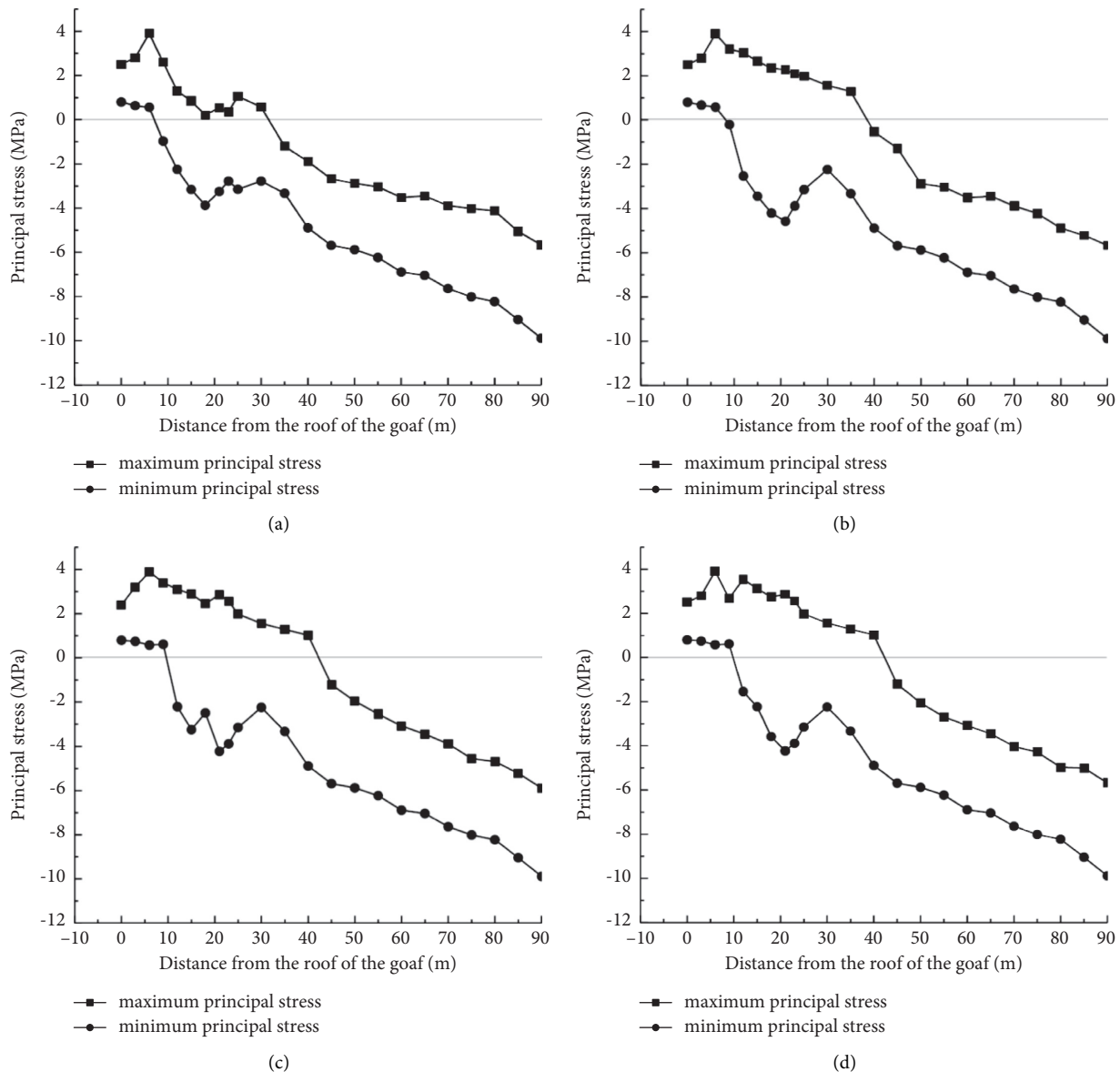


FIGURE 12: The variation curve of principal stress and the distance from the roof of the goaf (inclination direction): (a) the working face advances 80 m, (b) the working face advances 130 m, (c) the working face advances 180 m, and (d) the working face advances 240 m.

analyze the behavior of the appearance of rock pressure in the overlapping and noncoinciding sections with the upper goaf area, and verify the accuracy of the numerical simulation stress and strain results, on-site monitoring of the leading support pressure and the displacement of the roadway roof at 120502 island working face was conducted.

4.1. Measuring Point Layout and Monitoring Method. The length of the 120502 working face is 400 m. After fully considering the impact of the open-off cut and the stop line to protect the coal pillars, three measurement points for both stress monitoring and displacement monitoring of the working face are, respectively, set up in the transportation roadway and the return air roadway at both ends of the

working face. They are located at 100 m, 200 m, and 300 m away from the working face, respectively. The borehole stress gauge was used to measure the advance supporting pressure of the working face, and the roof separation gauge was used to measure the displacement of the surrounding rock of the overlying roof of the roadway.

4.2. Analysis of Monitoring Results of Two Roadways. Figure 13 shows the change curve of the leading support pressure at different advancing distances during the field measurement of the working face. The peaks of the leading support pressure of the working face in the coincident and noncoincident sections are located 10 m in front of the coal wall. In the overlap section, affected by the pressure relief of the upper goaf, the peak value of the leading support

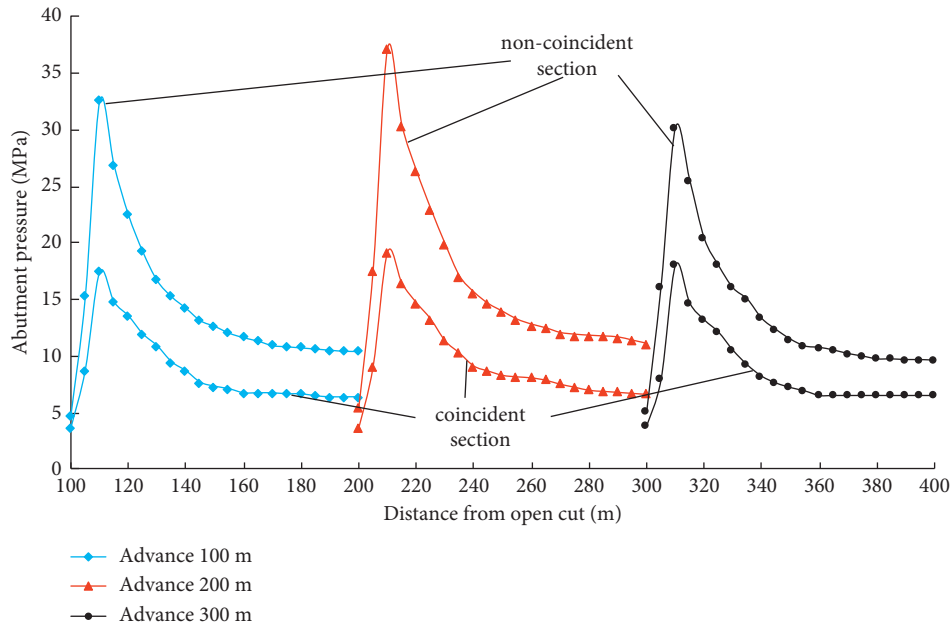


FIGURE 13: The change curve of the leading support pressure.

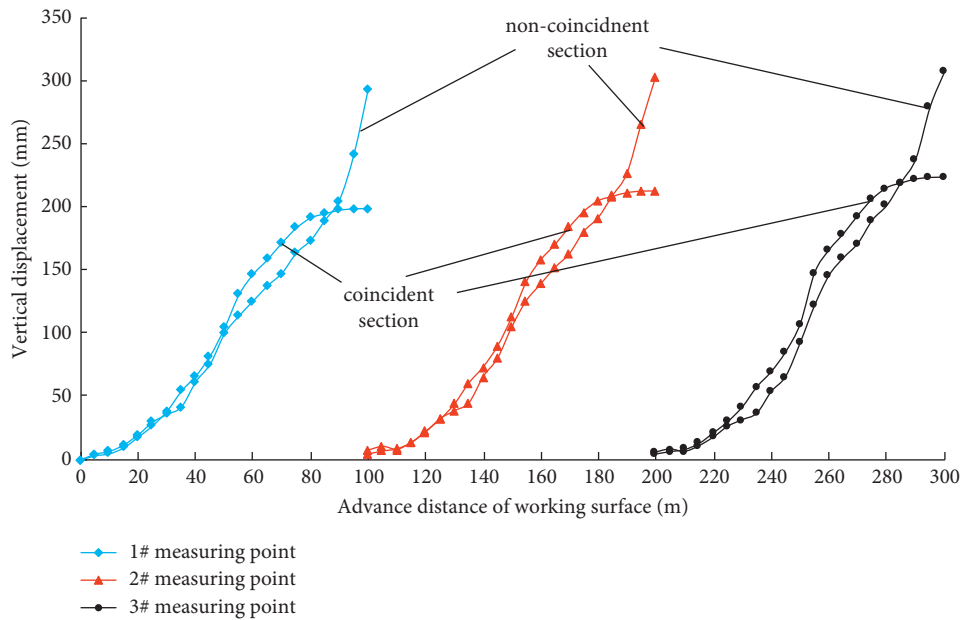


FIGURE 14: Roof displacement variation curve.

pressure is between 17.5 and 19.2 MPa, with an average of 18.2 MPa. The peak range of the leading support pressure in the noncoincident section is between 30.2 and 37.1, with an average of 33.3 MPa, which is larger than the coincident zone and consistent with the numerical simulation.

The measured vertical displacement curve of the roof of the roadway is shown in Figure 14. In the overlap section, the maximum displacement of the top plate is about 210 mm. The roof displacement of the non-coincident section is obviously larger than that of the coincident section. The displacement is about 300 mm, and it is not stable. It has a tendency to continue to

increase as the working face advances, which is consistent with the simulation result.

5. Conclusions

- (1) During the excavation of isolated island working face, the stress distribution presents the following characteristics. In the inclination direction, the pressure relief area expands with an arch upward movement as the mining distance increases and merges into a “saddle shape”. In the alignment direction, in the section coincident with the upper

goaf, the stress concentration area is behind the open-off cut and in front of the working face. The vertical stress first decreases and then increases with the increase of the mining distance and, finally, presents a “horizontal three-zone” distribution. The support pressure in front of the working face is increasing, and the distance between the peak support pressure and the coal wall is stable at about 10 m. In the noncoincident zone, the stress concentration area remains unchanged, and the peak stress concentration is also equivalent. However, under the same advancing distance, the peak support pressure in front of the work is higher.

- (2) The roof displacement has the following characteristics. In the alignment direction, in the section that overlaps with the upper goaf, the vertical displacement direction of the overlying rock strata in the goaf changes from downward to upward, and the peak displacement remains stable. In the noncoincidence section, the vertical displacement of the overlying strata in the goaf is downward, and the peak value is increasing. The horizontal displacement increases continuously with the advancement of the working face in the alignment direction. The overlying rock is subjected to the combined action of horizontal stretching and compression, and thus, the cracks develop more fully. The failure range of the plastic zone is a “saddle shape” with a nonuniform expansion trend and an upward dynamic development. The plastic zone on both sides of the coal pillars has a large development height, while the roof plastic zone has a small development range. With the increase of the advancing distance of the isolated island working face, the height of the caving zone and the fracture zone both show a slight increase trend.
- (3) The field measurement shows that the leading support pressure and top plate displacement of the noncoincident section obviously exceed that of the coincident section, and the peaks are all 10 m in front of the coal wall of the working face. Similarly, the vertical displacement of the roof in the noncoincident section is also greater than that in the coincident section

Data Availability

The data used to support the findings of this study are available from the corresponding author upon request.

Conflicts of Interest

The author declares that there are no conflicts of interest regarding the publication of this paper.

Acknowledgments

This work was supported by the National Natural Science Foundation of China (51404010 and 51374012).

References

- [1] X. F. Liu, E. Y. Wang, E. L. Zhao, and R. X. Shen, “Comprehensive prediction and effect verification of rock burst hazard in island working face,” *Journal of Mining and Safety Engineering*, vol. 27, no. 2, pp. 215–218, 2010.
- [2] X. Li, F. Pan, H. Li, M. Zhao, L. Ding, and W. Zhang, “Prediction of rock-burst-threatened areas in an island coal face and its prevention: a case study,” *International Journal of Mining Science and Technology*, vol. 26, no. 6, pp. 1125–1133, 2016.
- [3] D. Ma, H. Duan, J. Liu, X. Li, and Z. Zhou, “The role of gangue on the mitigation of mining-induced hazards and environmental pollution: an experimental investigation,” *The Science of the Total Environment*, vol. 664, pp. 436–448, 2019.
- [4] X. Liu, S. Tu, D. Hao, Y. Lu, K. Miao, and W. Li, “Deformation law and control measures of gob-side entry filled with gangue in deep gobs: a case study,” *Advances in Materials Science and Engineering*, vol. 2021, Article ID 9967870, 13 pages, 2021.
- [5] X. Liu, S. Song, Y. Tan et al., “Similar simulation study on the deformation and failure of surrounding rock of a large section chamber group under dynamic loading,” *International Journal of Mining Science and Technology*, vol. 31, no. 3, pp. 495–505, 2021.
- [6] X. S. Liu, D. Y. Fang, and Y. L. Tan, *New Detecting Method on the Connecting Fractured Zone above the Coal Face and a Case Study*, Rock Mechanics and Rock Engineering, 2021.
- [7] X. S. Liu, D. Y. Fang, and Y. L. Tan, “Failure evolution and instability mechanism of surrounding rock for close-distance parallel chambers with super-large section in deep coal mines,” *International Journal of Geomechanics*, vol. 21, no. 05, 2018.
- [8] F. Lin and H. Y. Rong, “Surrounding rock stress characteristics and support technology of isolated island working face,” *Coal Engineering*, vol. 49, no. 07, pp. 103–105, 2017.
- [9] C. Y. Liu, B. X. Huang, X. J. Meng, P. J. Yang, and L. G. Chen, “Research on the abutment pressure distribution law of super-long island fully mechanized caving face,” *Chinese Journal of Rock Mechanics and Engineering*, vol. 26, no. S1, pp. 2761–2766, 2007.
- [10] F. R. Lu and J. C. Shi, “Research on the rules and measures of rock pressure in the isolated island working face crossing the fault,” *Coal Engineering*, vol. 50, no. S1, pp. 136–138, 2018.
- [11] Z. Q. Wang, C. H. Xu, Y. J. Ren et al., “Research on roof failure mechanism under the influence of abutment pressure on isolated island working face,” *China Work Safety Science and Technology*, vol. 15, no. 6, pp. 105–112, 2019.
- [12] Y. X. Wang, J. B. Shen, and B. T. Fan, “Research on the relationship between impact hazard and micro-seismic activity of isolated island working face,” *Shandong Coal Science and Technology*, vol. 5, pp. 161–162, 2013a.
- [13] Q. Wang, S. H. Tu, Y. Yong, H. S. Tu, S. Wang, and F. Y. Feng, “Determination of reasonable coal pillar size for roadway protection in fully mechanized caving face of isolated island,” *Coal Mine Safety*, vol. 45 01, pp. 36–39, 2014.
- [14] W. J. Zhao, Y. L. Ma, Y. L. Liu, and G. W. Xu, “Research on characteristics of rock pressure in isolated island working face in shallow seam with large mining height,” *Coal Technology*, vol. 38, no. 5, pp. 21–23, 2019.
- [15] W. L. Yang, Q. D. Wei, X. C. Qu, W. X. Liu, and J. N. Zhang, “Classification and application research of isolated working face based on anti-flushing,” *China Work Safety Science and Technology*, vol. 14, no. 12, pp. 107–113, 2018.

- [16] G. A. Zhu, L. M. Dou, Z. W. Ding, and J. H. Xie, "Pre-assessment research on shock hazard of isolated island working face before mining," *Chinese Journal of Geotechnical Engineering*, vol. 40, no. 5, pp. 819–827, 2018.
- [17] L. M. Dou, Y. He, and W. D. Zhang, "Rock burst hazard and its control on isolated island working face," *Chinese Journal of Rock Mechanics and Engineering*, vol. 11, pp. 1866–1869, 2003.
- [18] Y. D. Jiang, Y. S. Pan, F. X. Jiang, and L. M. Dou, "The mechanism and prevention of rock burst in coal mining in my country," *Journal of China Coal Society*, vol. 39, no. 2, pp. 205–213, 2014.
- [19] Z. L. Li, X. Q. He, L. M. Dou, G. F. Wang, D. Z. Song, and Q. Lou, "The process of coal impact failure and the characteristics of acoustic and electrical response of the same source," *Chinese Journal of Rock Mechanics and Engineering*, vol. 38, no. 10, pp. 2057–2068, 2019.
- [20] L. M. Dou, Z. L. Li, and M. Zhang, "Research on monitoring and early warning technology for coal mine rock burst disasters," *Coal Science and Technology*, vol. 44, no. 7, pp. 41–46, 2016.
- [21] C. Wang, H. S. Tu, and Q. S. Bai, "The behavior of underground pressure in fully mechanized caving face with short-wall coal pillars in isolated island," *Coal Mine Safety*, vol. 44, no. 10, pp. 27–29, 2013b.
- [22] H. W. Zhang, Y. Cao, F. Zhu, and L. F. Shao, "Rock burst mechanism and precursor identification of hard roof island working face," *Coal Geology and Prospecting*, vol. 46, no. 2, pp. 118–123, 2018.

Research Article

Research on the Influence Mechanism of the High-Steep Slope on the Deformation Characteristics of Bridge Substructure

Yufang Zhang ¹, Hongyu Liu ², Jian Li ¹, Jiaming Li ¹, Qidi Huang ¹
and Xianjie Ma ²

¹Railway Engineering Research Institute, China Academy of Railway Sciences Group Co. Ltd., Beijing 100081, China

²School of Energy and Mining Engineering, China University of Mining and Technology (Beijing), Beijing 100083, China

Correspondence should be addressed to Jian Li; l18838978987@126.com

Received 15 June 2021; Accepted 14 August 2021; Published 1 September 2021

Academic Editor: Dawei Yin

Copyright © 2021 Yufang Zhang et al. This is an open access article distributed under the Creative Commons Attribution License, which permits unrestricted use, distribution, and reproduction in any medium, provided the original work is properly cited.

With the development of the Chinese railway, the high-steep slope is irreversible to be faced; especially under severe conditions such as heavy rainfall and earthquake, this kind of slope is prone to geological disasters, which seriously affects the safety and stability of the bridge substructure. Aiming to this, long-term monitorization and numerical analysis were carried out in this research, and the influence mechanism of the high-steep slopes on the stress and deformation characteristics of the bridge structure was studied. The research results show that under the effect of rainfall and earthquake, the original stress balance in the high-steep slope is broken, and the possibility of landslide thrust increases; under the comprehensive impact of residual landslide thrust, traction force at slope foot, vertical gravity of bridge slab and vehicle, and the bridge cap will deform. Besides, the deformation of the bridge pier exceeds the allowable lateral displacement of the top of the bridge pier, reaching 111.7%~112.4% of the limit, which seriously affects the stability of the bridge structure and the safety of the railway service. Therefore, by increasing the support strength of the slope foot and the diameter of the bridge pile foundation, the traction force of the slope foot can be reduced, and the sliding resistance of the bridge pile foundation can be improved so as the safety of the bridge structure can be promoted.

1. Introduction

Considering the railway alignment and the natural environment, many railways have to be built along high-steep slopes during the development of the Chinese railway; at this time, the horizontal force of the rock and soil will be subjected to the substructure of the bridge. Besides, because the substructure of the bridge is designed to mainly ensure vertical supportability, the horizontal bearing capacity is limited, and the deformation of the pier foundation needs to be strictly controlled. Especially under severe conditions such as the rainstorm and earthquake, the high-steep slope is prone to occur whole sliding and topsoil sliding and collapse, which seriously affects the safety and stability of the substructure of the bridge [1–5].

Compared with flat areas, the substructure of bridges on a high-steep slope is more complicated and has many differences in bearing mechanism and stress conditions. Given

its stress characteristics, the influence of the vertical load on the substructure of the bridge was studied from the aspect of the load effect of the slope soil, the bridge substructure the bearing characteristics of the slope, and the stress-strain relationship [6–12].

The loading mechanism of the bridge substructure is studied mainly by using the methods of theoretical analysis, numerical simulation, and model experiment. After being subjected to the horizontal loading, the deformation characteristics and the relationship between internal stress and deformation of the bridge substructure were studied [13–19].

Although there has been much relevant research, they just carry out the qualitative investigation from the aspects of deformation characteristics and influence mechanism, and the quantitative research is still limited.

In this paper, based on a railway, the influence mechanism of the high-steep slopes on the stress and deformation characteristics of the bridge substructure was studied.

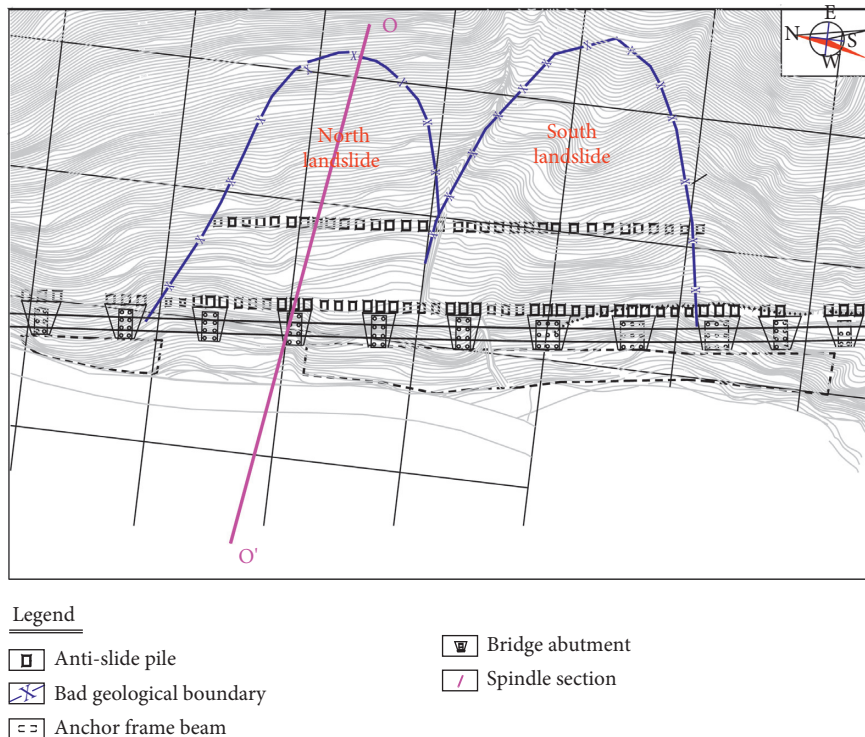


FIGURE 1: The engineering geological plan of landslide.

2. Overview of Long-Term Monitorization

2.1. The Introduction of the Project Site. The bridge structure is located at the foot of the steep slope, which is in the range of the alluvial fan accumulation area and the river terrace area, and the terrain in this area is relatively flat and is high in the east (on the side of the mountain) and low in the west (on the side of the river), forming deep gullies. In order to reduce the threat of high-steep slopes to the bridge substructure, the antislides piles are mainly adopted as protective measures as shown in Figures 1 and 2.

2.2. Stability Evaluation of High-Steep Slope. As shown in Figure 3, the landslide scale is relatively large and composed of two landslides in the north and south directions. For the north landslide, the direction of the main axis is $NW81^\circ$, the longitudinal slope is about 42° , the length of the main axis is about 130 m, and the width of the landslide bottom is about 202 m. From the aspect of geomorphology, the landslide has the potential of collapse, and the sliding surface is steeper than the accumulation layer; besides, the rock and soil are unevenly distributed, and the weak rock and soil are easy to be weathered and softened by water.

Under the intense effect of the geological structure, the rock mass is broken, and the joint fissures are more developed in the shape of "X," and the joint surface is mostly orthogonal to the layer. The joint surface is relatively straight, the joints of the earth surface slightly open ($1 \sim 5$ mm) with the space of $0.3 \sim 1$ m, the sandstone spacing is large, the slate spacing is small, and the rocks mostly

disintegrate along the joint surface, forming dangerous rocks on the cliff.

According to the on-site survey, it is analyzed that the high-steep slope has a significant impact on the bridge substructure, and its instability may endanger the bridge substructure under the condition of rainfall or earthquake.

3. Long-Term Monitorization and Analysis of the Influence of High-Steep Slope on Bridge Substructure

3.1. The Design of the Long-Term Monitorization

3.1.1. Monitorization Scheme. In the field, the deep displacement of the slope, the deformation and stress of the antislides pile, and the stress of the bridge pile foundation are all monitored.

3.1.2. Rainfall Condition. The landslide is located in the alpine climate zone in northwestern Sichuan, where the annual precipitation is 500–900 mm, and the 30-year average annual precipitation is 731.226 mm. The rainy season is from early June to mid-September, accounting for about 50% to 60% of the annual rainfall.

3.1.3. Earthquake Condition. On May 12, 2008, an M8.8 earthquake occurred in Wenchuan County, Aba Prefecture, Sichuan Province, and an M7.0 earthquake occurred in Jiuzhaigou County, Aba Prefecture, Sichuan Province, on

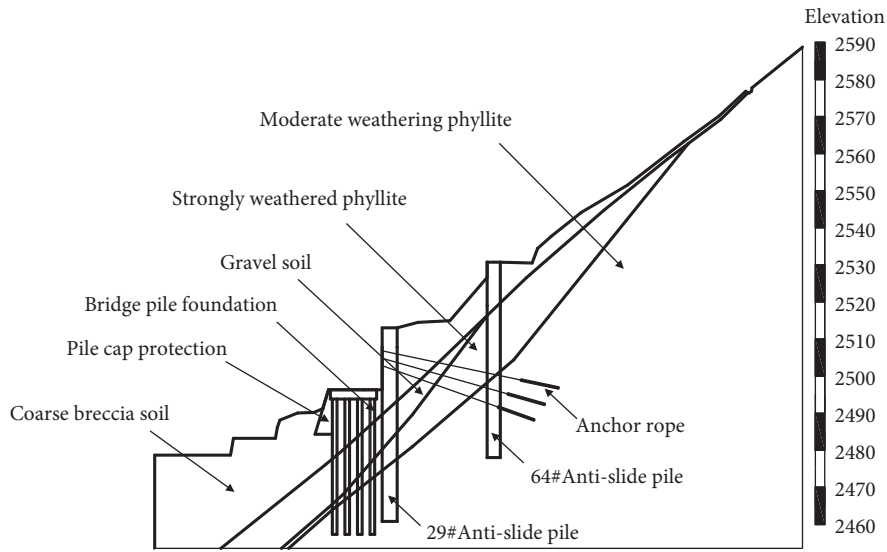


FIGURE 2: Engineering geological section of landslide.

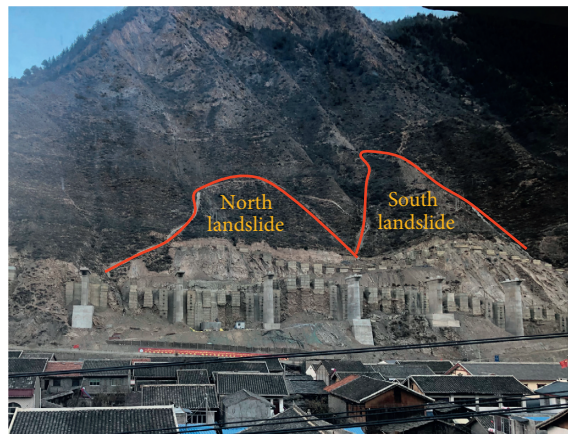


FIGURE 3: The illustration of the landslide body.

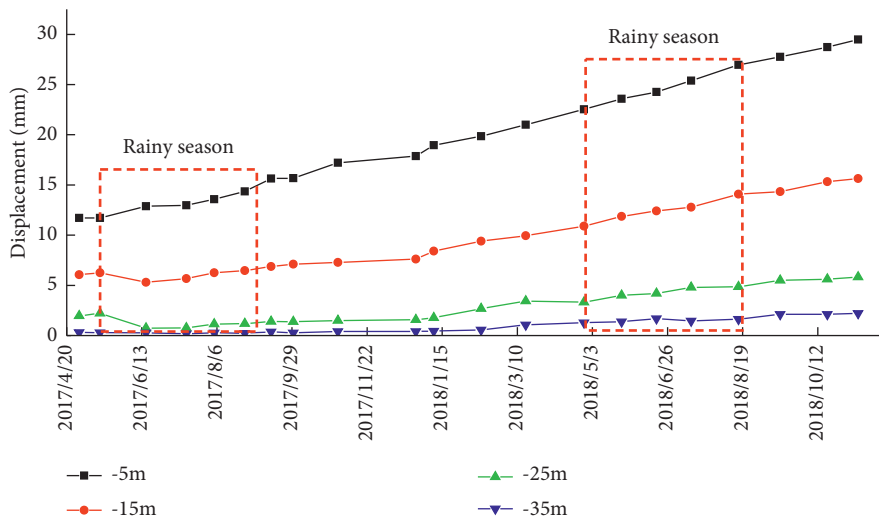


FIGURE 4: Displacement curve of 29# antislid pile at same depths during the rainy season.

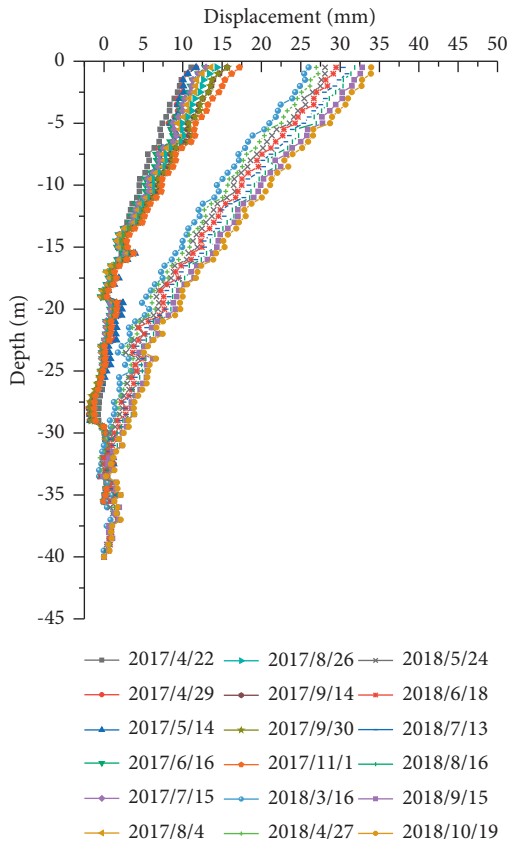


FIGURE 5: Displacement curve of 29# antislid pile at different depths during the rainy season.

August 8, 2017. The intensity of the area where the landslide is located is 6.0.

3.2. Long-Term Monitorization and Analysis of the Impact of High-Steep Slopes on Bridge Engineering under Rainfall Conditions. As shown in Figure 4, in the rainy season, the 29# antislid pile exhibited the same deformation characteristics at different depths; the displacement of the antislid pile continuously increases, and the maximum deformation reached 5 mm at the depth of 5 m.

As shown in Figure 5, it can also be found that the 29# antislid pile exhibited the trend of the relative displacement decreasing with the depth, and the maximum deformation of the surface was 6 mm, indicating that the adoption of the antislid pile is effective, and the high-steep slope is in a stable state under normal rainfall condition.

As shown in Figure 6, in the rainy season, the body stress on the side of the pile showed the shape of “ε” in overall and an increasing trend. The stress reached the maximum at 19 m, with an average daily increase of 0.12 MPa; this low growth rate indicates that the antislid pile has a good supporting effect when the pile stress is increased by the increased slope thrust under the effect of rainfall.

As shown in Figure 7, in the rainy season, the stress on the pile foundation of the 4# bridge pier generally showed a gentle increasing trend with an average daily increase of 0.012 MPa and reached the maximum at 10m; besides,

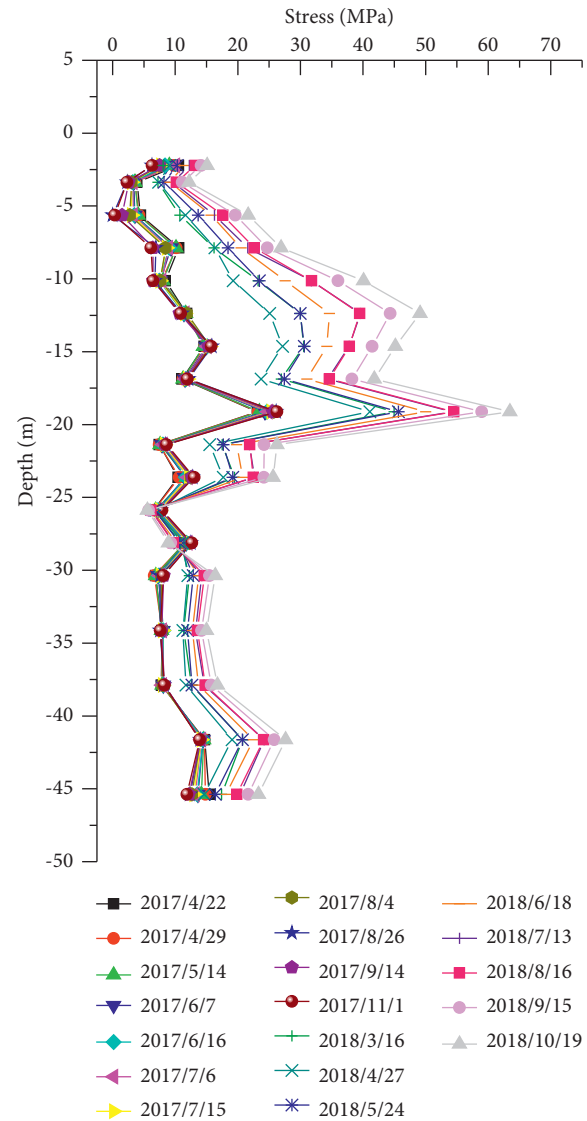


FIGURE 6: Body stress of 29# antislid pile during the rainy season.

compared with the 29# antislid pile, its growth rate was reduced by 90%. At the same time, the pile foundation showed a stress reversal point near the soil-rock interface, where the stress is -4.37MPa , and its value increased with the rainfall; this indicates that due to the existence of the antislid pile, the remaining landslide thrust subjected to the bridge pile foundation is significantly reduced, and the bridge pile foundation is nearly not affected.

In a regular rainfall year, the support structure of the bridge can guarantee that the increased landslide thrust has no significant impact on the stress of the bridge structure. However, it cannot be assured under the condition of extreme rainfall or continuous heavy rainfall.

3.3. Long-Term Monitorization and Analysis of the Influence of High-Steep Slopes on Bridge Engineering under Earthquake Condition. As shown in Figure 8, during the earthquake, the 29# antislid pile generally showed the characteristics of

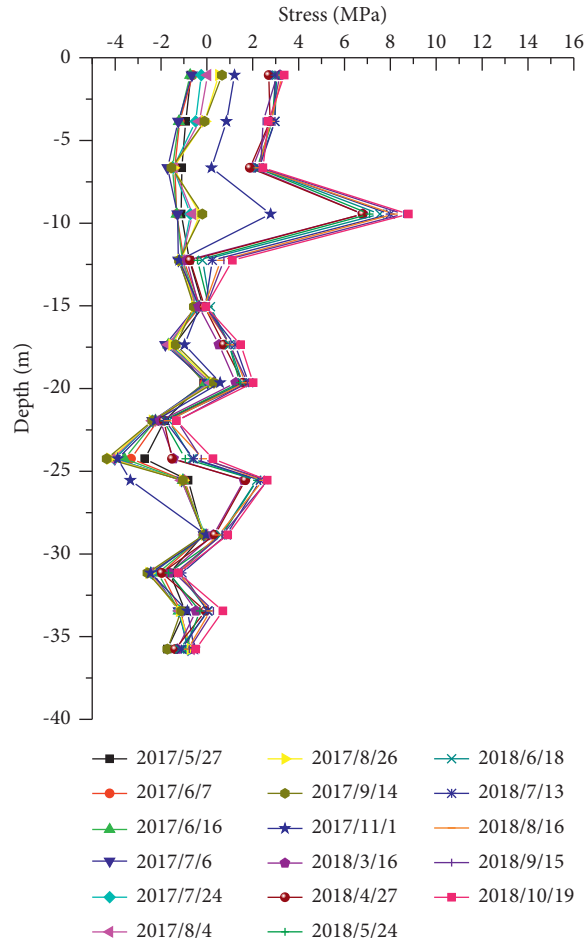


FIGURE 7: 4# stress curve of bridge pier pile foundation at different depths.

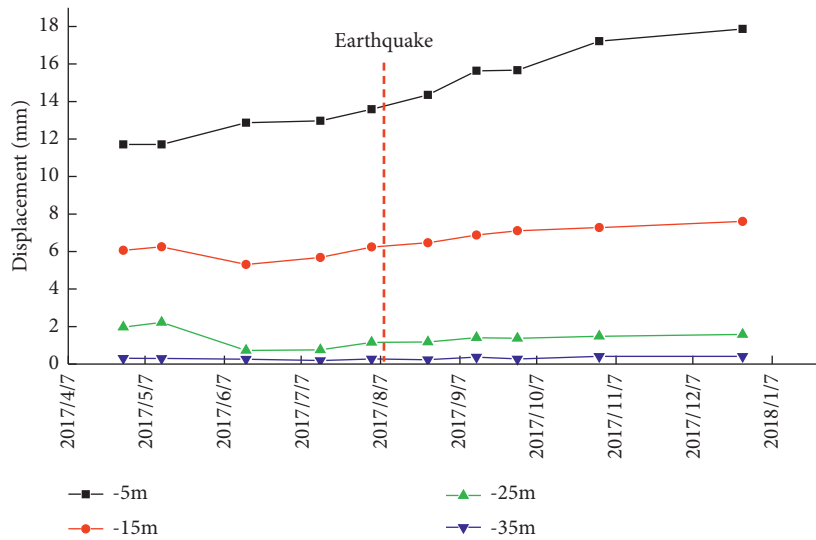


FIGURE 8: Displacement curve of 29# antislid pile at same depths during the earthquake.

relative displacement decreasing with the depth, but its variation became gentle from the depth of 25 m to the depth of 35 m. After the earthquake, the displacement did not change, indicating that the earthquake with a magnitude of

6.0 does not cause a significant impact on the high-steep slope, and the slope can keep stable.

As shown in Figure 9, the slope was disturbed by the earthquake, and the 29# side inclined hole produced a

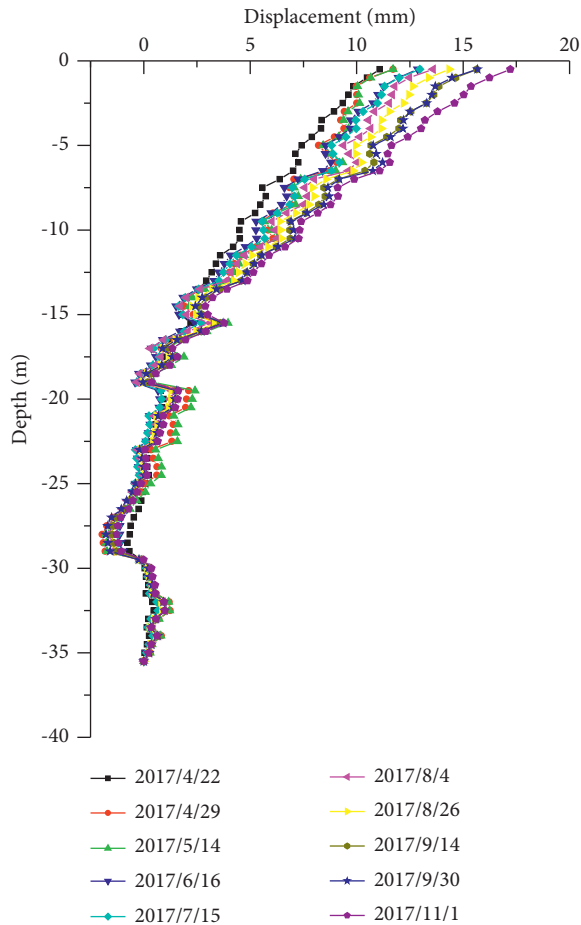


FIGURE 9: Displacement curve of 29# antislide pile at different depths during the earthquake.

maximum displacement of 0.8 mm; this small displacement suggests that the slope body is in a stable state as a whole.

As shown in Figure 10, under the effect of the earthquake, the body stress of the antislide piles generally showed a gradually increasing trend. After the earthquake, the daily stress increment was 37 kPa, and the pile did not change significantly, indicating that the stress of the antislide piles plays a good supporting role and is in a stable state.

As shown in Figure 11, during the earthquake, the stress characteristics of the 4# bridge pier pile foundation were similar to those in the rainy season, except that the stress was relatively small; this indicates that due to the antislide pile, the remaining landslide thrust caused by the loosening of the rock and soil caused has been significantly reduced and has no obvious impact on the bridge pile foundation.

Under the influence of an earthquake with a magnitude of 6, the increased landslide thrust of the high-steep slope does not have a significant impact on the stress of the bridge structure because of the support of the bridge structure.

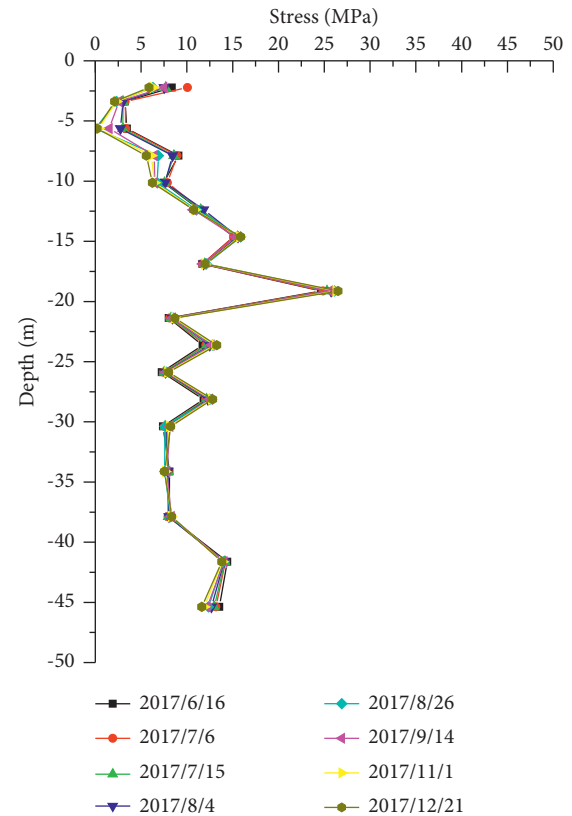


FIGURE 10: The body stress of 29# antislide pile during the earthquake.

However, the situation may be different under extreme earthquake conditions.

4. Numerical Analysis of the Influence of High-Steep Slope on Bridge Substructure

4.1. The Numerical Simulation

4.1.1. The Establishment of the Model. In this research, FLAC3D software was adopted for numerical calculation and analysis. During modelling, the soil adopts the Mohr-Coulomb constitutive; the pile cap and the antislide pile are simulated by solid elements; the pile foundation is simulated by the pile element; and the anchor cable is simulated by the cable element; besides, the normal displacement is restricted, the bottom is fixed, but the slope surface is free, as shown in Figure 12.

According to the in-site geology survey of landslides, the stratigraphic parameters can be determined and shown in Table 1.

4.1.2. Rainfall Condition. Rainfall will increase the water content of the slope soil, leading to the reduction of the cohesive force and internal friction angle, furtherly causing slope instability. In order to model the most unfavourable

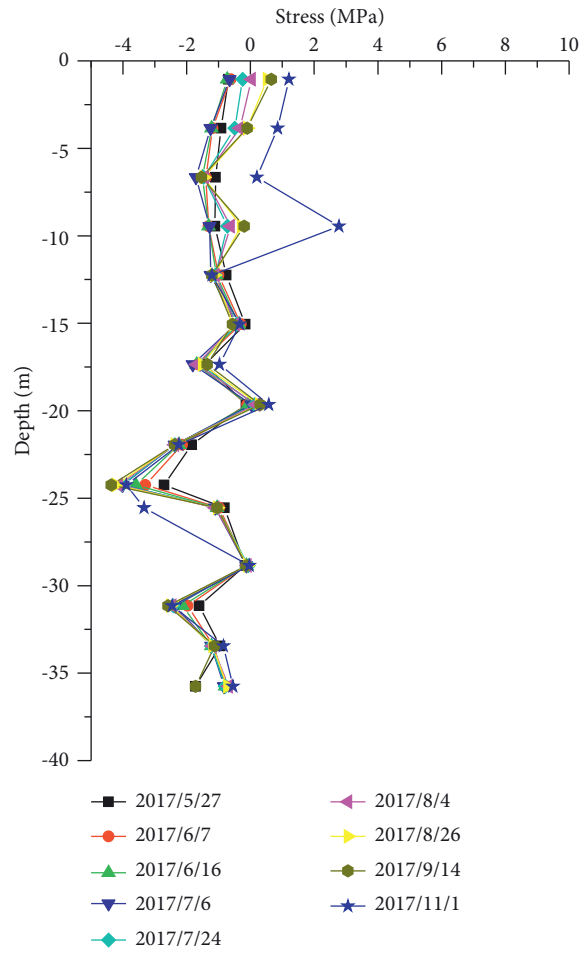


FIGURE 11: The body stress of 29# antislide pile during the earthquake.

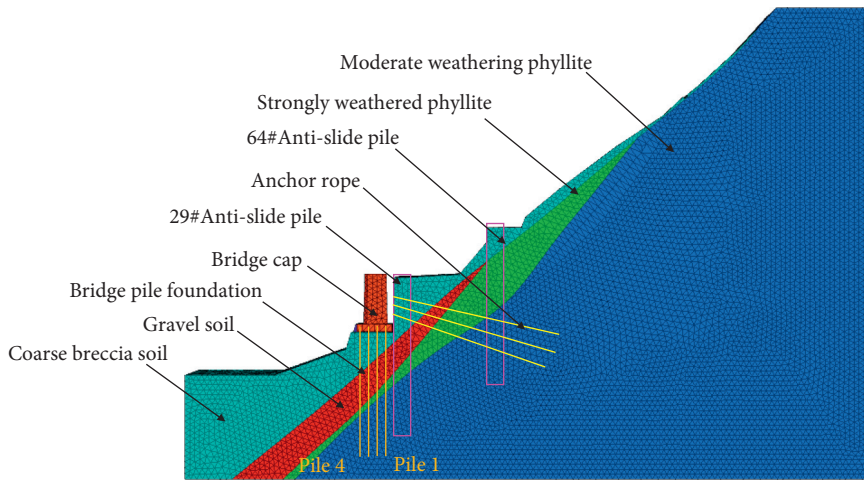


FIGURE 12: Numerical calculation model.

TABLE 1: Physical and mechanical parameters of landslide.

Material	Gravity (kN/m ³)	Elastic modulus (MPa)	Poisson's ratio	Cohesive force (kPa)	Friction angle (°)
Coarse breccia soil	20	20	0.2	10	21
Gravel soil	21	40	0.2	17	24
Strongly weathered phyllite	24	500	0.18	45	30
Moderate weathered phyllite	25	1800	0.17	200	55

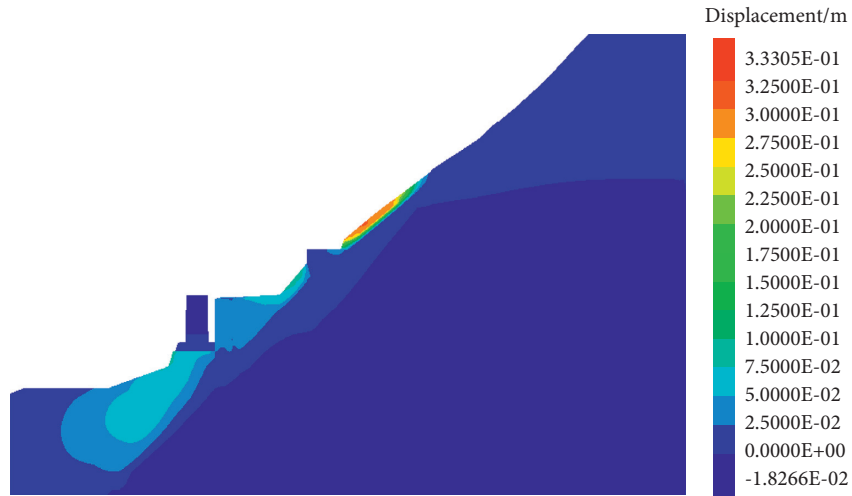


FIGURE 13: Cloud diagram of horizontal displacement of the slope.

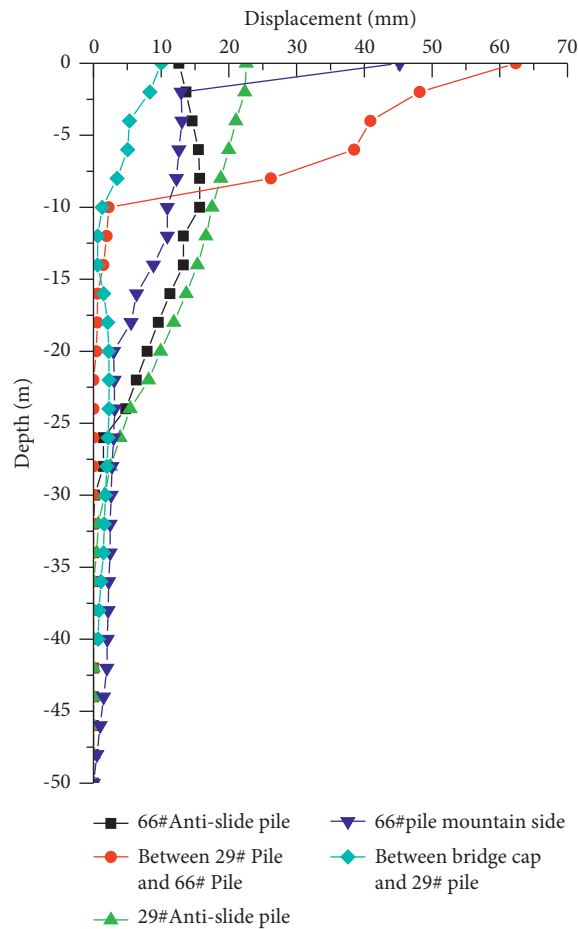


FIGURE 14: The deep displacement curve of the slope.

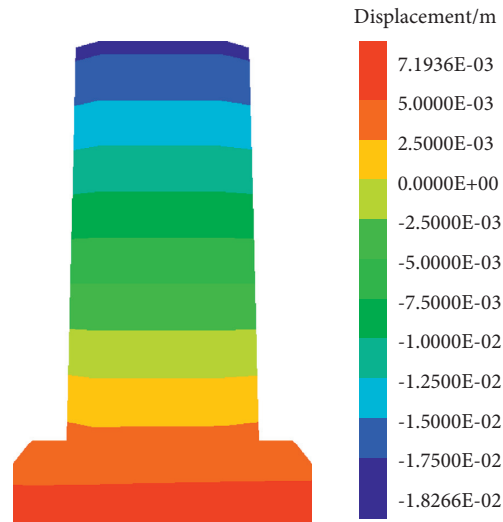


FIGURE 15: Cloud diagram of horizontal displacement of bridge cap.

conditions of extreme rainfall, the soil parameters when the soil is close to the saturated state were chosen.

4.1.3. Earthquake Condition. The quasistatic method was used to conduct seismic analysis of the slope, and the peak acceleration of the site vibration was 0.2 g. A rare earthquake with a fortification intensity of 8 as the basic acceleration α of the horizontal earthquake, and the comprehensive horizontal earthquake coefficient α_w was taken as 0.05.

4.2. Numerical Calculation of Extreme Rainfall Condition

4.2.1. The Analysis for the Simulate Displacement. As shown in Figures 13–15, under the same rainfall condition, there were three distinct areas showing deformation; among them, the deformation of the upper side area of 66# antislid piles was the most obvious, and the maximum displacement of soil was 330 mm; between 29# antislid piles, the maximum deformation was 27.2 mm, and the soil between the 29# antislid pile and the cap deformed 10.68 mm, suggesting that under the action of rainfall, the slope produced landslide thrust, but the displacement gradually decreased because of the two rows of antislid piles. Simultaneously, the 29# antislid pile produced a squeezing effect on the soil on the riverside; thus, the remaining landslide thrust on the bridge cap caused the deformation of the bridge cap, and a 100 mm deformation occurred at the toe of the slope, indicating that the controlling deformation at the toe of the slope should be considered during the design of the support.

Under the comprehensive effects of the landslide thrust, the traction force from the riverside, the vertical bridge slab, and the vehicle gravity, the bridge cap occurred an overall inclined deformation, in which the top part moved 18.26 mm to the mountainside relative to the bottom part, and the bottom part moved 7.19 mm to the riverside,

reaching 111.7% of the allowable lateral displacement limit of 16.35 mm in the “Code for Design of Railway Bridges and Culverts” [20], and seriously affects the safety of railway operations.

4.2.2. Stress Analysis of Bridge Pile Foundation. Under the condition of extreme rainfall, due to the decrease in the strength of the soil layer, the stress of the bridge pile foundation mainly showed the following characteristics in Figure 16.

The distribution of the bending moment of the bridge pile was closely related to the stratum. Under the combined effect of the remaining landslide thrust and the traction force of the slope toe, the distribution of the bending moment of each pile varied; among them, pile 2 and pile 3 showed the largest negative bending moment, and the maximum negative bending moment of pile 2 appeared at 14 m below the top of the pile, and the maximum negative bending moment of pile 3 appeared at 23 m below the top of the pile. From pile 1 to pile 4, the position of the maximum negative bending moment continuously decreased with the bedrock of the slope.

Compared with ordinary bridge pile foundations, the bridge pile foundation on the high-steep slope has dual functions of load-bearing and sliding resistance. In the bridge design, the reinforcement of the side piles and the caps should be paid special attention. At the same time, the corresponding reinforcement design should be chosen according to the distribution characteristics of the bending moment of each pile.

4.3. Numerical Calculation and Analysis of the Extreme Seismic Condition

4.3.1. Analysis of Displacement Calculation Results. As shown in Figures 17–19, under the impact of seismic with the intensity of 8°, the slope deformation characteristics were

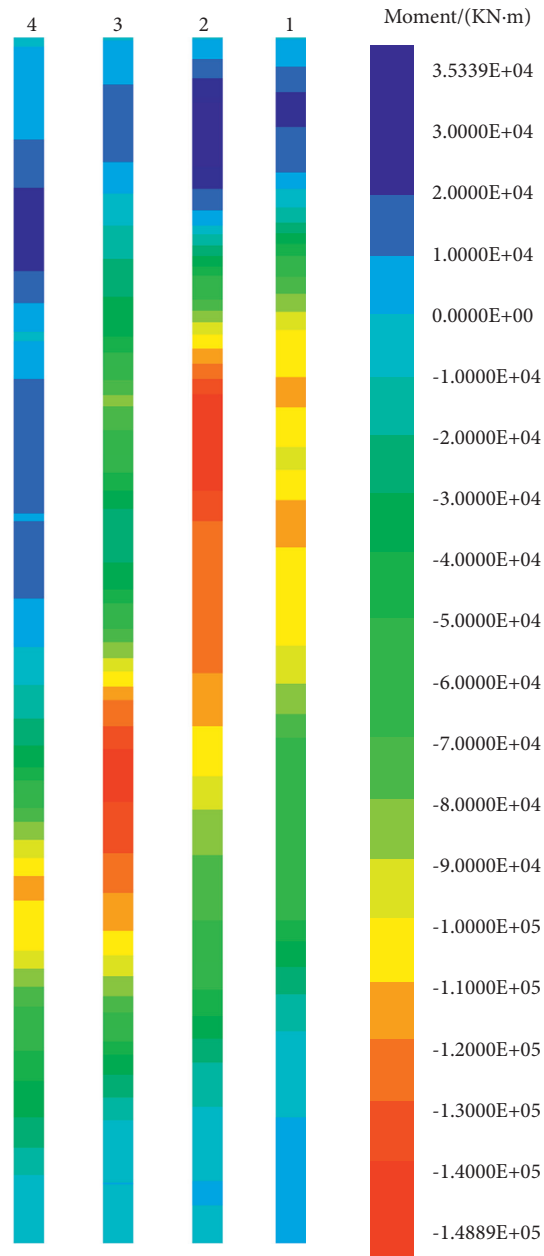


FIGURE 16: Cloud diagram of bending moment of bridge pile foundation.

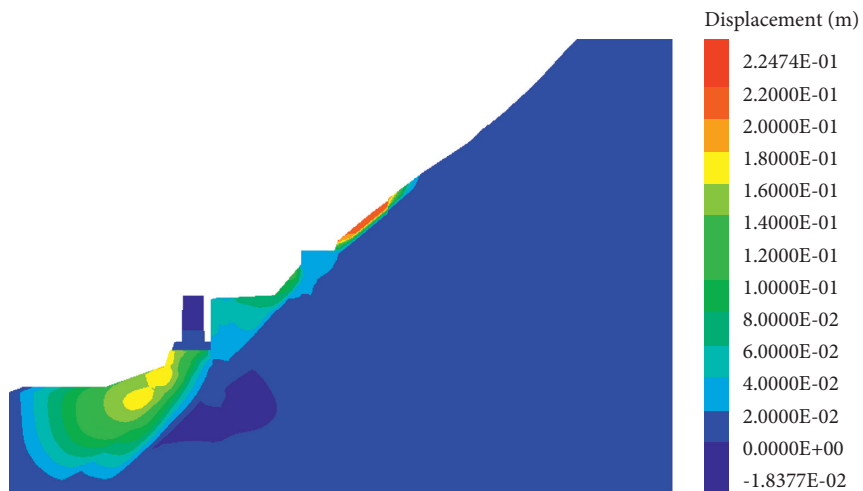


FIGURE 17: Cloud diagram of bending moment of bridge pile foundation.

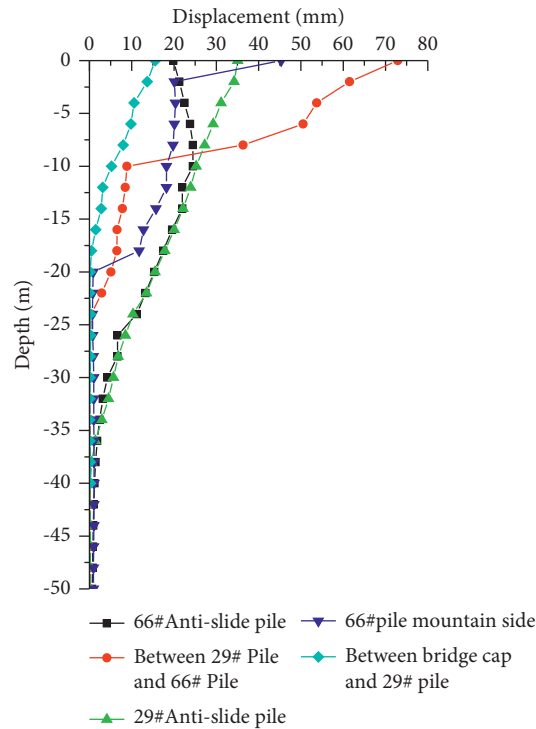


FIGURE 18: The displacement curve of the deep part of the slope.

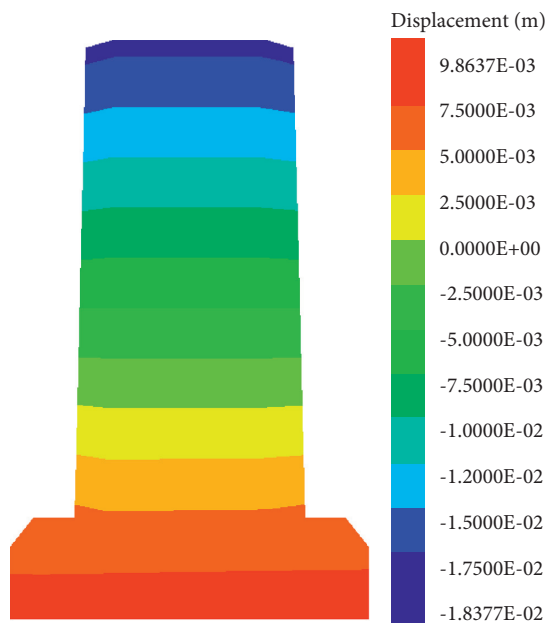


FIGURE 19: Cloud diagram of horizontal displacement of bridge cap.

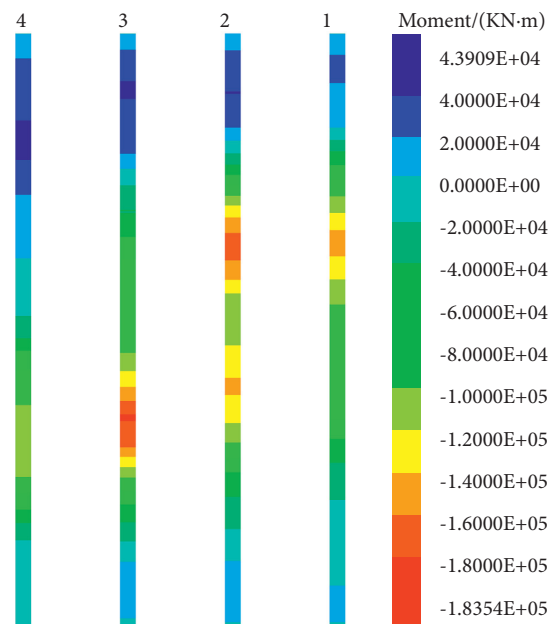


FIGURE 20: Cloud diagram of bending moment of bridge pile foundation.

similar to those under the extreme rainfall condition. The deformation of the upper side of the 66# antislid pile was the most obvious with the maximum soil displacement of 224.7 mm; the maximum deformation between the 29# antislid piles was 40 mm, and the soil between the 29# antislid pile and the cap deformed 17 mm; this indicates that under the function of two rows of antislid piles, the

remaining landslide thrust acting on the bridge cap caused the deformation of the bridge platform, as well as the 184 mm deformation at the slope toe.

Under the action of the earthquake, the bridge caps also showed an overall inclined deformation, in which the bottom part moved 9.86 mm to the riverside and the top part moved 18.37 mm to the mountainside, reaching 112.4% of

the 16.35 mm lateral allowable displacement limit of the top of the bridge pier in the “Code for Design of Railway Bridges and Culverts” [20], which seriously affects the safety of railway operation.

4.3.2. Stress Analysis of Bridge Pile Foundation. Under the seismic intensity of 8 degrees, due to changes in the internal bridge structure of the rock mass, the stress of the bridge pile foundation mainly shows the following characteristics.

As shown in Figure 20, under the impact of the earthquake, the stress characteristics of the bridge pile foundation were more consistent with those under rainfall; the negative bending moment of pile 2 and pile 3 was the largest, the maximum negative bending moment of pile 2 appeared at 14 m below the top of the pile, and the maximum negative bending moment of pile 3 appeared at 24.5 m below the top of the pile. From pile 1 to pile 4, the position of the maximum negative bending moment continuously decreased.

5. Conclusion and Discussion

With a railway landslide body as the background, field monitoring tests and numerical analysis were carried out on high-steep slopes. The mechanism of the influence of the high-steep slope on the bridge structure was analyzed.

- (1) Under the conditions of rainfall and earthquake, the original stress balance in the slope is broken, resulting in the continuous increase in the landslide thrust. Because of the existence of the supporting structure, the remaining landslide thrust causes the lower slope to produce compression and transmits squeeze force to the bridge structure. Under the effect of the remaining landslide thrust, the traction force of the slope toe and the vertical bridge slab and the gravity of the vehicle, the bridge cap declines and deforms.
- (2) During the in-site monitorization, under the influence of rainfall and earthquake, the antislide pile and bridge structure deforms, but the force and deformation characteristics are not obvious, and the slope and bridge structure remains stable as a whole.
- (3) Under extreme conditions such as rainfall and earthquakes, the deformation of the bridge pier and abutment exceeds the allowable limit of the lateral displacement of the pier top, reaching 111.7%~112.4% of the limit, which seriously affects the stability of the bridge structure and the safety of railway operations. The horizontal bearing capacity of the bridge structure is limited, and the deformation of the pier foundation is strictly required. In the design of the bridge pile foundation, the slip resistance of the bridge pile foundation can be increased by increasing the pile diameter, and the deformation of the bridge cap can be reduced.
- (4) The bridge structure at the foot of the high-steep slope is affected by the combined effect of the landslide thrust and the traction force of the slope

toe. While designing the support structure, not only the landslide thrust of the slope should be considered but also the traction force from the slope toe.

Data Availability

The data used to support the findings of this study are available from the corresponding author upon request.

Conflicts of Interest

The authors declare that they have no conflicts of interest.

Acknowledgments

This research was funded by National Key R&D Program of China (No. 2018YFC1504902), China Railway Corporation Research and Development of Science and Technology Plan Project (No. P2018G001), and National Railway Group Science and Technology Research and Development Program (No. N2020G052).

References

- [1] H. Luo, “Research on effect of heap loading on deformation and mechanical properties of bridge double pile foundation on steep slope,” *Open Journal of Civil Engineering*, vol. 10, no. 2, pp. 117–130, 2020.
- [2] L. Sun, *Research on Calculation and Analysis Method of Bridge Group Pile Foundation in Slope Section with Poor Stability*, Southwest Jiaotong University, Chengdu, China, 2019.
- [3] Q. Chang, *Research on the Interaction between Steep Slope and Bridge Pile Foundation under Earthquake*, Jiangxi University of Science and Technology, Ganzhou, China, 2019.
- [4] Y. Zhang, J. Tang, Z. He, and J. Tan, “A novel displacement prediction method using gated recurrent unit model with time series analysis in the Erdaohe landslide,” *Natural Hazards*, vol. 105, 2020.
- [5] Y. Zhang, Z. Zhang, and S. Xue, “Stability analysis of a typical landslide mass in the Three Gorges Reservoir under varying reservoir water levels,” *Environmental Earth Sciences*, vol. 79, no. 1, 2020.
- [6] D. Qing, “Three-dimensional finite element method for slope stability evaluation under bridge foundation load,” *Highway Engineer*, vol. 34, no. 3, pp. 38–42, 2008.
- [7] M. Zhao, P. Yin, M. Yang, and Y. Li, “Analysis of mechanical characteristics and influencing factors of bridge pile foundations on high and steep slopes,” *Journal of Central South University*, vol. 43, no. 7, pp. 2733–2739, 2012.
- [8] W. Zhao, Q. Xie, and Y. Li, “Study on the safety distance of bridge foundation on high and steep slope,” *Journal of Railway Engineering Society*, vol. 23, no. 6, pp. 47–50, 2006.
- [9] H. Lassaad, N. Hussien Mahmoud, and K. Mourad, “On the behaviour of pile groups under combined lateral and vertical loading,” *Ocean Engineering*, vol. 131, pp. 174–185, 2017.
- [10] M. N. Hussien, T. Tobita, S. Iai, and M. Karray, “On the influence of vertical loads on the lateral response of pile foundation,” *Computers and Geotechnics*, vol. 55, pp. 392–403, 2014.
- [11] Y. El-Mossallamy, “Pile group action under vertical compression loads,” *Advances in Soil Mechanics and Geotechnical Engineering*, IOS Press, Amsterdam, Netherlands, 2014.

- [12] C. Wang, *Research on the Mechanical Behavior of Three-Dimensional High Slope Rock Mass and the Determination of the Location of the Bridge Foundation under the Load of the Bridge Foundation*, Southwest Jiaotong University, Chengdu, China, 2008.
- [13] Z. Li, G. Quan, D. Liu et al., "Experimental study on horizontal load of soil slope building pile foundation," *Chinese Journal of Rock Mechanics and Engineering*, vol. 23, no. 6, pp. 930–935, 2004.
- [14] O. Reul and M. F. Randolph, "Design strategies for piled rafts subjected to nonuniform vertical loading," *Journal of Geotechnical and Geoenvironmental Engineering*, vol. 130, no. 1, pp. 1–10, 2004.
- [15] M. Gennaro, A. Osouli, Z. Siavash, and I. Shafii, "Performance of a pier group foundation in swelling rock," *Geotechnical & Geological Engineering*, vol. 32, no. 1, pp. 197–204, 2014.
- [16] G. Konstantinos, M. Georgiadis, and C. Anagnostopoulos, "Lateral bearing capacity of rigid piles near clay slopes," *Soils and Foundations*, vol. 53, no. 1, pp. 144–154, 2013.
- [17] M. Zhao, C. Yang, M. Yang et al., "Force analysis of bridge foundation piles in steep slope section based on finite pole element method," *China Journal of Highway and Transport*, vol. 27, no. 6, pp. 51–58, 2014.
- [18] X. Gong, M. Yang, M. Zhao et al., "Model test of bearing mechanism of bridge pile foundation in high and steep transverse slope section in mountainous area," *China Journal of Highway and Transport*, vol. 26, no. 2, pp. 56–62, 2013.
- [19] B. Yuan, K. Xu, Y. Wang, and R. Chen, "Investigation of deflection of a laterally loaded pile and soil deformation using the PIV technique," *International Journal of Geomechanics*, vol. 14, no. 1, pp. 1–7, 2014.
- [20] The Third Railway Survey and Design Institute Group Co. Ltd, *TB 10002-2017, Code for Design of Railway Bridges and Culverts*, Railway Publishing House, Beijing China, 2017.

Research Article

Study on the Stability of Slopes Reinforced by Composite Vegetation Combined with a Geogrid under Rainfall Conditions

Qizhi Hu , **Yong Zhou**, and **Gaoliang Tao**

College of Civil Construction and Environment, Hubei University of Technology, Wuhan 430068, China

Correspondence should be addressed to Qizhi Hu; 709317769@qq.com

Received 22 April 2021; Revised 26 June 2021; Accepted 7 August 2021; Published 19 August 2021

Academic Editor: Dezhong Kong

Copyright © 2021 Qizhi Hu et al. This is an open access article distributed under the Creative Commons Attribution License, which permits unrestricted use, distribution, and reproduction in any medium, provided the original work is properly cited.

The planting of shrubs and trees on geogrid-reinforced slopes is an important ecological slope protection method that is frequently implemented in the rainy areas of southern China. First, this paper analyzes the soil-fixing principle of the geogrid and root system and demonstrates the feasibility of using composite vegetation of shrubs and trees to reinforce the slope with a geogrid. Using the Yushi Expressway project in Guizhou, we conducted a stability analysis of slopes under different working conditions and different reinforcement modes. We determined that the ecological protection method of combining composite vegetation with a geogrid can effectively increase the stability of slopes. The maximum displacement of the ecological slope under rainfall conditions was reduced by 82% compared with the original slope, and the overall stability was improved by 35%. Four factors affect the slope stability: the depth of shrub reinforcement, depth of anchorage of trees, distribution of trees, and spacing of the geogrids. An orthogonal analysis considering these 4 factors with 3 levels was implemented. The following optimal combination was obtained to ensure ecological protection under rainfall conditions: a shrub reinforcement depth of 0.6 m, a tree anchorage depth of 3 m, a grid spacing of 0.4 m, and a top-sparse and bottom-dense tree distribution. The combined slope protection schematic was applied to the Yushi Expressway project in Guizhou, and a strong reinforced slope protection effect was observed.

1. Introduction

Under rainfall conditions, the erosion resistance of exposed slopes decreases, and soil erosion increases, which can easily induce major natural disasters such as landslides [1, 2]. Ecological slope protection efforts consider both engineering protection and environmental beautification and are widely used in China. Under the action of plant roots, the surface soil of an exposed slope is consolidated, and the shear strength is increased. The transpiration of plant leaves and suction of roots also improve the suction of the surface soil, stop ground runoff, and prevent scouring, which helps soil and water conservation. However, the contribution of root consolidation to slope stability is limited and not applicable to unstable or understable slopes. With the development of geosynthetics, geogrids have been widely used in slope engineering due to their obvious reinforcement effect and relatively economical nature [3]. Therefore, the planting of shrubs and trees on geogrid-reinforced slopes can improve

the stability of slopes and highlight the ecological benefits of such conservation efforts since it is an important method for slope management in rainy areas.

At present, many scholars have conducted various studies on geogrids and root reinforced slopes. Among them, numerical simulation technology can intuitively analyze the failure mechanism inside the rock and soil and is widely used in slope stability analysis. For example, Sun et al. used the finite element software Midas-GTS to simulate the performance of reinforced soil slopes, and they compared the numerical simulation results with monitoring data to verify that numerical simulation techniques can reliably analyze geogrid-reinforced slopes [4, 5]. Zhang et al. took the actual engineering of geogrid reinforcement of the slope as an example, analyzed the stability of the slope, and optimized the geogrid reinforcement scheme [6, 7]. Yang et al. discussed the mechanical mechanism of plant roots for soil consolidation and compared the stability of grass, shrub, arbor, and composite vegetation reinforcement under the slope. They noted that composite

vegetation had significantly higher reinforcement effect than single vegetation [8]. Waldron et al. conducted a shear test on reinforced soil and noted that reinforced soil mainly exerted the reinforcement effect by improving the original cohesion of the soil [9–11]. Su et al. conducted a pull test of the root system of the arbor. The influence of the root diameter on the anchorage of arbor roots was quantitatively analyzed [12]. Abdi et al. calculated the spatial distribution of plant roots in the soil; they found that the roots of shrubs were mainly distributed 0.6 m below the slope, and the roots of trees could reach 3 m in length [13, 14]. However, these studies did not consider the influence of geogrids and root systems on the hydraulic characteristics of slopes.

Rainfall infiltration is an important factor that induces slope instability [15, 16]. Based on the theory of unsaturated seepage, Zhang et al. established a hydraulic-mechanical coupling numerical calculation model for reinforced soil slopes and studied the effects of rainfall infiltration on the stress, displacement, and pore pressure of geogrid-reinforced soil slopes [17, 18]. Zhang et al. analyzed the seepage field distribution of root-fixed soil under rainfall conditions and found that when the root system continued to absorb water, the shear strength of unsaturated soil also increased [19, 20]. Ng et al. studied the size and distribution of suction generated by plant roots in soil and noted that plants could significantly increase soil suction under both dry and rainy conditions [21]. Wang et al. conducted a slope model test under rainfall conditions and believed that plant roots could improve the hydraulic properties of the soil and reduce the impact of rainfall on the slope runoff [22–24]. Song et al. proposed a composite soil treatment and slope protection method using the geocell structures and the wheat straw reinforcement, which can effectively reduce soil erosion on the slope [25].

These studies mainly focused on the influence of a single reinforcement mode and a single factor on the slope deformation and stability. There are few studies on slope reinforcement by composite vegetation with geogrids. With the improvement of the dual requirements of economic and ecological benefits, joint ecological slope protection technology has widely become the optimal choice for slope treatment. However, its work performance is more complicated, and there are many influencing factors. There is no clear understanding of the design plan for planting shrubs and trees on slopes reinforced by geogrids. Especially under rainfall conditions, it is of great significance to quantify the influence of various factors on the mechanical and hydraulic characteristics of ecological slopes. Therefore, to popularize this technology in engineering, it is necessary to study the stability of composite vegetation with geogrid reinforcement under rainfall conditions.

2. Soil Fixation Mechanism of Geogrid and Root Systems

As common reinforcement materials, geogrid and root systems can affect the mechanical properties of the soil and root system as an active medium. They can absorb water from different soil depths through the transpiration of plant leaves, increase the soil suction, and change the hydraulic

characteristics of unsaturated soil. We analyzed the soil fixation mechanism of a geogrid and a root system based on mechanical and hydraulic soil properties as follows.

2.1. Mechanical Activation Behavior. Geogrids and root systems have high tensile strengths. After being implanted in the soil, roots can interact with the soil to improve its tensile and shear strength and form a reinforced soil. Therefore, its mechanical properties can be quantitatively analyzed by reinforced soil theory, which mainly includes two types: the friction reinforcement principle and quasi-cohesive force mechanism.

The principle of friction reinforcement is that the reinforcing material is firmly fixed inside the soil body under the action of soil pressure; when the relative displacement of the soil body and reinforcing material occurs, the slip force will be transferred to the reinforcing material. Due to the friction between soil and tendons and the high tensile strength of the tendons, the soil deformation can be limited, which improves the soil stability. Section d_i of the reinforced soil is selected for analysis, as shown in Figure 1:

$$\begin{aligned} F &= 2\sigma_n f b d_i, \\ d_T &= T_1 - T_2, \end{aligned} \quad (1)$$

where F is the frictional resistance, σ_n is the effective stress that acts on the reinforced material, f is the friction coefficient, b and d_i are the width and length of the reinforced material, and d_T is the tensile force on the reinforced material. When $F > d_T$, the reinforced soil is in a stable state, and vice versa for destabilization.

The mechanism behind quasi-cohesion is to regard the reinforced soil as a composite material. Reinforcements play a similar role in the confining pressure, which limits the soil deformation. Reinforced soil mainly exerts the reinforcement effect by improving the original cohesion of the soil. As shown in Figure 2, the strength envelope of reinforced soil is parallel to that of unreinforced soil, and only the point of intersection with the vertical axis is significantly different. When the confining pressure σ_3 is constant and the soil reaches the ultimate equilibrium state, the maximum principal stress σ'_1 of the reinforced soil is obviously greater than the maximum principal stress σ_1 of unreinforced soil, and the strength of the reinforced soil is substantially improved. When the maximum principal force σ'_1 is constant, the minimum principal stress σ'_3 of unreinforced soil can be calculated using its strength envelope. Figure 2 shows that σ'_3 is significantly larger than σ_3 , which indicates that the tendons can limit the soil deformation and increase the enclosing pressure. The increase in confining pressure is defined as follows:

$$\Delta\sigma_3 = \sigma'_3 - \sigma_3 = 2\Delta c \cdot \tan\left(45^\circ - \frac{\varphi}{2}\right), \quad (2)$$

$$\begin{aligned} \Delta\sigma_3 &= (\sigma'_1 - \sigma_1) \tan^2\left(45^\circ - \frac{\varphi}{2}\right) \\ &= \Delta\sigma_1 \cdot \tan^2\left(45^\circ - \frac{\varphi}{2}\right). \end{aligned} \quad (3)$$

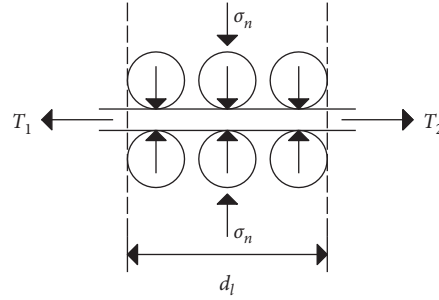


FIGURE 1: Principle of friction reinforcement.

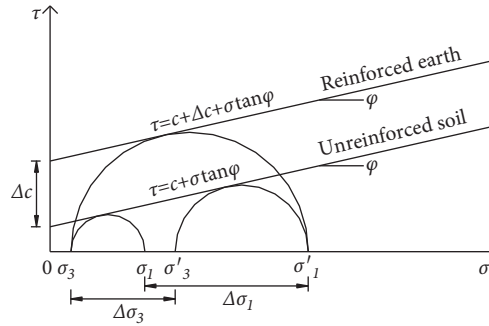


FIGURE 2: Diagram of the strength analysis of reinforced soil.

From formulas (2) and (3), we obtain

$$\Delta c = \frac{1}{2} \Delta \sigma_1 \cdot \tan\left(45^\circ - \frac{\varphi}{2}\right), \quad (4)$$

where Δc is the quasi-cohesive force, φ is the friction angle in the soil body, and $\Delta \sigma_1$ is the maximum principal stress difference.

2.2. Hydraulic Performance. Unlike other reinforced materials, the root system, as a type of active reinforcement, can play the mechanical role of reinforcement and anchoring, absorb water from different soil depths through the transpiration of plant leaves, reduce the pore water pressure of the soil, improve soil suction, and change the permeability characteristics of unsaturated soil. Therefore, the influence of the root system on soil hydraulic characteristics can be quantitatively analyzed using the unsaturated permeability theory, which is mainly reflected in two aspects.

On one hand, based on unsaturated theory, a shear strength formula considering matrix suction is established [26]:

$$\tau = c + (\sigma - \mu_a) \tan \varphi + (\mu_a - \mu_w) \tan \left[(\tan \varphi) \frac{\theta - \theta_r}{\theta_s - \theta_r} \right], \quad (5)$$

where τ , σ , c , and φ are the shear stress, principal stress, cohesion, and internal friction angle of the soil in sequence, respectively, $\mu_a - \mu_w$ is the matrix suction, μ_a is the pore-air pressure, μ_w is the pore water pressure, θ is the volumetric water content, θ_s is the saturated water content, and θ_r is the residual water content. This formula shows that plant roots

can increase soil suction, reduce the pore water pressure, and consequently increase the shear strength of the soil.

On the other hand, the relationship between suction and permeability coefficient of unsaturated soil can be described as follows:

$$K(s) = K_s \frac{\int_{\text{Ins}}^b ((\theta(e^y) - e(s))/e^y) \theta'(e^y) d_y}{\int_{\text{Ins}_{\text{ave}}}^b ((\theta(e^y) - \theta_s)/e^y) \theta'(e^y) d_y}, \quad (6)$$

where K_s is the saturated permeability coefficient, $s = \mu_a - \mu_w$, $b = \ln(10^6)$, y is the dummy variable of the suction integral, and θ' is the derivative of θ . From this formula, the soil suction is negatively related to the permeability coefficient. The change curve of various soil permeability coefficients with suction in Figure 3 shows that the permeability coefficient of soil decreases with increasing suction. Therefore, the ecological slope can increase the soil suction and reduce the permeability coefficient under the action of root suction. During rainfall, it can reduce the infiltration of rainwater and reduce the risk of soil erosion.

After the above analysis, as reinforced materials, the geogrid and root system play the role of reinforced anchors in terms of their mechanical properties, and the principle of soil fixation is identical. In actual engineering practices, due to the diversity of the plant root distribution, the root system can be intertwined with the grid through the grid gap to form a joint entity, which can limit the relative displacement of the geogrid and soil and prevent the root system from being pulled out to improve the shear strength of the soil. Simultaneously, the suction effect of the root system can

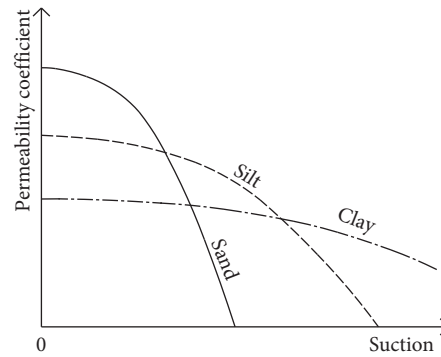


FIGURE 3: Diagram of the change in soil permeability coefficient with suction.

improve the hydraulic properties of the soil, increase the shear strength of the soil, reduce the infiltration coefficient, and reduce the harm of rainwater to the soil. In summary, the ecological slope protection method of composite vegetation with geogrids can fully utilize the reinforcing and anchoring effects of root systems and geogrids, effectively reduce the risk of soil erosion, and provide a theoretical basis for promotion.

3. Numerical Simulation of Combined Ecological Slope Protection

3.1. Engineering Background. The 10th section of the Guizhou Yushi Expressway starts from Majiao, Tianxing Township, Cengong County and ends at the Yangtang River, Tianxing Township, Cengong County, with a total length of 8.155 km. There are many deep excavation and high filling subgrades along the entire line of the tender section, with 3.47 million square meters of excavation and 3.06 million square meters of filling and rainfall conditions throughout the year. Therefore, the main technical difficulties in the construction process are abundant rainfall, difficulties associated with soil and water conservation, and more high-side and larger slopes. In addition, an urgent blockade of this project is how to adapt to local conditions in the context of green transportation, ensure the safety, stability, and green premise of the integration, optimize various protection methods, and achieve maximum economic and ecological benefits.

3.2. Establishment of the Numerical Model and Validation. MIDAS/GTS provides a slope stability analysis under various working conditions, which is widely used in slope stability calculations, and the calculation accuracy has been verified. Therefore, the finite element software Midas-GTS is used to simulate the joint ecological slope protection. A section of the slope of the Yushi Expressway in Guizhou was selected for analysis, which has a slope fill height of 6 m and a slope of 45°. To achieve maximum economic and ecological benefits, ecological protection of the composite vegetation with geogrids is performed on the slopes. The composite vegetation consists of a combination of shrubs and trees. Shrub roots are mainly distributed within 0.6 m below the slope surface. To facilitate the simulation, the arbor root

system is simplified. The main roots of the arbor are vertically distributed with a length of 3 m and a diameter of 0.1 m. The lateral roots are distributed symmetrically about the main root, parallel to the slope, with a length of 0.6 m, a diameter of 0.02 m, and a horizontal planting interval of 2 m. The geogrid is 6 m long. The layout spacing is 0.6 m. To reduce the influence of the size effect, the grid of the slope model is extended and converted according to the research of Zheng et al. on the calculation accuracy of numerical simulation [27]. The specific slope form and model dimensions are shown in Figure 4.

Due to the well-developed root system of shrubs with diverse and dense distribution patterns, they can interlock with the soil and form a joint mass. Therefore, the soil in the shrub reinforcement area is simulated in the form of a root soil complex. The Mohr–Coulomb model is used for plain soil and reinforced soil. Both geogrid and arbor root system were simulated using a separated elastic model. A normal constraint was applied around the model with a fixed constraint at the bottom and a rainfall boundary with an intensity of 5 mm/h at the top for 24 h, which was recorded every 6 h. The initial water level was 4.5 m. According to the engineering geological survey report and corresponding references, the mechanical parameters and hydraulic characteristic parameters of plain soil and reinforced soil are provided. Among them, the mechanical parameters of both geogrid and arboreal root system were obtained from indoor tensile tests, which are shown in Tables 1 and 2.

To verify the accuracy of the built numerical model, further research was performed on the joint ecological slope. The strength reduction method and stress limit equilibrium method are used to calculate the stability of the original slope. The safety factor of the slope obtained by the strength reduction method is 1.890, which is closer to the safety factor of 1.906 calculated by the stress limit equilibrium method. Thus, the numerical model can be used for the stability calculation of combined ecological slope protection.

3.3. Result Analysis. Figure 5 shows the displacement field of the original slope and ecological slope under the combined reinforcement after 24 h of rainfall. As seen from the figure, the slope displacement field considerably changes under combined ecological protection. First, in terms of displacement values, the maximum displacements of the

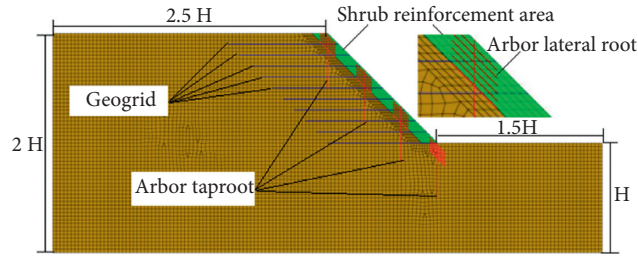


FIGURE 4: Slope model.

TABLE 1: Mechanical parameters of the materials.

Material	Volumetric weight r (kN/m ³)	Cohesion c (kPa)	Friction angle φ (°)	Elastic modulus E (MPa)	Poisson's ratio μ
Plain soil	18	10.3	22.85	4	0.3
Shrub reinforced soil	18	24.6	28.39	4.8	0.3
Arbor lateral roots	12.85	—	—	500	0.3
Geogrid	—	—	—	1500	0.23

TABLE 2: Hydraulic characteristic parameters of the soil.

Material	Fitting parameter a (kPa ⁻¹)	Fitting parameter n	θ_r (m ³ /m ³)	θ_s (m ³ /m ³)	k_s (10 ⁻⁶ m/s)
Plain soil	0.114	1.806	0.017	0.45	3.29
Shrub reinforced soil	0.176	1.798	0.018	0.456	3.18

original slope and ecological slope are 186.5 mm and 33.4 mm, respectively, i.e., the slope displacement is reduced by 82%. Second, the maximum displacement of the original slope is located at the foot of the slope, the stress is relatively concentrated, and the slope exhibits an overall slippage effect. Meanwhile, the sensitive area of the maximum displacement of the ecological slope has changed and is located in the middle and upper parts of the slope. The reason is that, under the action of rainfall, the weight of the soil sharply rises; the soil at the foot of the slope is most severely eroded by rainwater, and the original slope has an integral sliding from top to bottom. However, under the combined action of the geogrid and root system of the ecological slope, the displacement at the toe of the slope is fully restricted. Simultaneously, the suction effect of the root system reduces the pore water pressure at the foot of the slope and improves the shear strength of the soil at the foot of the slope. However, the effective stress on the tendons in the middle and upper parts of the slope is relatively small, the tendon reinforcement effect is limited, and the connection force between shrub reinforcement area and plain soil is insufficient, which can easily produce relative slip and cause shallow damage to the slope.

According to research on the mechanism of root soil fixation, considering the influence of the root system on the hydraulic characteristics of the slope, the unsaturated strength reduction method is used to calculate the slope stability under different reinforcement modes. As shown in Figure 6, under natural working conditions, the shrub reinforcement has limited effect on the slope, but the tree and geogrid reinforcement has an obvious effect. Compared with the original slope, the slope safety factor increases by 6% and 9%, respectively. In the combined form, the ecological

protection method of composite vegetation with the geogrid has the highest safety factor, which is represented by an increase of 12% relative to the reinforcement effect of a single vegetation with geogrid. Under rainfall conditions, as rainfall continued, the effect of the shrub reinforcement considerably improved, and the slope safety factor increased by 6% after 24 h of rainfall. Although the shrub reinforcement has limited contribution to the slope stability, it can effectively reduce the hazard of rainfall on the slope. Among them, the ecological protection method of composite vegetation with a geogrid still obtains the highest safety factor, which is 35% higher than that of the original slope.

Regardless of whether rainfall occurs, composite vegetation with the geogrid reinforcement mode has the best performance. Under the anchoring action of the geogrid and arbor root system, the reinforced soil in the shrub reinforcement area can be connected with the stabilizing layer, which improves the stability of the shallow soil. Simultaneously, the root system passes through the grid gap and interweaves with the grid to form a united entity. This unity effectively plays the role of geogrid, root reinforcement, and anchor, limits slope deformation, and changes the sensitive area of maximum ecological slope displacement. It can improve the stability of the slope under natural working conditions and greatly reduce the hazard of rainfall to the slope.

4. Optimization of the Combined Ecological Slope Protection

At present, most studies on the effect of ecological slope reinforcement are single-factor analyzes, while the ecological protection method of composite vegetation with geogrids

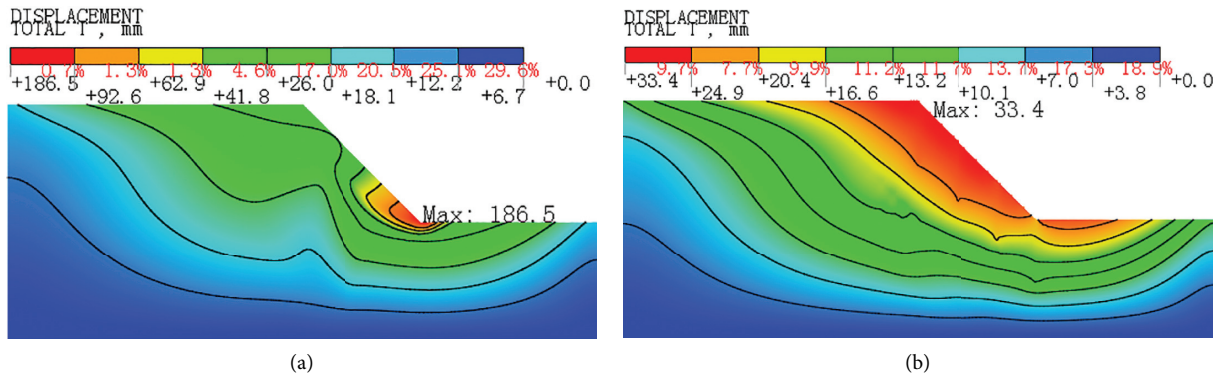


FIGURE 5: Displacement field of the original slope and ecological slope after 24 h of rainfall. (a) Original slope. (b) Ecological slope protection by composite vegetation with geogrid reinforcement.

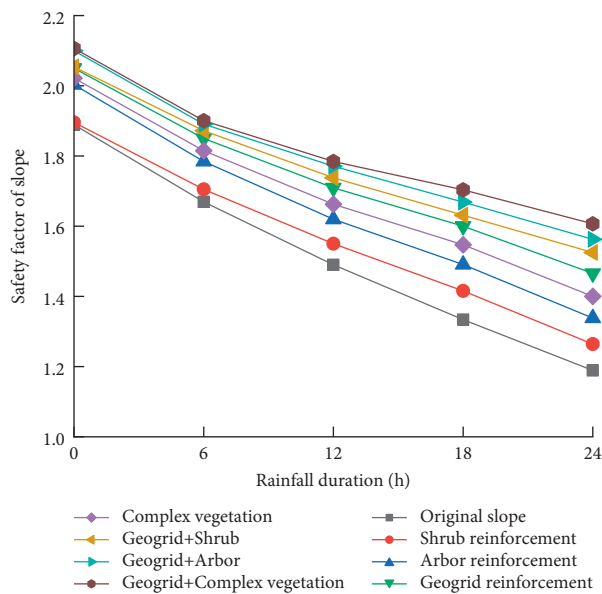


FIGURE 6: Slope stability under various protection methods.

has multiple factors and multiple levels, which affect one another. Therefore, compared with the single-factor analysis, the orthogonal model test can quantitatively calculate the degree of influence of each factor on the stability of ecological slopes under different working conditions. This process can also obtain the optimal combination form to guide the application of joint ecological slope protection technology in practical engineering.

4.1. Establishment of the Orthogonal Model. Based on the existing research, taking the shrub reinforcement depth, arbor anchoring depth, arbor distribution form, and geogrid spacing as influencing factors, we designed an orthogonal model test with 4 factors and 3 levels, as shown in Table 3. The distribution forms of trees include uniform (a), upper dense and lower sparse (b), and upper sparse and lower dense (c) distributions. Specific planting methods are shown in Figure 7.

4.2. Orthogonal Test Results. Nine combinations of 4 factors and 3 levels under different working conditions were numerically calculated, and the results are shown in Table 4. The calculation results are analyzed in the range in Table 5. A larger extreme difference indicates that this factor has a greater influence on the slope stability, which can be used to obtain the degree of influence of different factors on the ecological slope stability under different working conditions and derive the optimal combination form, which is reported in Table 5.

Under natural working conditions, trees have the largest extreme difference in anchorage depth, and shrubs have the smallest extreme difference in reinforcement depth. Therefore, the degree of influence of each factor on the stability of ecological slopes is as follows: depth of anchorage of trees > spacing of geogrid > form of distribution of trees > depth of reinforcement of shrubs. Meanwhile, it can be seen from Figure 8(a), the slope safety coefficient first increases and subsequently decreases with increasing

TABLE 3: Orthogonal design level of optimized parameters (unit: m).

Level	Optimization parameters			
	Shrub reinforcement depth	Arbor anchoring depth	Arbor distribution form	Geogrid spacing
1	0.2	1	a	0.4
2	0.4	2	b	0.6
3	0.6	3	c	0.8

reinforcement depths; the slope safety increases with increasing arbor anchorage depths; the slope safety first increases and then stabilizes with the decrease of the geogrid spacing. The size of the slope safety coefficient under different forms of arbor distribution follows the following order: upper sparse and lower dense > uniform distribution > upper dense and lower sparse. The above result shows that the stability of shallow slopes can be improved with increasing reinforcement depth. However, when the influence depth of reinforced soil is too large, the intermediate connection force is insufficient, which increases the risk of sliding along shallow slopes and induces shallow slope instability. Increasing the anchoring depth and reducing the spacing of the geogrid can improve the reinforced anchoring effect of the reinforced material. However, when the spacing of the grids is reduced, the reinforcement effect will not improve. Considering the economic benefits of the project, the spacing of grating should be 0.6 m. In addition, the sensitive area of the slope safety factor is at the foot of the slope, and the arbor adopts the upper sparse and lower dense distribution, which can effectively play the role of anchoring. In summary, under natural working conditions, the optimal combination form is as follows: the reinforcement depth is 0.4 m, the anchorage depth is 3 m, the arbor is sparse on the top and dense at the bottom, and the grid spacing is 0.6 m.

Under rainfall conditions, the degree of influence of each factor on the stability of ecological slopes is as follows: depth of anchorage of trees > depth of reinforcement of shrubs > spacing of geogrid > form of distribution of trees. The extreme difference in shrub reinforcement depth was greatly enhanced. Thus, the effect of shrub reinforcement on the hydraulic properties of the slope was considerably greater than its mechanical properties. Under joint ecological protection, shrub reinforcement can effectively reduce the hazard of rainfall on the slope stability and improve the hydraulic characteristics of the slope. It can be seen from Figure 8(b) that slope safety factor, shrub reinforcement depth, arbor anchorage depth, and geogrid spacing are linearly related, which obviously differs from the trend of natural working conditions. A greater depth of shrub reinforcement corresponds to a greater degree of improvement in the hydraulic properties of the slope and better protection against rainfall hazards. In other words, when planting shrubs in rainfall areas, vegetation with more developed root systems should be used. Simultaneously, rainfall increases the tendency of relative displacement between the soil and the grid. This reinforcement effect can be effectively improved by reducing the grid spacing, so the grid spacing should be 0.4 m. Under different arbor distribution forms, the slope safety factor follows the following order: upper sparse and lower dense > upper dense and

lower sparse > evenly distributed. The optimal reinforcement effect can be obtained with the upper sparse and lower dense planting method. The root system in the lower part more easily passes through the plastic zone of the slope and gives full play to the anchoring effect of the root system. However, under the action of rainfall, the displacement-sensitive area of the ecological slope is changed, and the maximum displacement is located in the middle and upper parts of the slope. Therefore, unlike the natural working condition, the planting method of upper density and lower sparsity can improve the connection force between the shallow soil and the stable layer in the middle and upper parts of the slope, prevents shallow damage to the slope, and is better than the uniform distribution. In summary, under rainfall conditions, the optimal combination form is as follows: reinforcement depth of 0.6 m, anchorage depth of 3 m, sparse arbor at the top, dense arbor at the bottom, and grid spacing of 0.4 m.

The above analysis shows that, under natural and rainfall conditions, the degree of influence of various factors on the stability of ecological slopes is very different, and the obtained optimal combination form is also different. Therefore, for the combination forms of ecological slopes in different regions, the corresponding optimal combination forms should be formulated according to the local hydrogeological conditions.

4.3. Practical Engineering Application. We applied the optimal combination form obtained from the orthogonal model test to the corresponding actual project to verify the superiority of the combination.

According to research on the reinforcement mode of composite vegetation with geogrids, the combined ecological protection method can be applied to the side slope project of the Yushi Expressway in Guizhou. Therefore, a geogrid was laid on the filling section of a subgrade side slope, and a vegetation composite consisting of shrubs and trees was planted on the slope. The grid spacing was 0.4 m, and trees were planted with sparse tops and dense bottoms. Figure 9 shows a site picture of ecological protection in the bid section. By monitoring the finished slope project, we found that, in the early stage of planting, the reinforcement of the geogrid improved the slope stability. As the vegetation growth period progressed, the root system passed through the mesh of the geogrid. The vegetation and geogrid were interweaved and jointly reinforced and anchored. Hence, the reinforcement of composite vegetation and ecological benefits considerably improved. Under rainfall conditions, shrubs could effectively weaken splash erosion and reduce the scouring of slopes by rainwater. No obvious soil erosion

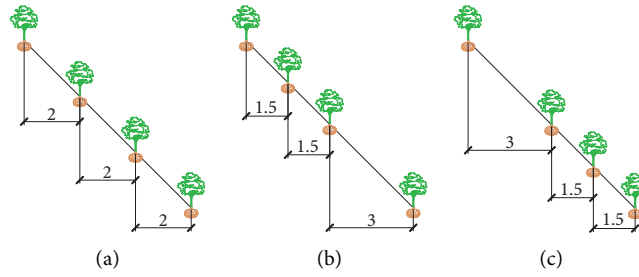


FIGURE 7: Schematic diagram of the tree planting pattern (unit: m).

TABLE 4: Orthogonal test results of the slope safety factor.

Combining forms	Optimization parameters				Safety factor of slope	
	Shrub reinforcement depth	Arbor anchoring depth	Arbor distribution form	Geogrid spacing	Rainfall 0 h	Rainfall 24 h
1	0.2	1	a	0.4	2.075	1.522
2	0.2	2	b	0.6	2.094	1.529
3	0.2	3	c	0.8	2.100	1.563
4	0.4	1	b	0.8	2.063	1.538
5	0.4	2	c	0.4	2.101	1.556
6	0.4	3	a	0.6	2.109	1.581
7	0.6	1	c	0.6	2.078	1.563
8	0.6	2	a	0.8	2.088	1.566
9	0.6	3	b	0.4	2.105	1.613

TABLE 5: Range analysis of the slope safety factor.

Rainfall duration (h)	Average water	Shrub reinforcement depth	Arbor anchoring depth	Arbor distribution form	Geogrid spacing
0	K1	2.090	2.072	2.091	2.094
	K2	2.091	2.094	2.087	2.094
	K3	2.090	2.105	2.093	2.084
	Range	0.001	0.033	0.006	0.010
24	K1	1.538	1.541	1.556	1.564
	K2	1.558	1.550	1.560	1.558
	K3	1.581	1.586	1.561	1.556
	Range	0.043	0.045	0.005	0.008

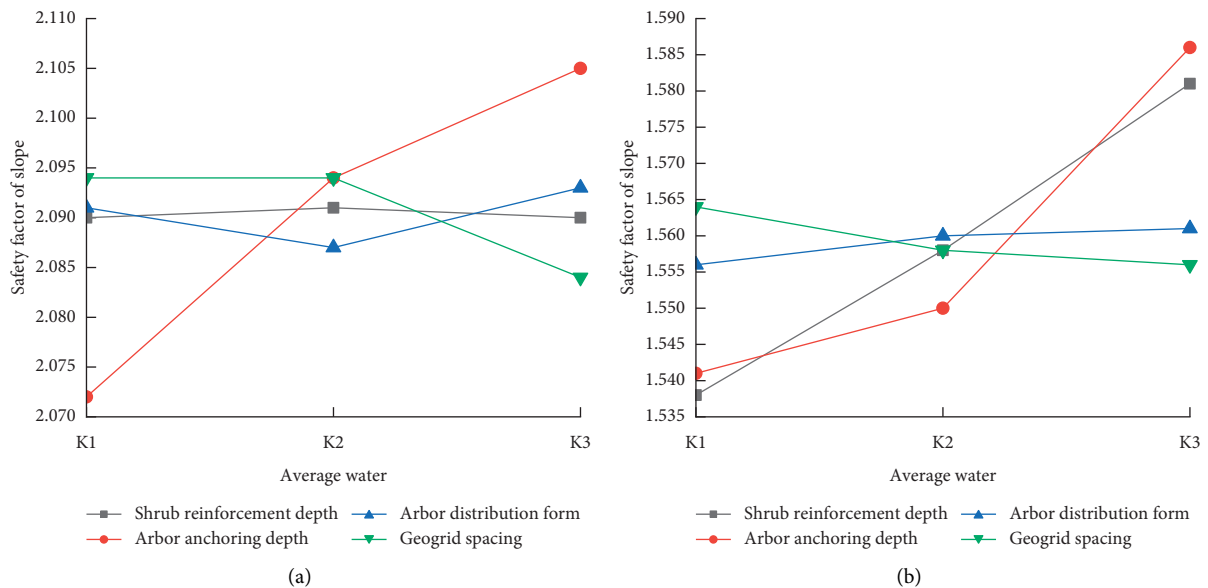


FIGURE 8: Curves of slope safety factor varying with the average level of various factors under different working conditions. (a) Rainfall 0 h. (b) Rainfall 24 h.

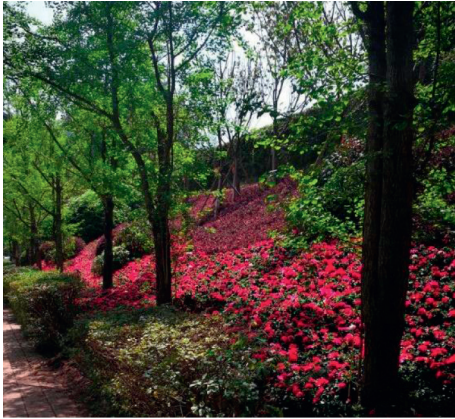


FIGURE 9: Practical application of joint ecological protection.

occurred, and the local ecological environment was quickly restored, which achieved good reinforcement and demonstrates the ecological benefits of the project.

5. Conclusions

For the ecological slope protection technology of composite vegetation with a geogrid, theoretical analysis, numerical simulation, optimization design, and practical application were performed. The mechanical and hydraulic characteristics of the combined ecological slope were comprehensively evaluated. The impacts of the shrub shallow root reinforcement, arbor deep root anchoring, and combined geogrid reinforcement on the stability of the slope were quantified. The design of the combined ecological slope was optimized. All of this work will contribute to the design and application of ecological slope engineering. The study indicates that

- (1) Based on the reinforced soil theory and unsaturated seepage theory, we demonstrated the feasibility of using composite vegetation of shrubs and trees to reinforce the slope with a geogrid.
- (2) The ecological protection method of composite vegetation with geogrids is obviously better than the single reinforcement method. The maximum displacement of the ecological slope under rainfall conditions decreased by 82% compared to the original slope, and the overall stability increased by 35%.
- (3) The shrub reinforcement has a much greater effect on the hydraulic characteristics of the slope than its mechanical characteristics. The anchoring depth of the arbor root system plays a key role in ensuring slope stability. The encryption of geogrid spacing can reduce the hazard of rainfall to the slope. According to the degree of influence of various factors on the stability of ecological slopes, the optimal combination form under different working conditions is obtained. The optimal combination form is applied to the actual project, and good reinforcement and ecological benefits have been achieved.

- (4) Due to the diversity of root distribution morphology, this study simplified the arbor root system, which can only reflect the spatial relationship between the root system and the geogrid. Therefore, future research will examine how to more truly reflect the actual effect of the joint reinforcement of the root system and grid.

Data Availability

The data used to support the findings of this study are available from the corresponding author upon request.

Conflicts of Interest

The authors declare that they have no conflicts of interest.

Acknowledgments

This research was supported by the General Project of the National Natural Science Foundation of China (51978249).


References

- [1] L. J. Guo, R. M. Liu, C. Men et al., "Multiscale spatiotemporal characteristics of landscape patterns, hotspots, and influencing factors for soil erosion," *Science of the Total Environment*, vol. 779, Article ID 146474, 2021.
- [2] B. Y. Guo, Y. Q. Niu, V. S. Mantravad, L. Zhang, and G. Z. Liu, "The variation of rainfall runoff after vegetation restoration in upper reaches of the Yellow river by the remote sensing technology," *Environmental Science and Pollution Research*, vol. 2, 2021.
- [3] Y.-J. Kim, A. R. Kotwal, B.-Y. Cho, J. Wilde, and B. H. You, "Geosynthetic reinforced steep slopes: current technology in the United States," *Applied Sciences*, vol. 9, no. 10, Article ID 9102008, 2019.
- [4] Y. Sun, H. Xu, P. Gu, and W. Hu, "Application of FBG sensing technology in stability analysis of geogrid-reinforced slope," *Sensors (Basel, Switzerland)*, vol. 17, no. 3, p. 597, 2017.
- [5] M. B. Guo, L. Song, J. Liu, and Y. F. Duan, "Analysis of mechanical behavior of geogrid-reinforced steep embankment," *Journal of Shihezi University (Natural Science)*, vol. 37, no. 6, pp. 708–713, 2019, in Chinese.
- [6] R. Zhang, M.-x. Long, T. Lan, J.-l. Zheng, and C. Geoff, "Stability analysis method of geogrid reinforced expansive soil slopes and its engineering application," *Journal of Central South University*, vol. 27, no. 7, pp. 1965–1980, 2020.
- [7] L. S. Shen, G. Q. Yang, H. T. Cheng, R. J. Zheng, and J. C. Chen, "Optimization technology for geogrid-reinforced subgrade widening projects of highways," *Chinese Journal of Geotechnical Engineering*, vol. 35, no. 74, pp. 789–793, 2013, in Chinese.
- [8] W. H. Yang, D. W. Zhang, Q. Yan, and Z. L. Mao, "Numerical analysis on stability of slope reinforced by combination of deep and shallow roots," *Journal of Southeast University (Natural Science Edition)*, vol. 50, no. 1, pp. 161–168, 2020, in Chinese.
- [9] L. J. Waldron, "The shear resistance of root-permeated homogeneous and stratified soil," *Soil Science Society of America Journal*, vol. 41, no. 5, pp. 843–849, 1977.

- [10] D. H. Gray and T. Al-Refeai, "Behavior of fabric-versus fiber-reinforced sand," *Journal of Geotechnical Engineering*, vol. 112, no. 8, pp. 804–820, 1986.
- [11] C. F. Chen, H. X. Liu, and Y. P. Li, "Study on grassroots-reinforced soil by laboratory triaxial test," *Rock and Soil Mechanics*, vol. 28, pp. 2041–2045, 2007, in Chinese.
- [12] L.-j. Su, B.-l. Hu, Q.-j. Xie, F.-w. Yu, and C.-l. Zhang, "Experimental and theoretical study of mechanical properties of root-soil interface for slope protection," *Journal of Mountain Science*, vol. 17, no. 11, pp. 2784–2795, 2020.
- [13] E. Abdi, B. Majnounian, M. Genet, and H. Rahimi, "Quantifying the effects of root reinforcement of Persian ironwood (*Parrotia persica*) on slope stability; a case study: hillslope of Hyrcanian forests, northern Iran," *Ecological Engineering*, vol. 36, no. 10, pp. 1409–1416, 2010.
- [14] J. J. Roering, K. M. Schmidt, J. D. Stock, W. E. Dietrich, and D. R. Montgomery, "Shallow landsliding, root reinforcement, and the spatial distribution of trees in the Oregon coast range," *Canadian Geotechnical Journal*, vol. 40, no. 2, pp. 237–253, 2003.
- [15] L. Zeng, H.-b. Bian, Z.-n. Shi, and Z.-m. He, "Forming condition of transient saturated zone and its distribution in residual slope under rainfall conditions," *Journal of Central South University*, vol. 24, no. 8, pp. 1866–1880, 2017.
- [16] K.-H. Yang, J. N. Thuo, J.-W. Chen, and C.-N. Liu, "Failure investigation of a geosynthetic-reinforced soil slope subjected to rainfall," *Geosynthetics International*, vol. 26, no. 1, pp. 42–65, 2019.
- [17] X. Zhang, L. Huang, Y. J. Hou, B. Wang, B. H. Xue, and M. S. Shi, "Study on the stability of the geogrids-reinforced earth slope under the coupling effect of rainfall and earthquake," *Mathematical Problems in Engineering*, vol. 2020, Article ID 5182537, 11 pages, 2020.
- [18] J. J. Zhen, H. Yu, Z. S. Guo, and W. Z. Chao, "Numerical analysis of stability of widened embankment under rainfall conditions," *Journal of Hunan University (Natural Science Edition)*, vol. 44, no. 7, pp. 150–155, 2017, in Chinese.
- [19] P. Zhang, Y. F. Xu, and X. T. Wu, "Effects of water uptake by plant roots on slope stability," *Journal of Yangtze River Scientific Research Institute*, vol. 37, no. 9, pp. 120–125, 2020, in Chinese.
- [20] M. S. Wu, C. Zhou, L. Wang, and C. M. Tan, "Numerical simulation of the influence of roots and fissures on hydraulic and mechanical characteristics of the soil," *Rock and Soil Mechanics*, vol. 40, no. s1, pp. 519–526, 2019, in Chinese.
- [21] C. W. W. Ng, K. X. Woon, A. K. Leung, and L. M. Chu, "Experimental investigation of induced suction distribution in a grass-covered soil," *Ecological Engineering*, vol. 52, no. 2, pp. 219–223, 2013.
- [22] H. X. Wang, Y. L. He, Z. F. Shang, C. P. Han, and Y. L. Wang, "Model test of the reinforcement of surface soil by plant roots under the influence of precipitation," *Advances in Materials Science and Engineering*, vol. 2018, Article ID 3625053, 12 pages, 2018.
- [23] S. Y. Meng, *Study on Unsaturated Infiltration Model and Ecological Reinforcement Mechanism of Slope under Rainfall Condition*, China University of Geosciences, Beijing, China, 2019, in Chinese.
- [24] W. W. N. Charles, "Atmosphere-plant-soil interactions: theories and mechanisms," *Chinese Journal of Geotechnical Engineering*, vol. 39, no. 1, pp. 1–47, 2017, in Chinese.
- [25] X. R. Song, M. S. Huang, S. Q. He et al., "Erosion control treatment using geocell and wheat straw for slope protection," *Advances in Civil Engineering*, vol. 2021, Article ID 5553221, 12 pages, 2021.
- [26] D. G. Fredlund, N. R. Morgenstern, and R. A. Widger, "The shear strength of unsaturated soils," *Canadian Geotechnical Journal*, vol. 15, no. 3, pp. 313–321, 1978.
- [27] Y. R. Zheng, S. Y. Zhao, and L. Y. Zhang, "Slope stability analysis by strength reduction FEM," *Chinese Engineering Science*, vol. 4, no. 10, 2002, in Chinese.

Research Article

Welding Deformation of Hydraulic Support Measurements by Using FBG Sensors

Shangyu Du ^{1,2,3}, Guofa Wang,^{1,2} Yajun Xu,^{2,3} Ying Ma,^{2,3} Desheng Zhang,^{2,3} Qiang Ma,¹ and Xingtong Yue⁴

¹CCTEG Coal Research Institute, Beijing 100013, China

²Tiandi Science and Technology Co., Ltd., Beijing 100013, China

³CCTEG Coal Mining Research Institute, Beijing 100013, China

⁴Ansteel Beijing Research Institute Co., Ltd., Beijing 102209, China

Correspondence should be addressed to Shangyu Du; dusy6509@163.com

Received 15 July 2021; Accepted 30 July 2021; Published 4 August 2021

Academic Editor: Dezhong Kong

Copyright © 2021 Shangyu Du et al. This is an open access article distributed under the Creative Commons Attribution License, which permits unrestricted use, distribution, and reproduction in any medium, provided the original work is properly cited.

The welding deformation and cracking of hydraulic support have always been an important issue that impacts product quality and performance in the industry. In order to quantify the deformation of the welding seam of the reverse four-bar linkage hydraulic support under loading conditions, a real-time weld monitoring system based on sensitive fiber Bragg grating sensors is designed. The strength test and the cycle life test of the top coal caving reverse four-link support with four typical eccentric loads were conducted, respectively. The strength test results prove that the fiber Bragg grating sensor is accurate enough to measure welding deformation of hydraulic support; the measurement resolution reaches $0.1\ \mu\text{m}$. The eccentric load experiment produces the reverse four-bar torsion, especially when the top beam is at a low position; the maximum deformation of the weld is $100\ \mu\text{m}$. In the cycle test, a phenomenon has been captured, i.e., the welds present a baseline shift along with the cyclic load and even jump. It indicates that the hydraulic support changes from one stable state to another stable state. This work not only provides a feasible solution for welding deformation monitoring but also provides a possibility for the whole life cycle monitoring of hydraulic supports.

1. Introduction

According to the latest World Energy Data Statistics Report for 2019 provided by the British company BP, the total annual global power generation in 2019 was 27004.7 TWh. Among the fossil energy used for power generation in the world, coal supports 30% of the total global power generation, which is still an important part of the world's energy. At present, the underground coal mines are mainly mined in the form of comprehensive mechanized coal mining, using highly automated "three fully mechanized mining machines," namely, shearer, scraper conveyors, and hydraulic supports [1]. The hydraulic support plays a vital role in supporting the roof of the coal mining face and protecting the equipment and workers of the coal mining face [2].

The top coal transition support is one of the most important support equipment for comprehensive mechanized top coal mining. Its performance and quality directly determine the output and efficiency of the fully mechanized caving face [3]. The mechanical characteristics of the reverse four-bar linkage mechanism of the transition support are better than those of the positive four-bar linkage transition support, and it is more suitable for top coal mining. However, most of the top coal mining is faced with unfavourable situations such as large thickness drop and complex geological conditions, making it difficult for traditional simulation to obtain force characteristics close to the actual application. According to the actual application of the reverse four-bar linkage structure of the top coal caving transition support underground, the weld seam of the four-bar linkage structure

often deforms or even cracks, which poses a serious threat to underground safety production.

The requirements for hydraulic support consist of rational structure, sufficient support resistance force, stable and shock resistance, the sustainability of highly efficient coal discharge, and high coal recovery [4, 5]. Zhao et al. analysed the structural characteristics of hydraulic supports with box-type structures based on simulation, whose results show structural stress concentration is the main factor leading to the fatigue damage of hydraulic supports [6]. Liu and Junqing Liu analyse structured statics and transient dynamics of the hydraulic support strength test under base torsion by ANSYS software [7]. Fu Fang et al. compared using automatic TANDEM twin-wire welding and twin-wire gas metal welding (GMAW) to weld Q690 steel, and pointed that TANDEM twin-wire welding is very suitable in the welding of Q690 used in the hydraulic support [8].

Welding deformation and cracking of hydraulic support structural parts have always been an important issue that impacts product quality and performance in the industry. The shutdown of the working face caused by structural cracking is an important reason for users' dissatisfaction with product performance [9]. The hydraulic support structure belongs to a multichamber box girder structure composed of plates and profiles. The number of welds is densely arranged; the size of the welds is large; the structural stress concentration is serious, and the residual stress distribution is complex, which lead to hydraulic support working in an unstable state [9, 10], especially for the top coal caving transition hydraulic support with reverse four-link structure. In the actual work of the reverse four-link structure, the welding seam stretching and even cracking caused by the unbalanced top and floor pressure cannot be calculated by simulation. Due to the complicated wiring, traditional resistive strain sensors are not suitable for long-term monitoring underground, especially in humid environments.

With the development of sensing technology, researchers begin to use modern sensing technology to measure the pressure, stress distribution, posture, and deformation of hydraulic supports in actual work [11–13]. For instance, the displacement sensor and pressure sensor are equipped with modern hydraulic support to quantify the working resistance [14]; a fiber Bragg grating (FBG) tilt sensor based on double equal strength beams is designed and used to monitor the posture of hydraulic supports [15]; Zhen and Ma et al. reported optical FBG sensors for aircraft wing shape measurement [16]. Optical fiber sensing technology is a sensing technology that uses light propagation path as a medium to sense external strain [17], magnetic field [18], temperature [19], vibration [20], and other information. Because of its passive, anti-interference, anticorrosion, and small size, it has been widely used in important fields such as petrochemical [21], aerospace [22], biomedicine [23], national defense and military [24], and environmental monitoring [25].

To reveal the deformation of the welding seam of the reverse four-bar linkage hydraulic support under loading conditions, in this paper, we adopted an FBG sensor to

measure the deformation of the weld of the reverse four-bar linkage. Furthermore, we designed a real-time weld monitoring system, based on a fiber optic demodulator with sensitive FBG sensors and a NI DAQ-6002 board, which is used to sample the pressure of hydraulic support. They were synchronized by the inner timer of the host computer.

To quantify the relationship between the welding deformation and the pressure of the load under different working conditions, the strength test and the cycle life test of the top coal caving reverse four-link support with four typical eccentric load were conducted, respectively. The results of strength test show that the eccentric load experiment produces the reverse four-bar torsion; the maximum deformation of the weld reaches $100\ \mu\text{m}$. In the cycle test, we found that the welding deformation presents a baseline shift along with the cyclic load, and even jumps.

2. Materials and Methods

2.1. Fiber Bragg Grating Sensor. In 1978, Canadian physicist Ken Hill demonstrated the grating effect for the first time [26]. The principle of fiber grating is shown in Figure 1. An intense ultraviolet laser is used in “writing” systematic variation of refractive index into the core of the special optical fiber. The Bragg gratings can be realized using microfabrication methods which can create refractive index modulation along the beam propagation direction. Besides the FBGs based on refractive index modulation, they can be also realized using heterocore fiber structures, taper structures, cladding removal, microbending structure, and macrobending structure [27]. Then, a broadband laser light source is used to transmit a broadband spectrum along a section of the fiber. Λ_a is the constant nominal period of refractive index modulation; after the light passes through the FBG, a certain bandwidth λ_a corresponding to Λ_a is reflected. The rest of the light continues propagating forward, the reflected light is separated from the incident light by the optical coupler, and then the light sensor is used to monitor the reflected light. When the FBG is squeezed or stretched by stress or temperature, the frequency of the reflected light will shift left to be λ_b or shift right to be λ_c . Thus, FBG can be used as a sensor to sense temperature and strain.

2.2. Deformation Sensor with FBG. In our measurement, a sensitive sensor, Osc3110, made by Macron Optics company is adopted. The Osc3110 Strain Gage is shown in Figure 2, which is a spot-welded steel using a capacitive-discharge spot welder. The length of the optical strain gate is 2.38 cm and the spot weldable areas are arranged at both ends of the gate. Osc3110 is connected with a fiber demodulator by the optical fiber. Although osc3110 is a strain sensor, its structure is suitable for measuring the deformation. Due to the uniformly forced among the optical strain gate, it is reasonable to quantify the deformation of the welds on the hydraulic support.

Specifically, we utilize the parameters of the sensors to explain how we quantify the welding deformation by

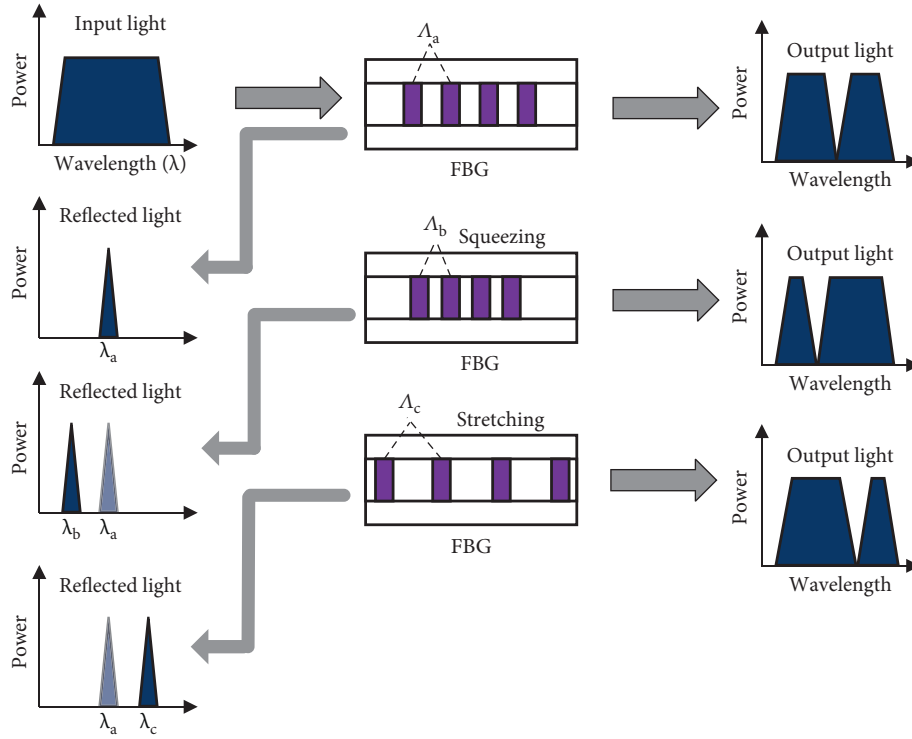


FIGURE 1: FBG principle.

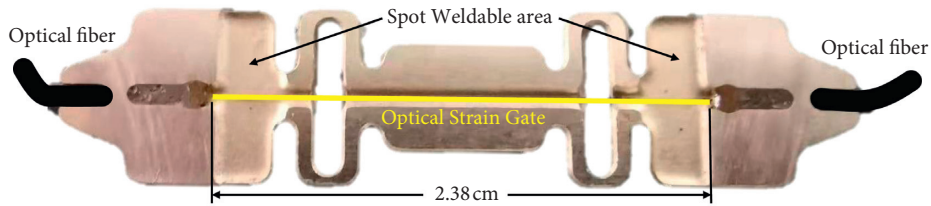


FIGURE 2: Deformation sensor.

Osc3110. According to the sensors' datasheets, we obtain the parameters of the five sensors shown in Table 1, where F_G is gate factor, λ_0 is the nominal wavelength, C_1 is gate constant 1, and C_2 is gate constant 2.

Equation (1) introduces the relationship between the strain ϵ and wavelength shift $\Delta\lambda$; here ϵ_{TO} indicates thermally induced apparent strain. The FBGs, which are based on the strain gages, respond to both strain and temperature. Thus, ϵ_{TO} , shown in equation (2), is used to express how the temperature affects the strain measurement, where ΔT is the temperature change and CTE_S is 13.3 ppm/°C.

$$\epsilon = \frac{(\Delta\lambda/\lambda_0) \times 10^6}{F_G - \epsilon_{TO}}, \quad (1)$$

$$\epsilon_{TO} = \Delta T \left[\frac{C_1}{F_G} + CTE_S - C_2 \right]. \quad (2)$$

The temperature of the laboratory remains 12°C, leading to ΔT as 10°C. Substituting the values of Table 1 into equation (2), we get ϵ_{TO} as 62.17 μm . Although ϵ_{TO}

represents a large number, the temperature of the laboratory can be viewed as constant; then ϵ_{TO} is subtracted as a zero bias.

To measure the deformation of the weld, we need to transform strain into deformation. Here, the length of the optical strain gate L is 2.38 cm with a reasonable approximation that the optical strain gate is uniformly stressed; then we can get the expression of deformation d as follows:

$$d = \epsilon \times L. \quad (3)$$

So far, we have elaborated on the principle of measuring weld seams with FBG sensors.

2.3. Setup. In our experiments, we use a reverse four-bar transition support ZFG10000/23/38 for top coal caving as the research object. We chose several welds that often cracked when the reverse four-bar linkage is used in underground applications. In order to clearly show the sensor installation location, a 3D model of the support and the layout of measuring points are shown in Figure 3. To study

TABLE 1: Parameters of Osc3110.

Sensors	F_G	λ_0	C_1	C_2
FBG1	0.89 at 22°C	1550.83 nm at 22°C	6.156 $\mu\text{m}/\text{m}$ at 22°C	0.7 $\mu\text{m}/\text{m}$
FBG2	0.89 at 22°C	1552.58 nm at 22°C	6.156 $\mu\text{m}/\text{m}$ at 22°C	0.7 $\mu\text{m}/\text{m}$
FBG3	0.89 at 22°C	1549.75 nm at 22°C	6.156 $\mu\text{m}/\text{m}$ at 22°C	0.7 $\mu\text{m}/\text{m}$
FBG4	0.89 at 22°C	1558.70 nm at 22°C	6.156 $\mu\text{m}/\text{m}$ at 22°C	0.7 $\mu\text{m}/\text{m}$
FBG5	0.89 at 22°C	1556.80 nm at 25°C	6.156 $\mu\text{m}/\text{m}$ at 22°C	0.7 $\mu\text{m}/\text{m}$

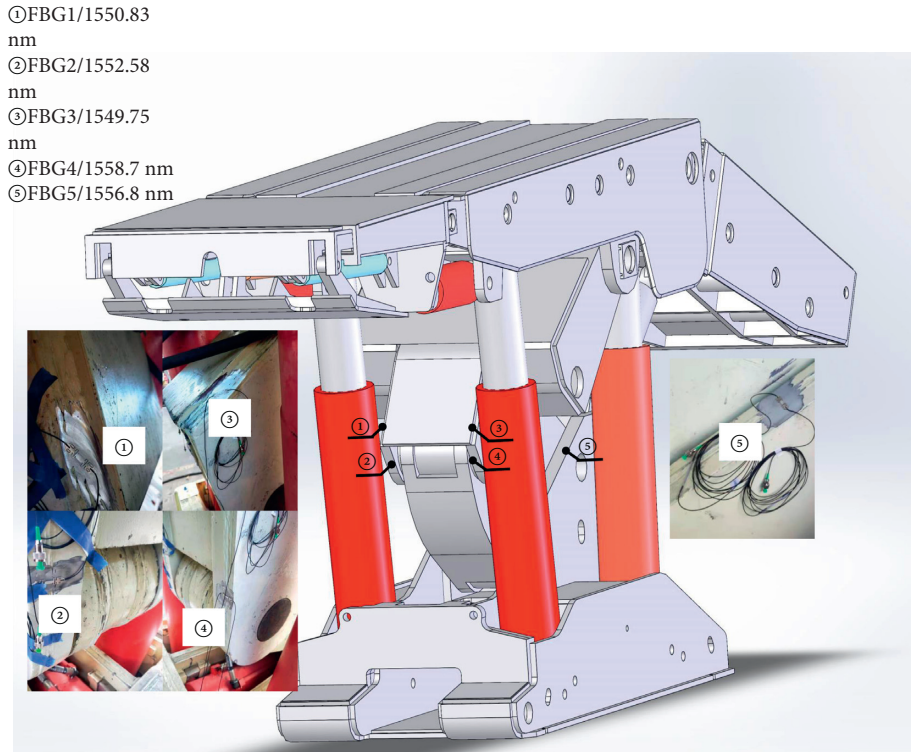


FIGURE 3: The layout of measuring points and 3D model of ZFG10000/23/38.

the deformation of the key welds of the reverse four-bar linkage under eccentric load experimental conditions, 5 FBG sensors are spot-welded cross the welds and their initial wavelengths are shown in the upper left corner of Figure 3.

To reveal how the deformation of the weld on the four-bar linkage changes with the loading pressure in the eccentric load experiment, a synchronized measurement system for hydraulic pressure and welding seam (Figure 4) was designed. The measurement system contains a hydraulic pressure measurement unit and an optical fiber data acquisition unit, and they are synchronized by the timestamp of the host computer. In the hydraulic pressure measurement unit, a pressure sensor with the precision of 0.5% F.S and the range of 0–60 MPa is adopted; then NI DAQ-USB-6002 is programmed to capture the hydraulic pressure data with sample rate 1 kHz. In the optical fiber data acquisition unit, we use optical strain gate Osc3120 series as our sensors as well as an optical spectrum analyser, operated by the MOI-ENLIGHT software on the host computer, to capture optical fiber signal. The optical spectrum analyser is an SM125-500 FBG static demodulator (produced by Micron

Optics, Inc., USA). Its main technical parameters are as follows: the wavelength scanning ranges from 1510 nm to 1590 nm, scanning frequency is 2 Hz, the wavelength resolution is 1 pm, and the sample rate is 1 kHz.

In the series of loading tests on the main structural parts of the hydraulic support, the high and low top beam eccentric loading test has the most severe test on the reverse four-bar weld. Here, we conduct four sets of trials: (1) left side eccentric loading of the top beam at the low position; (2) right side eccentric loading of the top beam at the low position; (3) left side eccentric loading of the top beam at the high position; (4) right side eccentric loading of the top beam at the high position. The loading diagram and block location are shown in Figure 5.

3. Results

3.1. Hydraulic Pressure Measurement. The measurements in our research are performed in the test bench of Safety Access Analysis and Verification Laboratory for Mine Support Equipment. The test bench applies pressure to the hydraulic

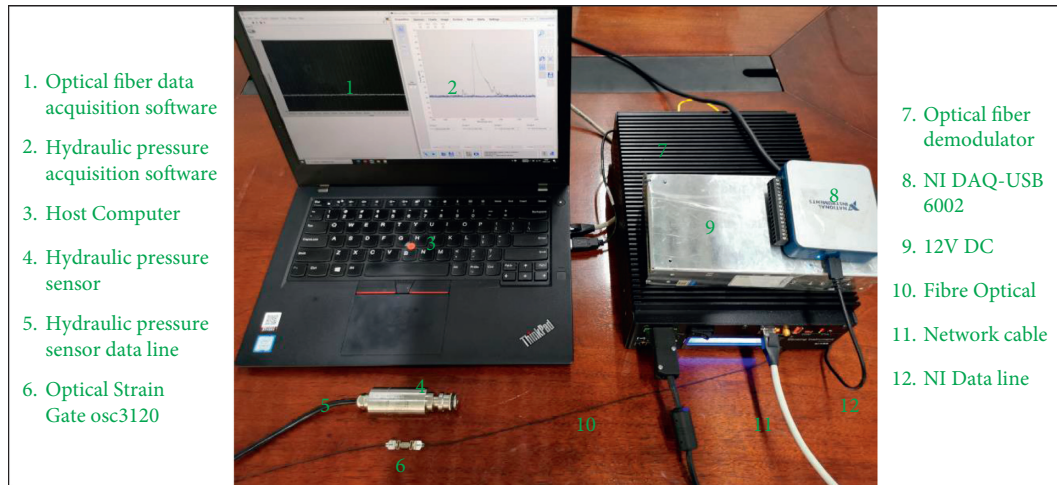


FIGURE 4: The synchronized measurement system for hydraulic pressure and welding seam.

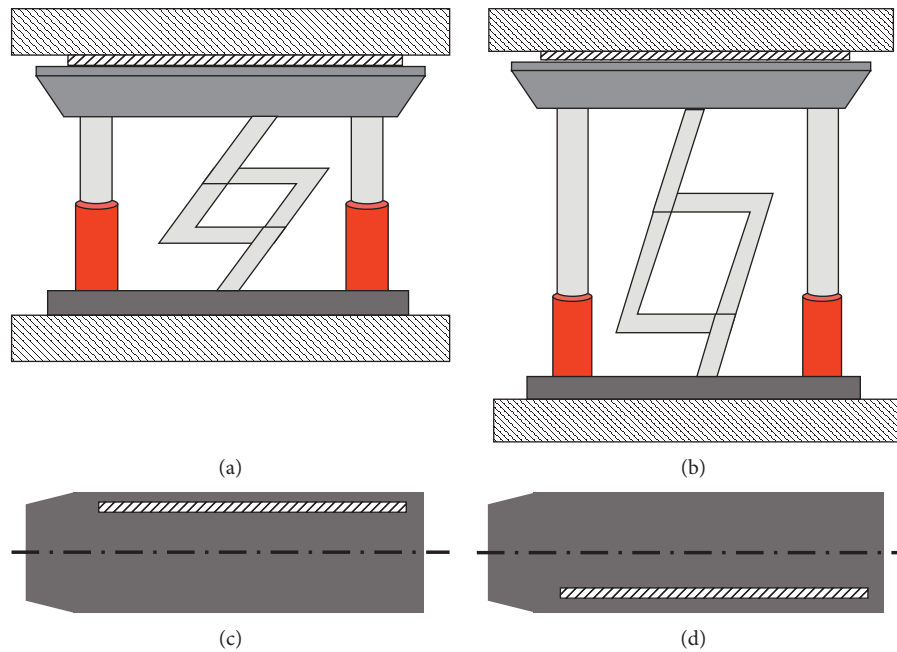


FIGURE 5: Loading diagram and block position. (a) Top beam at the low position. (b) Top beam at the high position. (c) The block at the left side of the top beam. (d) The block at the right side of the top beam.

support and the pressure sensor is connected to the hydraulic support through a three-way valve. Two top beam eccentric loading experiments, i.e., top beam at the high position and low position, are performed, respectively. And the hydraulic pressure is recorded (shown in Figure 6) by the synchronized measurement system which is introduced in Figure 4. The hydraulic pressure waveform in Figure 6(a) is used for the cycle life test of hydraulic support when its top beam is at a high position. From Figure 6(a), we can tell that the period of the waveform is 10 s, and the hydraulic pressure starts approximately at 31 MPa and then increases to 43.7 MPa and keeps at 2 s, dropping to 31 MPa eventually. Besides, in Figure 6(b), the hydraulic pressure varies from

23 MPa to 34 MPa, which is used for the cycle life test of the top beam at a low position.

3.2. Welding Deformation of Eccentric Loading with the Top Beam at a High Position. We have already detailed the measuring principle of weld deformation above. To study the deformation of the five welds with pressure loading, we trace the whole process of pressure loading; i.e., (1) hydraulic pressure stays zero; (2) hydraulic pressure increases slowly to 31 MPa; (3) hydraulic pressure varies periodically between 31 MPa and 43.7 MPa as shown in Figure 6(a). From Figure 7, we can tell that the five deformations of weld start

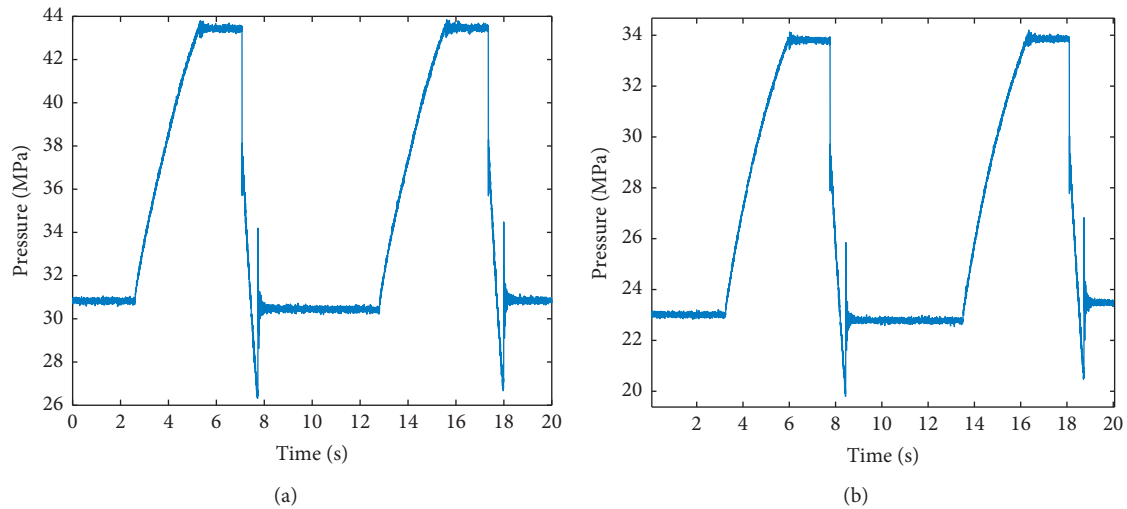


FIGURE 6: Hydraulic pressure waveform. (a) Top beam at the high position. (b) Top beam at the low position.

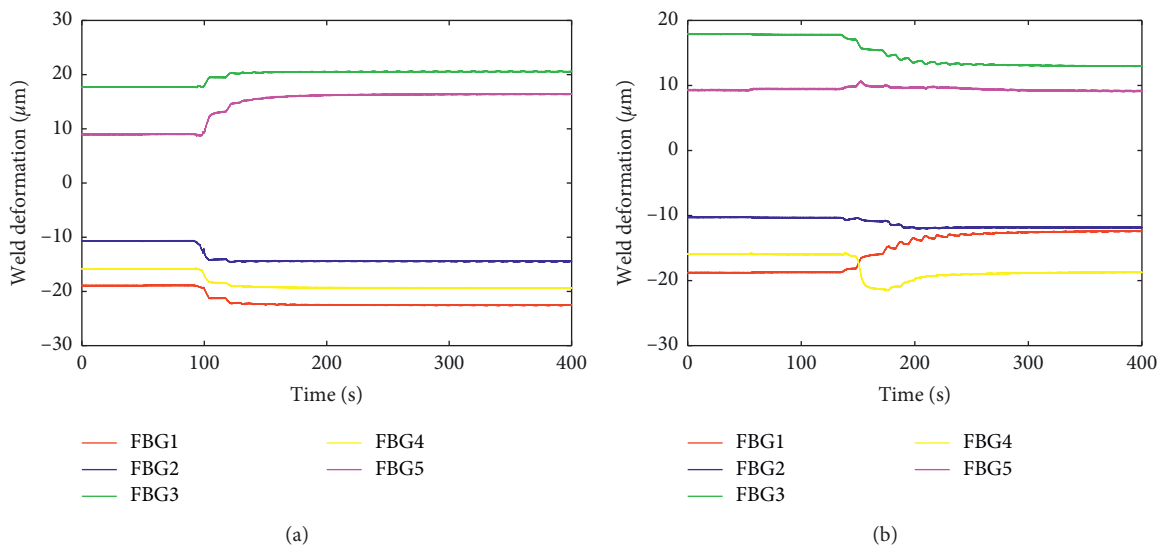


FIGURE 7: Welding deformation of eccentric loading of the top beam at a high position. (a) The block on the left side. (b) The block on the right side.

from different values, which is caused by the stress change during the hydraulic support being transported to the test bench; here, zero shift caused by temperature has been erased. Figure 7(a) illustrates five weld deformations of eccentric loading of the top beam at a high position when the block sets on the left side; it can be seen that FBG 3 and 5 increase at the positive phase; on the contrary, FBG 1, 2, and 4 decrease at the negative phase, which means welds 3 and 5 are stretched and welds 1, 2, and 4 are squeezed when the test bench provided hydraulic pressure. However, the condition is different in Figure 7(b); even though the initial welding deformation values of the five FBGs are the same as the ones shown in Figure 7(a), when the block sets on the right side, weld 1 is stretched, welds 1, 2, and 4 are all squeezed, and weld 5 approximately remains stable.

According to these two sets of experimental data, the force of the reverse four-bar linkage is even and symmetrical when the top beam is at a high position, and the stretch and squeeze amount of the weld is within $20 \mu\text{m}$. Therefore, the fiber grating sensor is effective for measuring the change of the reverse four-bar weld; furthermore, it can be used to evaluate the pros and cons of the reverse four-bar linkage structure design.

3.3. Welding Deformation of Eccentric Loading with the Top Beam at a Low Position. We repeat the same measurements after the top beam was dropped to a low position. The hydraulic pressure increases slowly to 23 MPa and then varies periodically between 23 MPa and 34 MPa as shown in

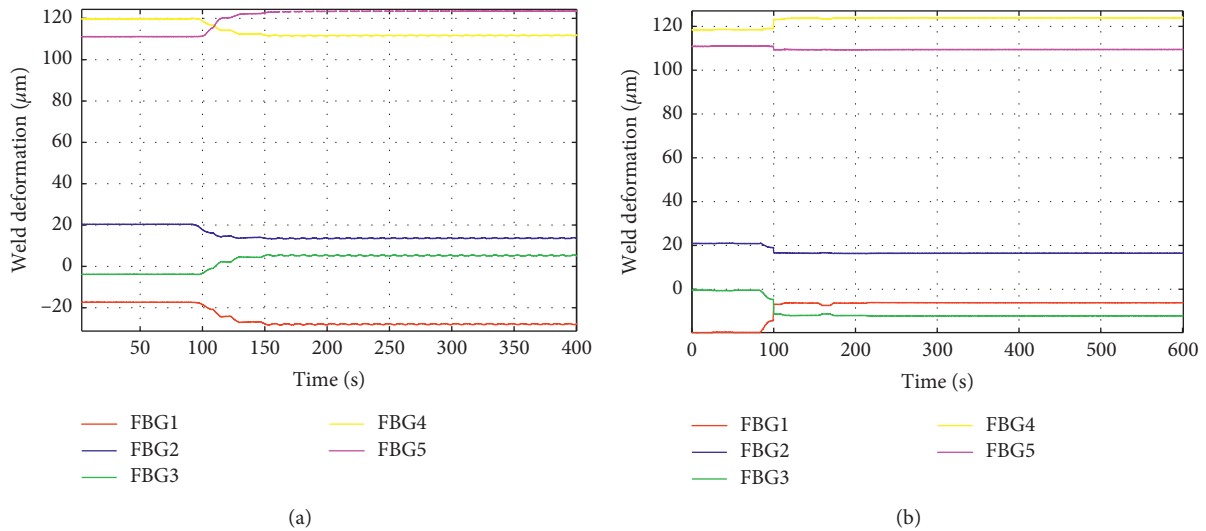


FIGURE 8: Welding deformation of eccentric loading of the top beam at a low position. (a) The block on the left side. (b) The block on the right side.

Figure 6(b). In Figure 8, the initial values of the five welding deformations are different from those in Figure 6, especially for FBG 4 and 5, whose welding deformations are stretched to $120 \mu\text{m}$ and $110 \mu\text{m}$, respectively. Compared with the weld change caused by the loading experiment, the one caused by the position of the top beam produces a greater weld deformation.

Figure 8(a) shows five welding deformations of eccentric loading of the top beam at a low position when the block sets on the left side. FBG 3 and 5 increase at the positive phase; on the contrary, FBG 1, 2, and 4 decrease at the negative phase, obeying the same principle revealed in Figure 7(a). However, in Figure 8(b), when the block sets on the right side, welds 1 and 4 are stretched and welds 2, 3, and 5 are all squeezed, which is different from that in Figure 7(b).

From the results, we can tell that, in the high and low loading test of the reverse four-bar linkage, the force law is not the same, especially when the block sets on the right side. We can also see some signs in the initial state of the low-position loading test that the weld deformation of FBG 4 and 5 is much larger than others, which means the hydraulic support is not in a stable state and could not be found by workers as usual. Thus, we can tell that FBG sensors can identify whether the hydraulic support is stable or not.

3.4. Cycle Loading Test with the Top Beam at a Low Position.

To view the welding deformation under cycle loading test with the top beam at a low position, we erased the initials of the five welding deformations. As the hydraulic pressure is a waveform with a period of 10 s, the weld deformations present the same characteristics, especially for FBG 1, 2, and 3 shown in Figure 9. In Figure 9(a), when the block sets on the left side, the maximum deformation of welds 1, 2, and 3 can reach $0.35 \mu\text{m}$, while the deformations of welds 4 and 5 are only $0.1 \mu\text{m}$. In Figure 9(b), when the block sets at the right side, the maximum deformation of welds 1, 2, and 3 can reach $0.35 \mu\text{m}$ and the deformation of weld 4 is $0.15 \mu\text{m}$; however, weld 5 does

not show periodicity. From the results in Figure 9, we find that the periodic loading pressure causes weak deformation of the welds, especially for weld 5.

3.5. 4000 s Long Cycle Loading Test. Furthermore, to explore the effect of long-term periodic loading on the weld, we monitored the above four sets of experiments for up to 4000 s. The pressure waveforms applied by the test bench are illustrated in Figure 6. Here, we also conduct four sets of trials: (1) right side eccentric loading of the top beam on the high position; (2) right side eccentric loading of the top beam on the low position; (3) left side eccentric loading of the top beam on the high position; (4) left side eccentric loading of the top beam on the low position.

The comparison of (1) and (2) experimental results is shown in Figure 10. We can tell that, in the high-position experiment of the right eccentric load within 4000 s, there is almost no cumulative deformation of the five welds over time. At the same time, in the low-position experiment of the right eccentric load, only the baseline of weld 2 has slowly shifted over time, and the other welds have not changed significantly.

Meanwhile, the comparison of (3) and (4) experimental results is shown in Figure 11. We can find that, in the high-position experiment of the left eccentric load, within 4000 s, welds 3 and 5 depict slight cumulative deformation over time; especially the baseline of weld 5 varies from $-0.1 \mu\text{m}$ to $+0.1 \mu\text{m}$. On the other side, in the low-position experiment of the left eccentric load, welds 1, 4, and 5 present significant cumulative deformation; the biggest shift of the baseline appears in weld 4, which varies from $-0.1 \mu\text{m}$ to $+0.3 \mu\text{m}$. Besides, in the dash line area, we find a jump appearing in five welds almost simultaneously. Since the weld maintains the original creep law after the jump, it is almost impossible for this jump to be caused by weak cracks in the weld. Here, we think that the reverse four-bar linkage structure has changed to another balanced force state, a more stable state under long-term load.

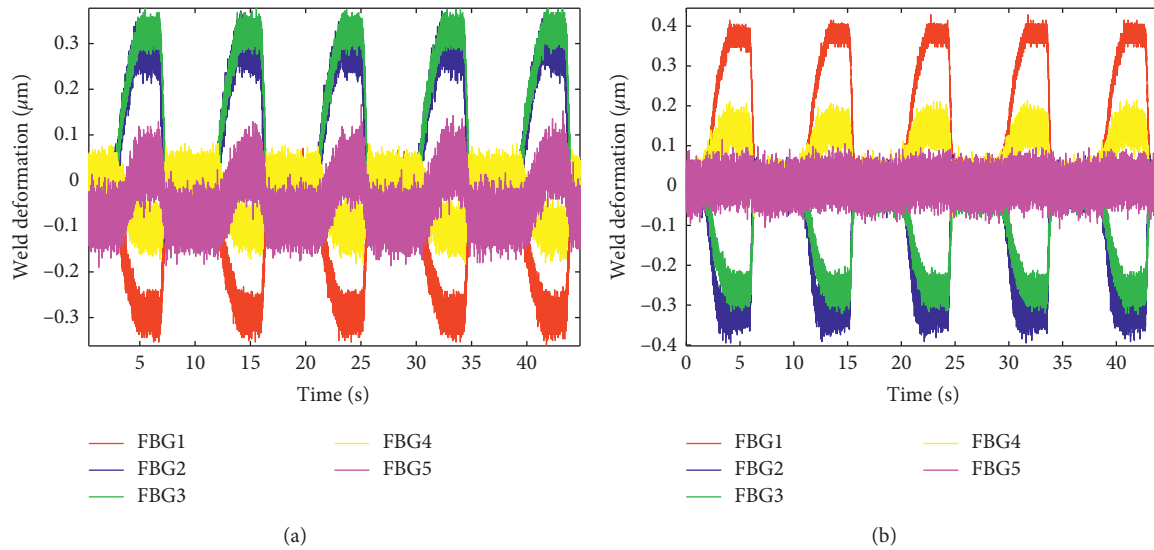


FIGURE 9: Cycle loading test with the top beam at a low position. (a) The block on the left side. (b) The block on the right side.

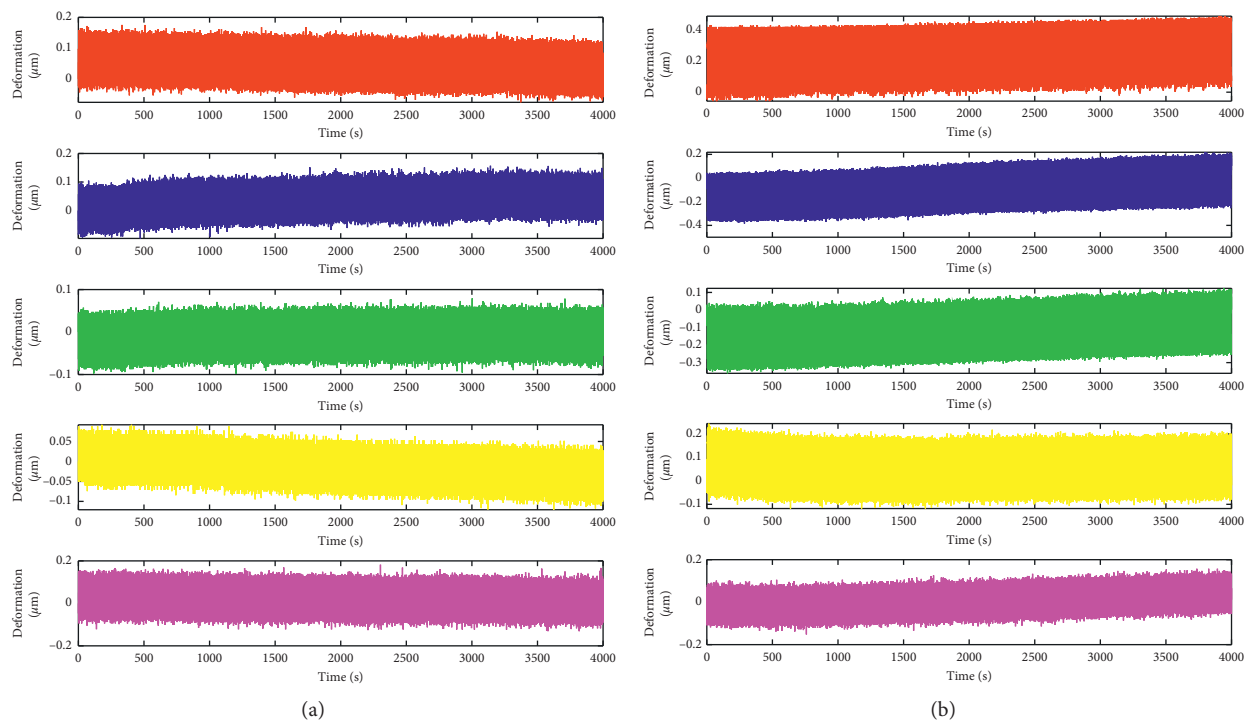


FIGURE 10: 4000 s cycle loading test with the block on the right side. (a) On the top position. (b) On the low position.

4. Discussion

As early as 1900, Barczak pointed out that the design of hydraulic supports should minimize stress concentration [28]. Although electrical strain gauges have long been used for monitoring structural changes, they sometimes lack the durability and integrity necessary to provide accurate, actionable information over extended periods. FBG-based optical fiber strain gauges offer a variety of advantages over electrical strain gauges.

In the National Coal Mine Support Equipment Quality Supervision and Inspection Center, the fiber grating sensing technology is used to realize the online monitoring of welds in the hydraulic support loading experiment. The results are reliable, proving that it is accurate enough to measure welding deformation by FBG sensors. Although the current hydraulic support test standards do not propose requirements for real-time monitoring of welds, whether the current Chinese test standard or the European test standard regards manual inspection of the degree of weld cracking as

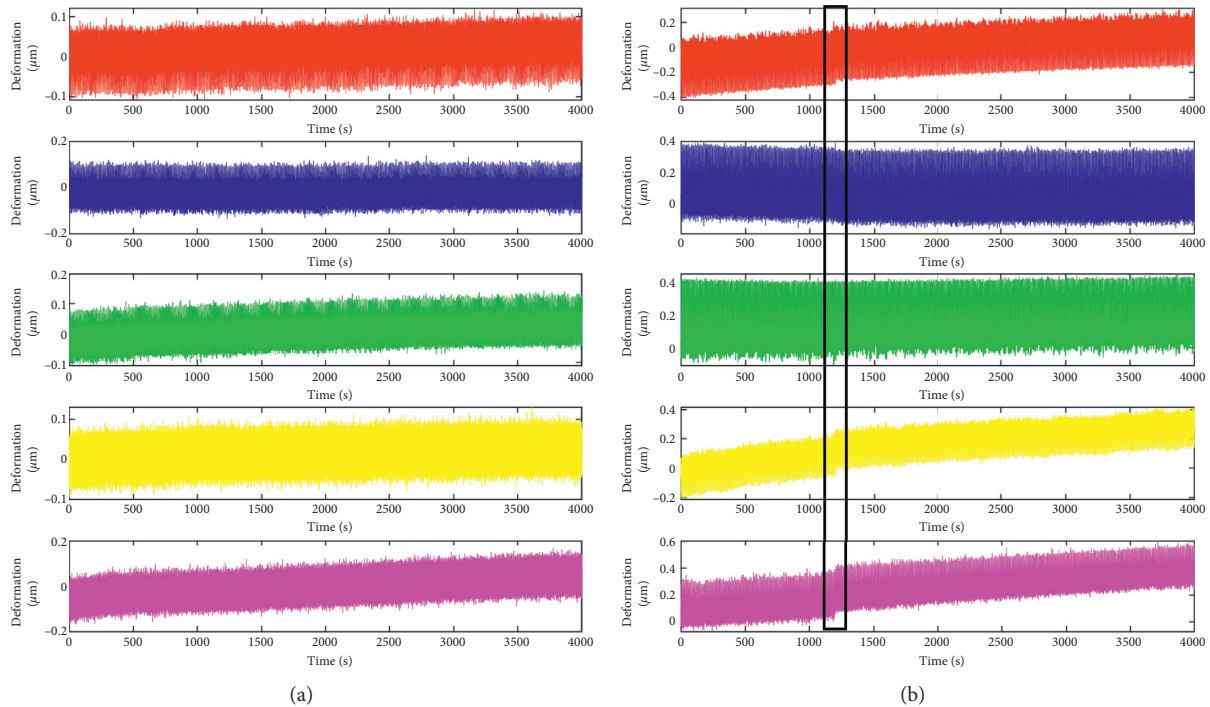


FIGURE 11: 4000 s cycle loading test with the block on the left side. (a) On the top position. (b) On the low position.

an indispensable item. Our research provides a feasible solution for real-time monitoring of hydraulic support welds, whether in the testing phase or the practical phase.

Due to the complex structure of the hydraulic support and the various types of welds, in the following research, the development of weld measuring sensors suitable for various planes and angles is an urgent problem to be solved.

In the cycle test, the welds present a baseline shift along with the cyclic load. It indicates the hydraulic support changes from one stable state to another stable state. This experimental result shows that welding seam monitoring can provide necessary feedback information for the cooperative support of hydraulic supports.

5. Conclusions

In this paper, a commercial FBG sensor is adopted to measure the welding deformations of a reverse four-bar hydraulic support. A synchronized measurement system is designed, which contains a hydraulic pressure measurement unit and an optical fiber data acquisition unit.

To reveal the welding deformation of the reverse four-bar linkage in the eccentric loading experiment, the strength test and the cycle life test of the top coal caving reverse four-link support with four typical eccentric load were conducted, respectively, in the National Coal Mine Support Equipment Quality Supervision and Inspection Center.

According to the results, we can conclude the following:

- (1) FBG sensor is accurate enough to measure welding deformation; measurement resolution reaches $0.1 \mu\text{m}$

- (2) In the high and low loading test of the reverse four-bar linkage, the force distribution is not the same; the welding deformation caused by the change of the top beam position is greater than the welding deformation caused by the loading test

- (4) Continuous long-term loading will cause the weld to show baseline shift or even jump to another stable state

Data Availability

Researchers can obtain the data from the corresponding author via dusy6509@163.com.

Disclosure

This paper is already published in the preprint given at <https://www.researchsquare.com/article/rs-607237/v1>.

Conflicts of Interest

The authors declare that they have no conflicts of interest.

Acknowledgments

The authors would like to thank Junhui Wang for his advice and help about the 3D model of hydraulic support. This research was funded by the National Natural Science Foundation of China (Grant nos. 5207415, 551804158, and 51974159), Tiandi Technology Co., Ltd., Technology Innovation Fund (Grant nos. KJ-2021-KCMS-05 and 2020-TD-ZD005), and Key R&D Program of Shandong Province (Grant no. 2019SDZY04).

References

- [1] J. Niu, "Study on automatic and intelligent following control system of hydraulic powered support in fully-mechanized coal mining face," *International Journal of Coal Science & Technology*, vol. 43, no. 12, pp. 85–91, 2015.
- [2] X. Fang, M. Liang, X. Xing, G. Xue, and M. Ma, "Development of hydraulic support pressure gauge based on FBG and its performance test," *Caikuang yu Anquan Gongcheng Xuebao/ Journal of Mining and Safety Engineering*, vol. 35, no. 5, pp. 945–952, 2018.
- [3] Z. Cheng, L.-H. Li, and Y.-N. Zhang, "Laboratory investigation of the mechanical properties of coal-rock combined body," *Bulletin of Engineering Geology and the Environment*, vol. 79, no. 4, pp. 1947–1958, 2020.
- [4] J. Wang, B. Yu, H. Kang et al., "Key technologies and equipment for a fully mechanized top-coal caving operation with a large mining height at ultra-thick coal seams," *International Journal of Coal Science & Technology*, vol. 2, no. 2, pp. 97–161, 2015.
- [5] J. Lou, F. Gao, J. Yang et al., "Characteristics of evolution of mining-induced stress field in the longwall panel: insights from physical modeling," *International Journal of Coal Science & Technology*, vol. 24, 2021.
- [6] X. Zhao, F. Li, Y. Liu, and Y. Fan, "Fatigue behavior of a box-type welded structure of hydraulic support used in coal mine," *Materials*, vol. 8, no. 10, pp. 6609–6622, 2015.
- [7] H. Junqing Liu and J. Liu, "The structure statics analysis and transient dynamics analysis of hydraulic support," in *Proceeding of the 2011 International Conference on Electric Information and Control Engineering*, pp. 895–898, Wuhan, China, April 2011.
- [8] C. Fu Fang, X. Meng, Q. Hu et al., "TANDEM and GMAW twin wire welding of Q690 steel used in hydraulic support," *Journal of Iron and Steel Research*, vol. 19, no. 5, pp. 79–85, 2012.
- [9] T. M. Barczak, "Examining longwall shield failures from an engineering design and operational perspective," in *Proceedings of the New Technology for Coal Mine Roof Support*, Pittsburgh, PA, USA, 2000.
- [10] D.-Z. Kong, Z.-B. Cheng, and S.-S. Zheng, "Study on the failure mechanism and stability control measures in a large-cutting-height coal mining face with a deep-buried seam," *Bulletin of Engineering Geology and the Environment*, vol. 78, no. 8, pp. 6143–6157, 2019.
- [11] G. F. Pereira, L. P. Mikkelsen, and M. McGugan, "Crack detection in fibre reinforced plastic structures using embedded fibre Bragg grating sensors: theory, model development and experimental validation," *PLoS One*, vol. 10, no. 10, pp. e0141495–38, 2015.
- [12] M. Liang, X. Fang, H. Bai, X. Xing, and G. Wu, "Application of temperature compensation fiber Bragg grating pressure sensor for bolting quality monitoring," *Meitan Xuebao/ Journal China Coal Soc.* vol. 42, no. 11, pp. 2826–2833, 2017.
- [13] S. Pamukcu, L. Cheng, and M. Pervizpour, "Introduction and overview of underground sensing for sustainable response," *Underground Sensing*, Academic Press, Cambridge, MA, USA, pp. 1–42, 2018.
- [14] Y. P. Wu, B. S. Hu, and P. S. Xie, "A new experimental system for quantifying the multidimensional loads on an on-site hydraulic support in steeply dipping seam mining," *Experimental Techniques*, vol. 43, no. 5, pp. 571–585, 2019.
- [15] M. Liang, X. Fang, S. Li, G. Wu, M. Ma, and Y. Zhang, "A fiber Bragg grating tilt sensor for posture monitoring of hydraulic supports in coal mine working face," *Measurement*, vol. 138, pp. 305–313, 2019.
- [16] Z. Ma and X. Chen, "Fiber Bragg gratings sensors for aircraft wing shape measurement: recent applications and technical analysis," *Sensors*, vol. 19, no. 1, p. 55, 2019.
- [17] J. G. Burnett, P. M. Blanchard, and A. H. Greenaway, "Optical fibre-based vectorial shape sensor," *Strain*, vol. 36, no. 3, pp. 127–133, 2000.
- [18] E. Ilbeygi, M. Jahanbakhshian, M. Arshadi Pirlar, and R. Karimzadeh, "Magnetic field sensor based on plasmonic fiber optics coupled with smartphone," *Optics & Laser Technology*, vol. 140, Article ID 107065, 2021.
- [19] R. Somma, C. Troise, L. Zeni et al., "Long-term monitoring with fiber optics distributed temperature sensing at campi flegrei: the campi flegrei deep drilling project," *Sensors*, vol. 19, no. 5, Article ID 1009, 2019.
- [20] M. Nishiyama and K. Watanabe, "Frequency characteristics of hetero-core fiber optics sensor for mechanical vibration," *Sensors and Actuators A: Physical*, vol. 209, pp. 154–160, 2014.
- [21] H. Yuting and H. Yuting, "Research progress of dynamic measurement technology based on Brillouin optical time-domain analysis," *Laser & Optoelectronics Progress*, vol. 55, no. 10, Article ID 100004, 2018.
- [22] V. G. M. Annamdas, "Review on developments in fiber optical sensors and applications," *International Journal of Materials Engineering*, vol. 1, no. 1, pp. 1–16, 2012.
- [23] S. Kang, G. Dong, J. Qiu, and Z. Yang, "(INVITED) Hybrid glass optical fibers-novel fiber materials for optoelectronic application," *Optical Materials X*, vol. 6, Article ID 100051, 2020.
- [24] E. K. Rotich Kipnoo, G. M. Isoe, D. K. Boiyo et al., "All optical polarization-based and DSP-Assisted distributed fiber sensor for earth mass movements caused by environmental factors," *Optik*, vol. 206, Article ID 163691, 2020.
- [25] N. Sabri, S. A. Aljunid, M. S. Salim, R. B. Ahmad, and R. Kamaruddin, "Toward optical sensors: review and applications," *Journal of Physics: Conference Series*, vol. 423, Article ID 012064, 2013.
- [26] K. O. Hill, Y. Fujii, D. C. Johnson, and B. S. Kawasaki, "Photosensitivity in optical fiber waveguides: application to reflection filter fabrication," *Applied Physics Letters*, vol. 32, no. 10, pp. 647–649, 1978.
- [27] C. Campanella, A. Cuccovillo, C. Campanella, A. Yurt, and V. Passaro, "Fibre Bragg grating based strain sensors: review of technology and applications," *Sensors*, vol. 18, no. 9, Article ID 3115, 2018.
- [28] T. M. Barczak, "Design considerations for the next generation of longwall shields," in *Proceedings of the Longwall USA Conference and Exhibit*, Pittsburgh, PA, USA, June 1900.

Research Article

Numerical Simulation of Surface Movement and Deformation Caused by Underground Mining with Complex Stratigraphic Boundary

Liang Wang,^{1,2} Chao He,² Songjun Cui,² and Feifei Wang³ 

¹Hebei Key Lab Smart Mat & Struct Mech, Shijiazhuang Tiedao University, Shijiazhuang 050043, China

²Wanbao Mining Co., Ltd., Beijing 100053, China

³Changsha Institute of Mining Research Co., Ltd., Changsha, Hunan 410012, China

Correspondence should be addressed to Feifei Wang; ffw1991@126.com

Received 23 March 2021; Revised 25 April 2021; Accepted 22 July 2021; Published 31 July 2021

Academic Editor: Dezhong Kong

Copyright © 2021 Liang Wang et al. This is an open access article distributed under the Creative Commons Attribution License, which permits unrestricted use, distribution, and reproduction in any medium, provided the original work is properly cited.

The interface program of finite element software based on surface spline interpolation is developed by using MATLAB software. The controllable 3D surface modeling based on CAD contour is realized. Taking a mine as an example, the method of establishing the 3D numerical calculation model including complex stratum boundary is studied. The influence of underground mining on surface movement and deformation under complex stratum conditions by using the FLAC3D software further was discussed. The research results show that the developed interface program of finite element software can well realize the numerical modeling of complex formation and provide help for subsequent numerical simulation. The calculated subsidence value is in good agreement with the measured value. The values of surface tilt, surface curvature, and surface horizontal deformation are less than the relevant regulations. The mining method of the filling method has no obvious effect on the surface structures. The research results can provide reference for similar numerical simulation.

1. Introduction

With the rapid development of economy, people's demand for mineral products is increasing, which makes the mining industry develop vigorously. The surface subsidence disaster brings hidden danger to people's safety [1–3]. The underground mining can cause deformation and damage to surrounding rock mass, surface structures, railways, and water bodies. Therefore, the surface movement and deformation caused by underground mining and the damage of surface buildings have become one of the global man-made environmental disasters and a hot issue in the mining field [4–6].

With the continuous improvement of mining related theory and technology, many achievements have been made in the study of surface subsidence caused by underground mining. At present, the prediction methods of surface movement and deformation can be divided into three categories. They are the theoretical analysis method, similarity

model, and numerical simulation method. In terms of the theoretical analysis method and the similar model method of surface movement and deformation caused by underground mining, Sasaoka et al. [7], Villegas et al. [8], Fazio et al. [9], Wu et al. [10], and He and Kang [11] have carried out a very meaningful discussion and practice on the theory of surface movement and deformation caused by underground mining. The theoretical analysis method can analyze and restore the surface movement and deformation curve by introducing related variables. However, the analysis of complex strata and terrain related problems is slightly insufficient. Nikolaos et al. [12], Guarino et al. [13], Scotto di Santolo [14], Yin et al. [15], and Li et al. [16] analyzed the surface movement caused by underground mining by simulation experiment method. However, the model experiment is established based on the similarity theory. Therefore, the material properties, stress factors, and boundary conditions are difficult to fully meet the similar requirements. Moreover, the model test process is complex.

At present, with the development of computer hardware and the progress of related numerical model software, the numerical simulation method of surface movement and deformation of underground mining has made rapid progress [17, 18]. The influence of dynamic load, groundwater, and other comprehensive factors on the surface movement and deformation can be considered in the numerical simulation [19]. Therefore, the numerical simulation has become a common analysis method [20–23]. Hadi et al. [24] used the FLAC3D software to simulate the ground surface subsidence due to sublevel caving method. Then, the longitudinal and transverse profiles of subsidence and the influence zone were studied. Zuo et al. [25] used a new program MDDA (mining discontinuous deformation analysis) which has been developed to simulate the continuous excavation process in mining engineering based on the existing discontinuous deformation analysis (DDA). Both the real-time stress distribution and evolution of rock strata movement during the mining process could be effectively obtained. Nick et al. [26] used a distinct element numerical model PFC2D to establish a large-scale avalanche of earth material. A general stretching and thinning of the avalanche are observed.

However, it is difficult to convert complex strata and complex terrain into the 3D numerical model. The establishment process of 3D stratigraphic boundary is complex. At present, the simplified stratigraphic boundary modeling is generally adopted by making a plane with consistent occurrence along a single direction, although some software can directly use the complex 3D stratum boundary to construct the model. However, it is very difficult to control the model element size at the 3D stratigraphic boundary, due to the complexity of CAD isoline spacing and nodes. The high-density grid is often generated in the area with large height difference (dense contour lines), which makes the total number of model units increase sharply. The existence of high-density mesh seriously affects the calculation speed of the 3D model.

Based on the self-developed CAD and finite element software interface program, this paper realizes the controllable grid of complex strata. Taking a mine as an example, a mine numerical model with complex geological strata is established by using the FLAC3D numerical simulation method. The relevant horizontal and vertical sections, geological boundary contour map, ore body distribution map, and other data are used in the model. Through the field engineering geological survey and rock mechanics, the mine numerical model is established. The actual rock mass mechanical parameters are obtained from the test. Then, the calculation and analysis are carried out. In this way, not only the influence of complex strata is

considered but also the influence of joint and other structural planes is reflected in the process of rock mass mechanical parameters. The surface subsidence is in good agreement with the measured values. The calculation results of surface movement and deformation can provide reliable guidance for mining.

2. Mesh Construction Method of 3D Complex Surface

The MATLAB program is used to realize the interface between CAD and finite element software. The 3D complex surface model can be directly generated from CAD data, which can be used by finite element software.

The features of the interface program are as follows:

- (1) The interface program can automatically extract the coordinates of isoline points and corresponding elevation values and coexist in the text file.
- (2) The interface program can automatically set the horizontal and vertical dimensions of the 3D surface mesh. The difference of the grid near the actual coordinate point can be found automatically. Finally, the regular and uniform 3D surface is obtained.
- (3) The interface program can realize the automatic extension of isoline to nonisoline data area. The automatic construction of area surface model without isoline data can be realized.

If the density of isoline points extracted by the program does not meet the needs of horizontal and vertical grid size of 3D surface, the surface spline interpolation method is used for encryption. The coordinates and corresponding elevation values of the points before encryption are

$$\begin{cases} X_i = [x_i \ y_i]^T, \\ H_i \quad i = 1, 2, 3, \dots, n, \end{cases} \quad (1)$$

where X_i and Y_i are the X and Y coordinates of elevation point I , respectively, and H_i is the elevation value of point i .

Formula (1) is a bivariate single-valued list function, which is fitted. The expression of bivariate spline function is as follows:

$$H(X) = c_1 + c_2x + c_3y + \sum_{i=1}^n c_{3+i}r^2 \ln(r_i^2 + \varepsilon), \quad (2)$$

where $r^2 = (x - x_i)^2 + (y - y_i)^2$, c_1, c_2, \dots, c_{3+n} is the coefficient to be solved, and ε is the adjustment coefficient, ranging from 0.01 to 1.00 for flat areas and 10^{-6} to 10^{-5} for singular surfaces. The coefficient to be calculated can be determined by the following formula:

$$\left\{ \begin{array}{l} \sum_{i=1}^n c_{3+i} = 0, \\ \sum_{i=1}^n c_{3+i} x_i = 0, \\ \sum_{i=1}^n c_{3+i} y_i = 0, \\ c_1 + c_2 x_j + c_3 y_j + \sum_{i=1}^n c_{3+i} r_{ji}^2 \ln(r_{ji}^2 + \varepsilon) + h_j c_{3+j} = H_j, \quad j = 1, 2, \dots, n; i \neq j, \end{array} \right. \quad (3)$$

where $r_{ji}^2 = (x_j - x_i)^2 + (y_j - y_i)^2$ and h_j is the weighting coefficient of the j node, which can be taken as 0. Equation (3) is expressed as matrix

$$A_{m \times m} C_{m \times 1} = H_{m \times 1}, \quad (4)$$

where $C_{m \times 1}$ is a symmetric matrix composed of node coordinate values and weighted coefficients. If $A_{m \times m}$ is not a singular matrix, then the equation can be solved and the coefficient matrix is

$$C_{m \times 1} = A_{m \times m}^{-1} H_{m \times 1}. \quad (5)$$

Then, equation (2) can determine that if the model area is divided into k quadrilateral grids, the corresponding isoline elevation of each grid node is expressed as

$$H_k = c_1 + c_2 x_k + c_3 y_k + \sum_{i=1}^n c_{3+i} r_{ki}^2 \ln(r_{ki}^2 + \varepsilon). \quad (6)$$

The partial derivative of elevation function of isoline at any grid node is expressed as

$$\left\{ \begin{array}{l} \frac{\partial H_k}{\partial x} = c_2 + 2 \sum_{i=1}^n c_{3+i} \left[\ln(r_{ki}^2 + \varepsilon) + \frac{r_{ki}^2}{r_{ki}^2 + \varepsilon} \right] + (x_k - x_i), \\ \frac{\partial H_k}{\partial y} = c_3 + 2 \sum_{i=1}^n c_{3+i} \left[\ln(r_{ki}^2 + \varepsilon) + \frac{r_{ki}^2}{r_{ki}^2 + \varepsilon} \right] + (y_k - y_i). \end{array} \right. \quad (7)$$

c_{3+i} is the coefficient to be solved. k is the number of quadrilateral meshes. i is the specific grid node. ε is the adjustment coefficient, ranging from 0.01 to 1.00 for flat areas and 10^{-6} to 10^{-5} for singular surfaces.

Through formula (7) and grid node coordinates, the corresponding coordinates of the mesh nodes of the fitting surface can be obtained. The three-dimensional coordinates of the interpolated points can be obtained.

Taking the CAD contour, as shown in Figure 1, as an example, the grid length in horizontal and vertical directions (25 m in horizontal direction and 20 m in vertical direction) is set independently in the interface program. The local part of CAD contour line (such as the lower left corner of CAD drawing) cannot meet the grid density. The program carries out automatic interpolation calculation to generate the 3D surface model. The different grayscale in Figure 2(a) represents different elevation. The model is consistent with the isoline in Figure 1.

3. Engineering Case Analysis

3.1. General Situation of Mining Area. The surface of the mining area is gentle, slightly inclined to the east, with a gradient of about 7‰. The surface of the mining area is approximately horizontal. The strata in the mining area are composed of quaternary loose rocks, neogene clastic rocks, metamorphic rocks of Daqeshan formation of Middle Proterozoic Zhujiashan group, and ultrabasic rocks. There are mainly two ore belts K1 and K2 in the mining area. The K1 ore belt occurs in the top alteration of the rock mass. The K2 mineralization belt occurs in the alteration of the rock bottom. The occurrence of K1 and K2 ore belts is consistent with the top and bottom of the rock mass, respectively.

A large number of buildings and structures are distributed on the surface of the mining area. The several villages and a provincial highway are mainly distributed within the scope of the mining right. If the surface is destructively deformed, it will have serious consequences. This paper will focus on the analysis of the surface movement and deformation of underground mining. The geological boundary of strata in the mining area is complex. The contour line of typical rock stratum boundary is shown in Figure 3. Because the theoretical analysis method has strict requirements on the occurrence of strata, it is very difficult to establish the complex geological boundary in the similar model test. Therefore, it is very practical to use numerical simulation analysis for the mine with complex stratum boundary.

3.2. Construction of Numerical Model. According to the actual situation of the mine, the developed interface program is used to realize the three-dimensional surface modeling of multiple complex strata, which provides the basis for the subsequent surface movement and deformation analysis. According to the geological exploration data, a three-dimensional grid of quaternary stratigraphic boundary and surface topography is established, as shown in Figure 4. According to the contour map of stratigraphic boundary, the boundary 3D grid of upper K1 ore body and lower K2 ore body is established, as shown in Figure 5. The final 3D grid of stratigraphic boundary is shown in Figure 6.

According to the established three-dimensional grid of stratum boundary, the numerical calculation model is completed and the units are divided. According to the

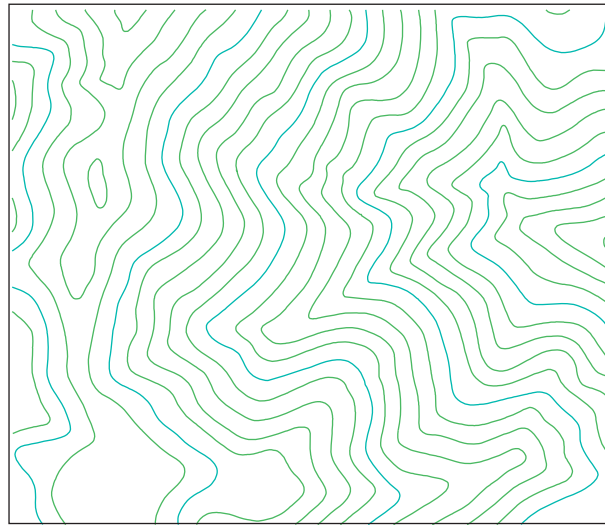
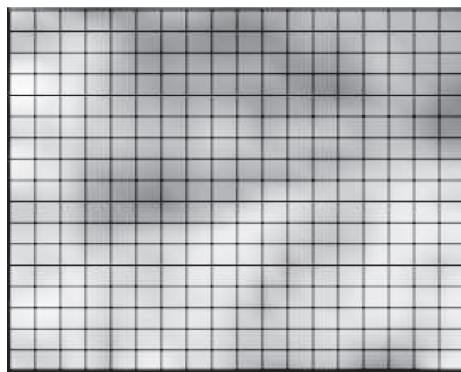
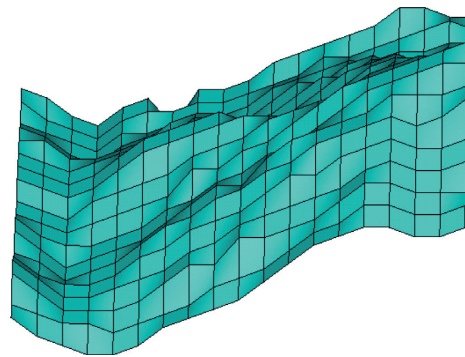


FIGURE 1: Original CAD contour map.



(a)



(b)

FIGURE 2: 3D surface model. (a) Top view grayscale image of 3D surface. (b) Three-dimensional surface stereogram.

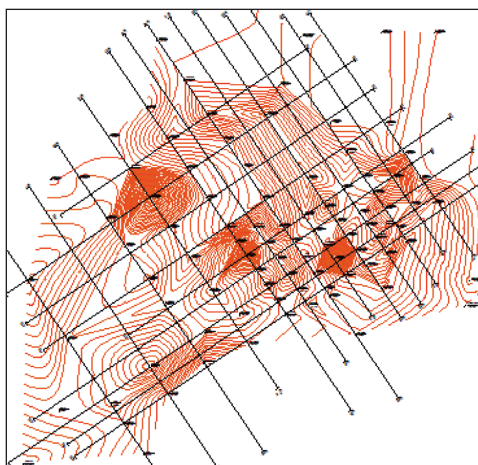


FIGURE 3: Contour line of ore body floor strata boundary.

horizontal projection of ore body, the high- and low-grade ore bodies are divided. The three-dimensional model of the ore body and surrounding rock three-dimensional model is shown in Figure 7. The different colors represent different



FIGURE 4: Quaternary stratigraphic boundary and surface grid map (front view).



FIGURE 5: Grid diagram of boundary line of K1 ore body and K2 ore body (front view).

grades of ore bodies. The two-layer ore bodies are composed of four three-dimensional curved surfaces. The internal units of the calculation model are shown in Figure 8. In Figure 8, group 9 is the quaternary system, group 11 is the Neogene rock mass, group 10 is the roof rock mass of K1 seam, group 7 is the roof rock mass of K1 seam and K2 seam, group 8 is the floor rock mass of K2 seam, and group 3, group 5, and group 6 are different grade ore bodies.

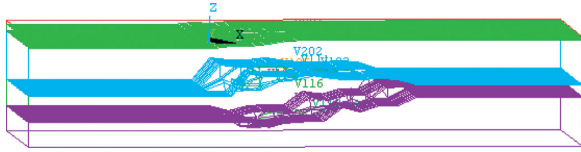


FIGURE 6: Grid diagram of stratigraphic boundary.

In the numerical analysis of underground engineering, the key to successful calculation is not only the accurate calculation model but also the initial geo-stress field [27, 28]. This time, the load is applied according to the self-weight stress of the rock mass. The z -direction constraint is applied at the bottom of the model, and the X -direction and Y -direction constraints are applied around the model. The surface is a free surface.

3.3. Numerical Simulation Scheme and Parameter Value. This numerical simulation mainly analyzes the influence law and scope of mining on the surface. According to the mine design, the simulated mining steps are determined. The filling is carried out at the end of each mining step. The specific numerical simulation scheme is shown in Figure 9.

According to the results of rock physical and mechanical test and rock mass quality evaluation, the mechanical parameters of surrounding rock mass are calculated according to Hoek–Brown criterion. The typical Hoek–Brown calculation curve is shown in Figure 10. The final mechanical parameters of rock mass are shown in Table 1.

3.4. Analysis of Numerical Simulation Results. After the high-grade ore above 280 m in K1 ore body is mined and filled, the displacement of the upper rock mass next to the filling body is the largest, which is 0.15 m. The surface displacement above the mining area is the largest, about 0.05 m. After the mining and filling of high-grade ore below –280 m of K1 ore body and –730 m~–590 m of K2 ore body, the maximum displacement of rock stratum appears above the filling body of K2 ore body, which is about 0.3 m. The surface displacement is about 0.1 m. After the high-grade ore above –730 m and below –590 m of K2 ore body is mined and filled, the maximum displacement of strata is located above the filling body of K2 ore body, and the increase is not obvious, which is 0.32 m. The surface displacement reaches 0.2 m. The mining of all low-grade ore bodies has a significant impact on strata movement. The maximum displacement inside the strata reaches 0.37 m, which is located in the upper part of K2 ore body and relatively close to the surface. At this time, the maximum displacement of the surface reaches 0.3 m. The cloud chart of strata movement in different mining stages is shown in Figure 11. The results of FLAC3D are imported into surfer software, and the final deformation of the surface is shown in Figure 12.

3.5. Analysis of Theoretical Calculation Results. At present, the mine has arranged the surface subsidence observation points along the 1-1 survey line. The mining of the lower ore

body of Miaozhuang has been completed, and the mining area is far away from here. The measured results show that the surface subsidence has become stable. The maximum measured value of subsidence near village 4 is 0.07 m, which can be regarded as the final subsidence value of this point. There is no obvious damage sign of surface structures.

FLAC3D can directly export the surface subsidence isoline map and the surface horizontal movement isoline map. Surface slope contour map and surface curvature contour map are transformed into surface horizontal deformation contour map. It can be realized by the derived surface subsidence and surface horizontal movement data by the MATLAB, according to the following calculation formula.

The formula for calculating the inclination of the earth's surface in x and y directions is

$$i_x(x, y) = \frac{\partial W(x, y)}{\partial x},$$

$$i_y(x, y) = \frac{\partial W(x, y)}{\partial y},$$
(8)

where $W(x, y)$ is the surface subsidence value.

The formula for calculating the curvature of the earth's surface in x and y directions is

$$K_x(x, y) = \frac{\partial^2 W(x, y)}{\partial x^2} = \frac{\partial i_x W(x, y)}{\partial x},$$

$$K_y(x, y) = \frac{\partial^2 W(x, y)}{\partial y^2} = \frac{\partial i_y W(x, y)}{\partial y},$$
(9)

where $i(x, y)$ is the surface inclination value in the x and y directions.

The formula for horizontal deformation in the direction of x and y of the surface is

$$\varepsilon_x(x, y) = \frac{\partial U_x(x, y)}{\partial x},$$

$$\varepsilon_y(x, y) = \frac{\partial U_y(x, y)}{\partial y},$$
(10)

where $U(x, y)$ is the horizontal surface movement in x and y directions.

The surface subsidence isoline map, surface horizontal movement contour map, and corresponding survey line profile map obtained by numerical simulation are shown in Figures 13 and 14. The surface slope contour map, surface curvature contour map, surface horizontal deformation contour map, and corresponding survey line profile map obtained by formulas (8)–(10) are shown in Figures 15–17. The final surface movement deformation value obtained is shown in Table 2.

The damage degree of buildings affected by mining depends on the size of surface deformation and the ability of buildings to resist deformation. As there is no specification for this aspect in noncoal mines, the influence range of surface deformation of underground mining is delineated according to horizontal deformation $\varepsilon > 2.0$ mm/m or curvature $k > 0.2 \times 10^{-3}$ or inclination $i > 3.0$ mm/m with

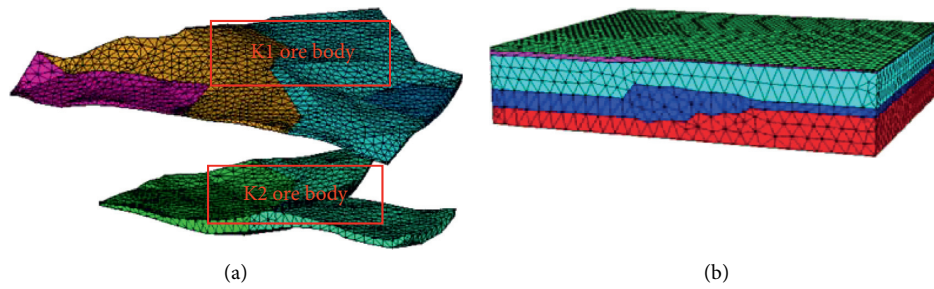


FIGURE 7: Three-dimensional model of the ore body and the surrounding rock three-dimensional model. (a) Ore body of K1 and K2. (b) Three-dimensional model.

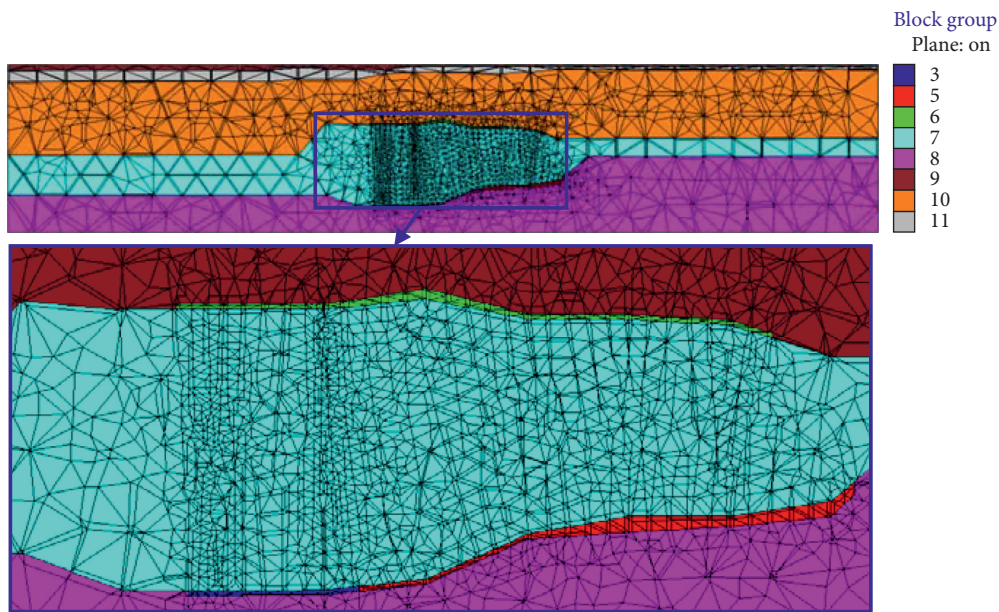


FIGURE 8: Unit diagram of the calculation model (note: group 9 is quaternary; group 11 is Neogene; group 10 is K1 roof rock; group 7 is K1 floor rock and K2 roof rock; group 8 is K2 floor rock; group 3, group 5, and group 6 are ore bodies.).

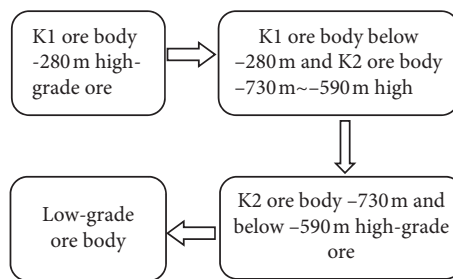


FIGURE 9: Numerical simulation calculation scheme.

reference to the regulations for retaining coal pillars in buildings, water bodies, railways, and main shafts [29].

According to the calculation, the underground mining has little influence on the surface of the mine. The calculated subsidence value at village 4 is 0.075 m, which is close to the measured value of 0.07 m. The numerical simulation results are consistent with the actual situation. The regional subsidence and horizontal movement of the ground surface will not affect the surface buildings and structures. Therefore, in the three regulations and other specifications, only three

surface deformation indexes, such as horizontal deformation, curvature, and inclination, are used to reflect the influence degree of surface buildings and structures. Horizontal surface deformation can cause tension cracks in buildings, surface curvature will cause uneven deformation of buildings and structures, and surface tilt may cause construction buildings overturn, which affects the safety of surface buildings and structures. According to the calculation results, the maximum inclination, maximum curvature, and horizontal deformation of the mine are $-0.5\sim 0.3$ mm/m,

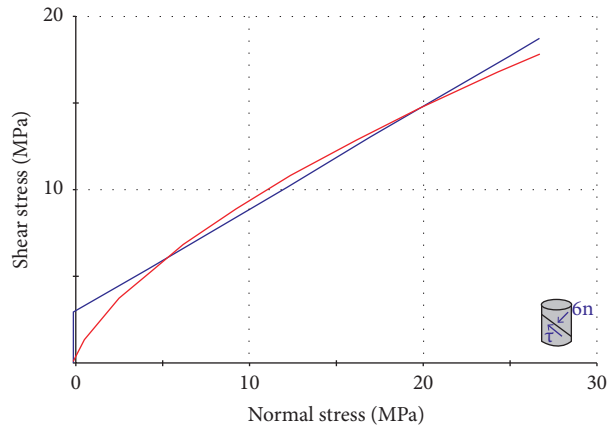
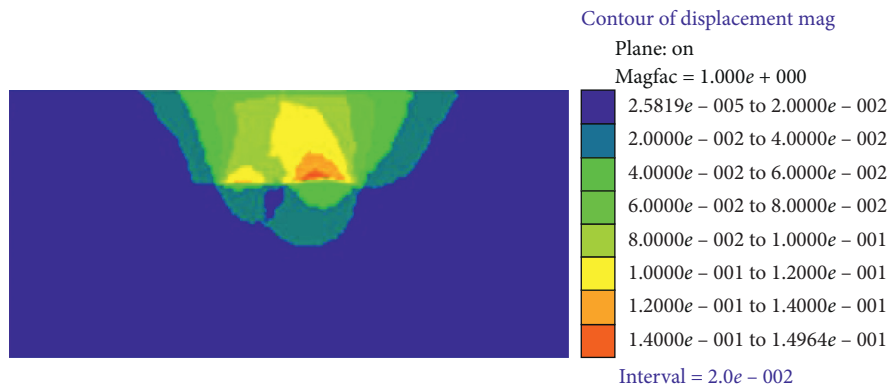


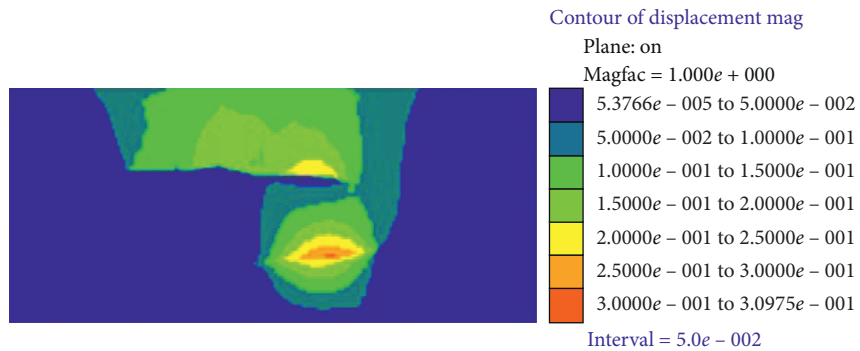
FIGURE 10: Calculation curve of Hoek–Brown criterion for roof rock mass of K1 ore body.

TABLE 1: Summary of rock mass mechanical parameters.

Rock stratum	Bulk density (kN/m ³)	Cohesion (MPa)	Internal friction angle (°)	Elastic modulus (GPa)	Poisson's ratio
Quaternary soil	1.9	0.56	29.3	0.021	0.32
Neogene rock mass	2.7	0.60	33.0	6.0	0.21
K1 ore body roof	2.7	3.28	32.8	12.0	0.26
K1 ore body floor	2.8	6.73	41.5	16.8	0.26
Floor of K2 ore body	2.7	6.95	41.5	15.3	0.26
Ore body	2.9	9.28	44.2	26.6	0.26
Filling body	2.0	0.50	32.0	0.60	0.25



(a)



(b)

FIGURE 11: Continued.

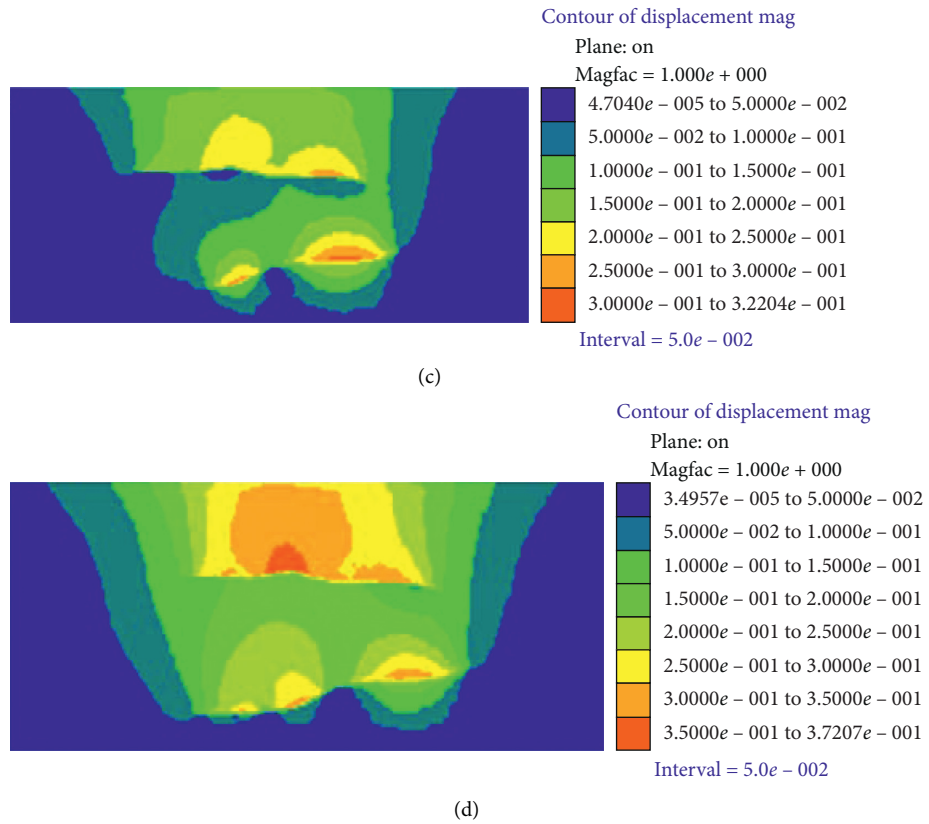


FIGURE 11: Cloud chart of strata movement in different mining stages. (a) Step 1. (b) Step 2. (c) Step 3. (d) Step 4.

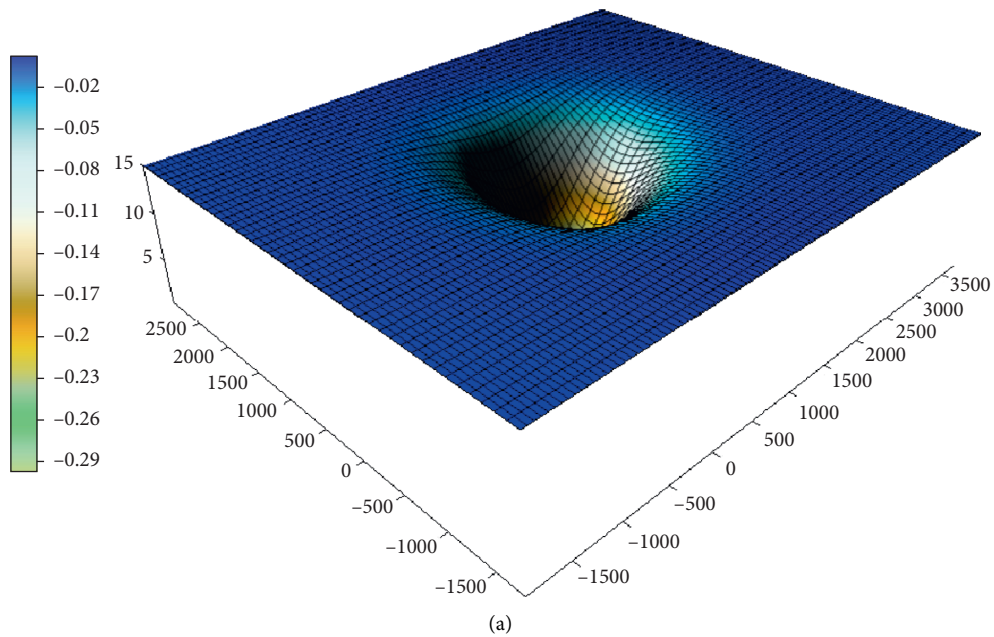
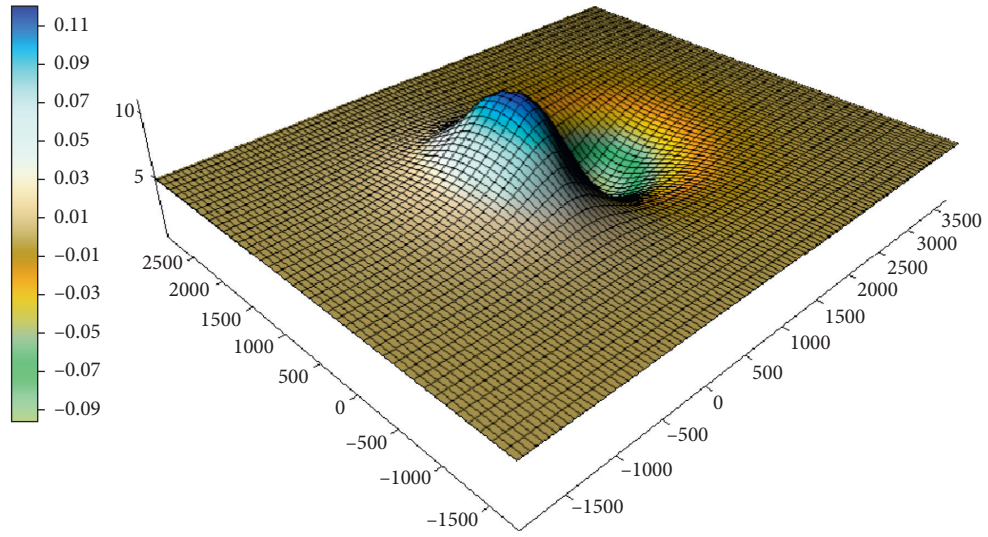
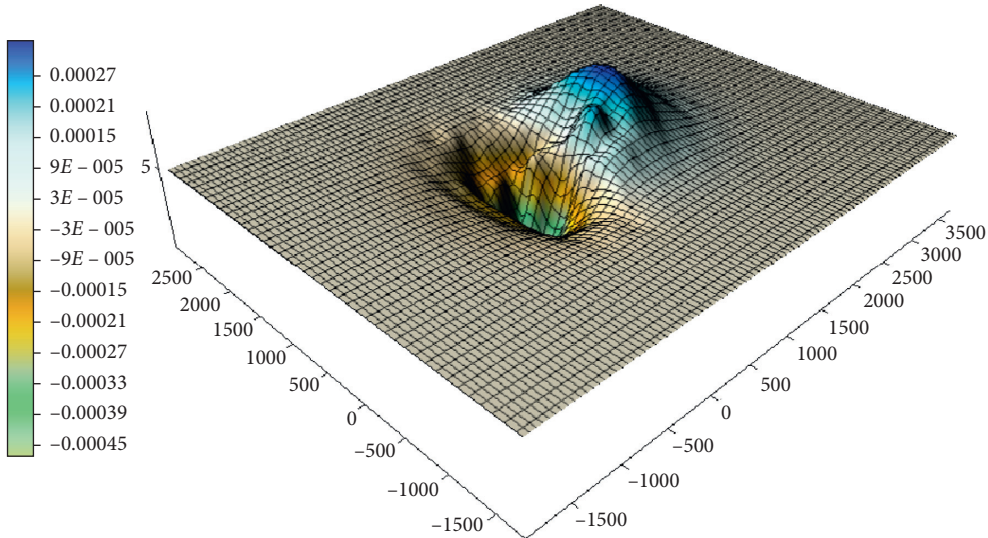


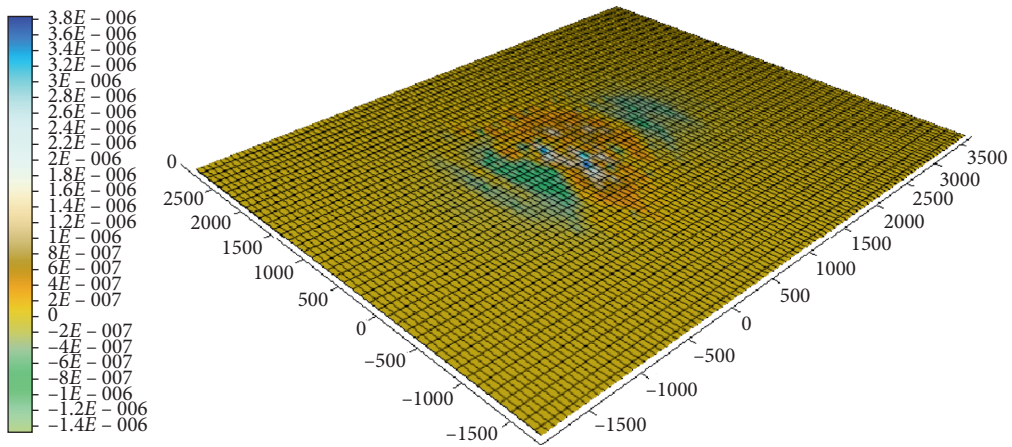
FIGURE 12: Continued.



(b)



(c)



(d)

FIGURE 12: Continued.

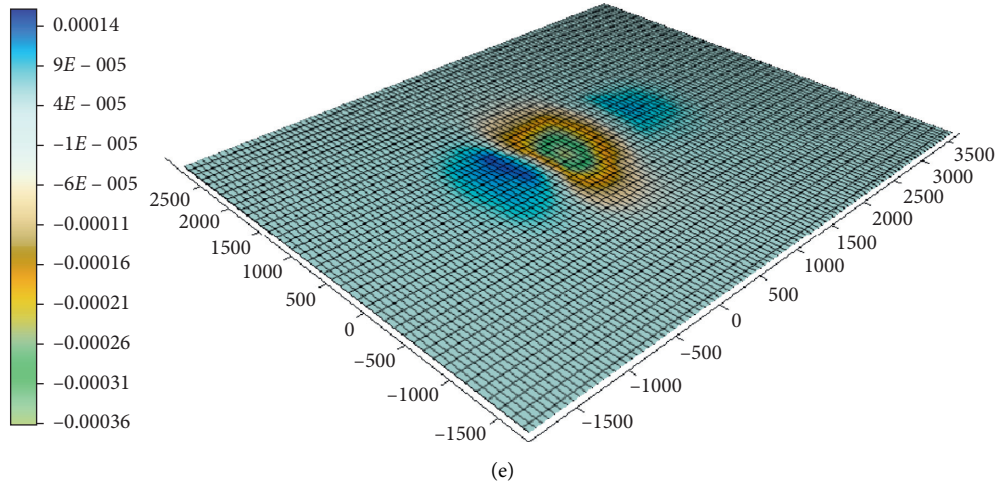


FIGURE 12: Final surface movement and deformation. (a) Cloud chart of surface subsidence. (b) Cloud image of surface horizontal movement. (c) Cloud chart of surface tilt. (d) Surface curvature nephogram. (e) Cloud image of surface horizontal deformation.

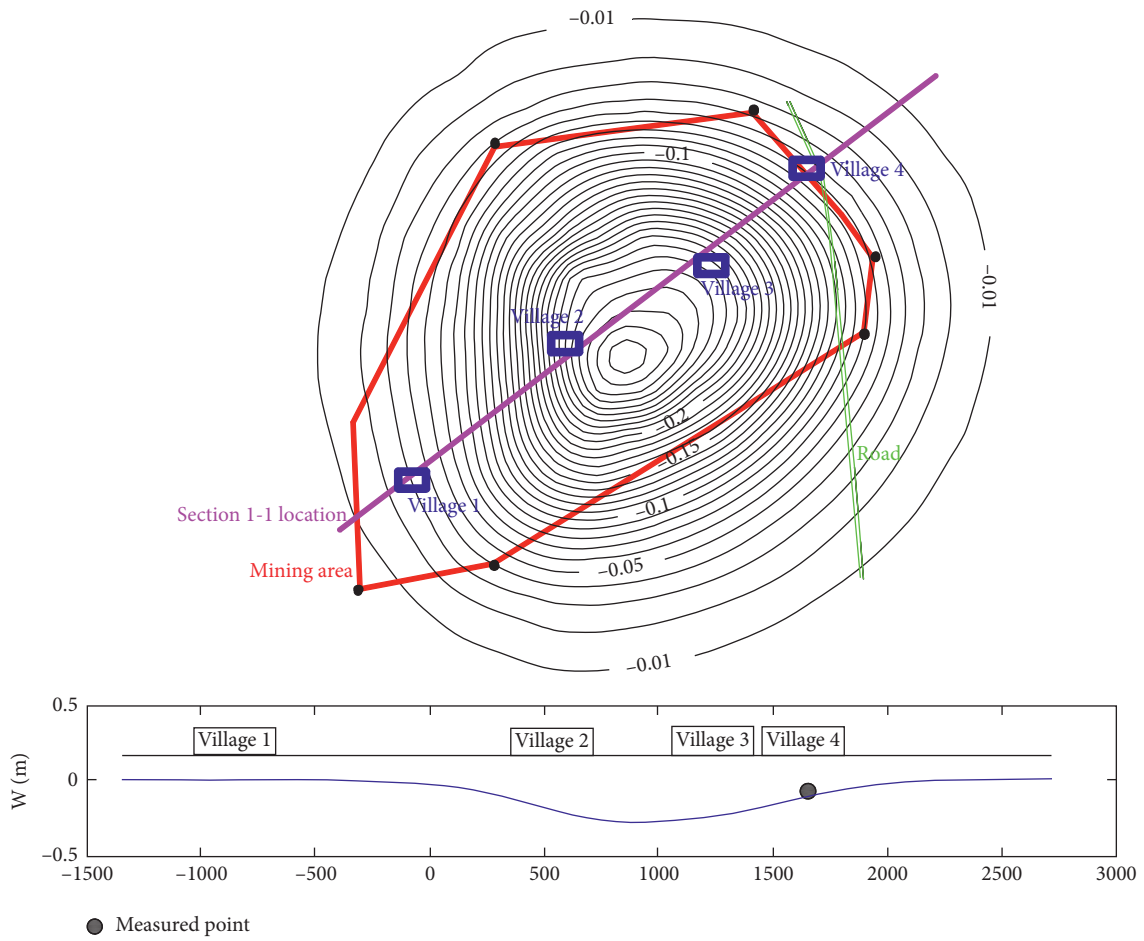


FIGURE 13: Surface subsidence contour map.

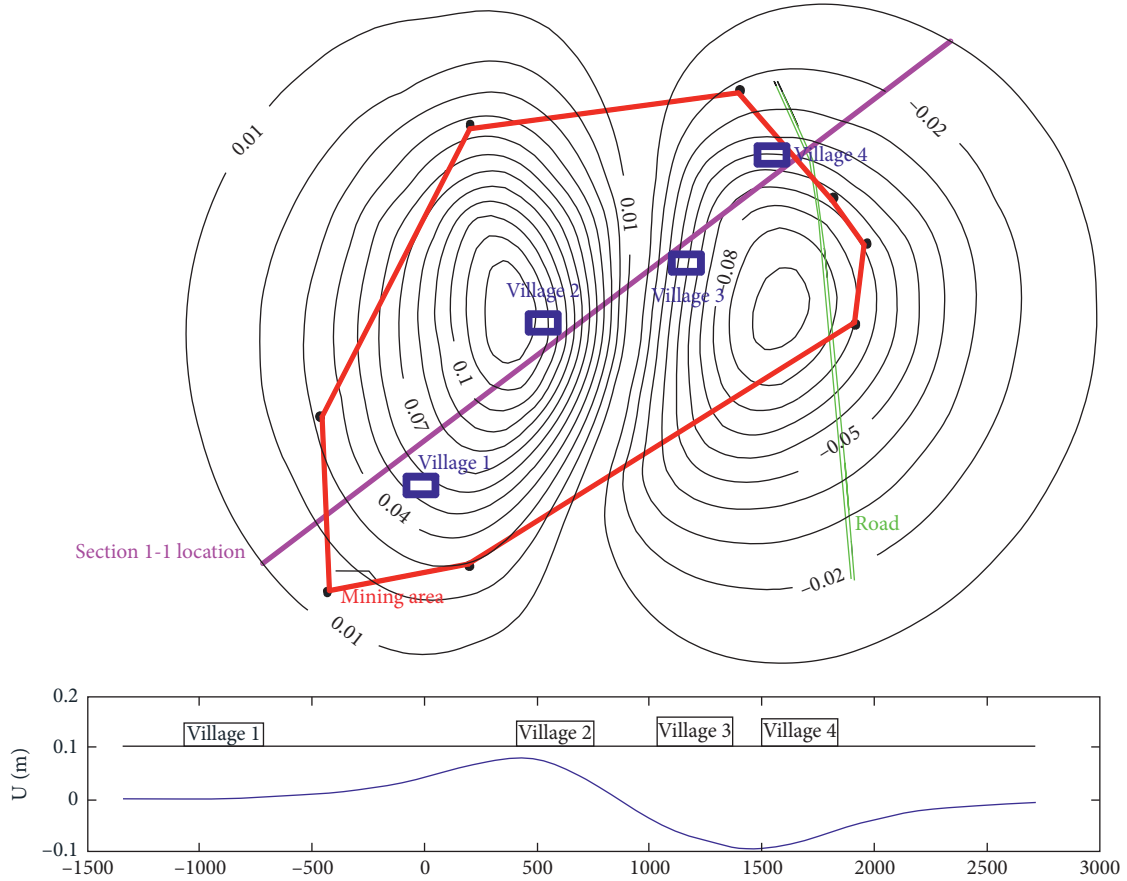


FIGURE 14: Contour map of horizontal movement.

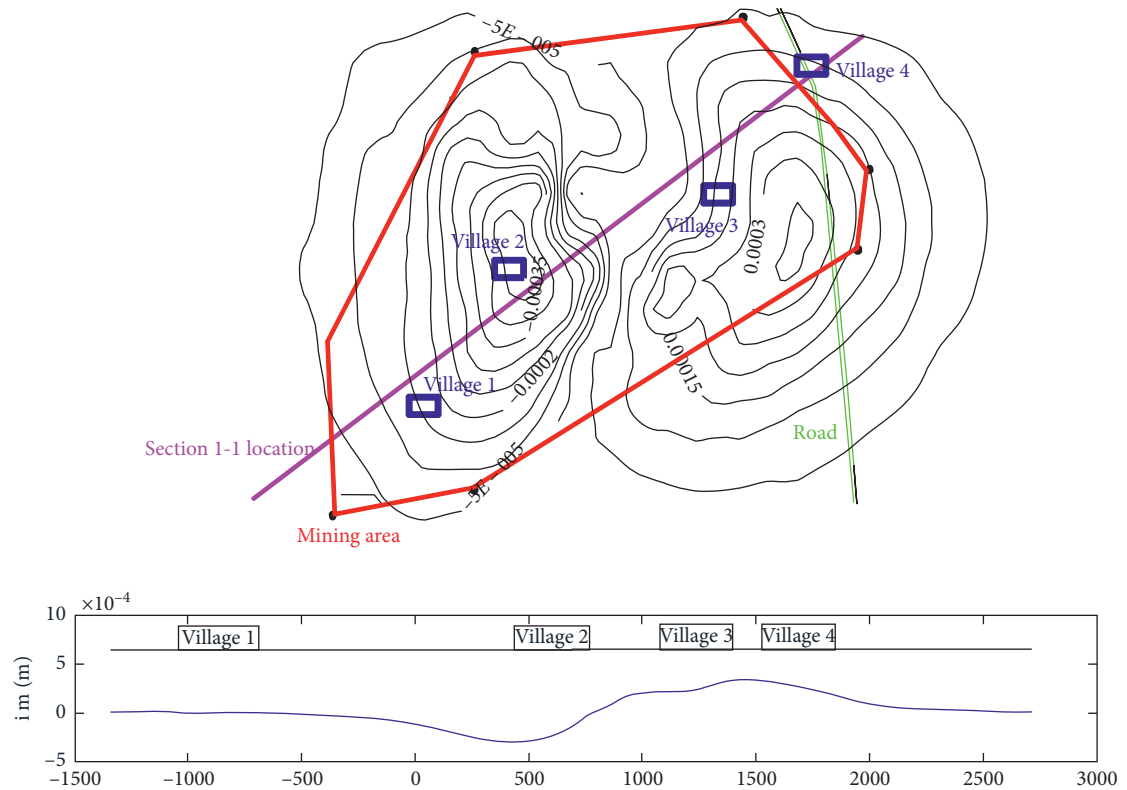


FIGURE 15: Contour map of surface tilt.

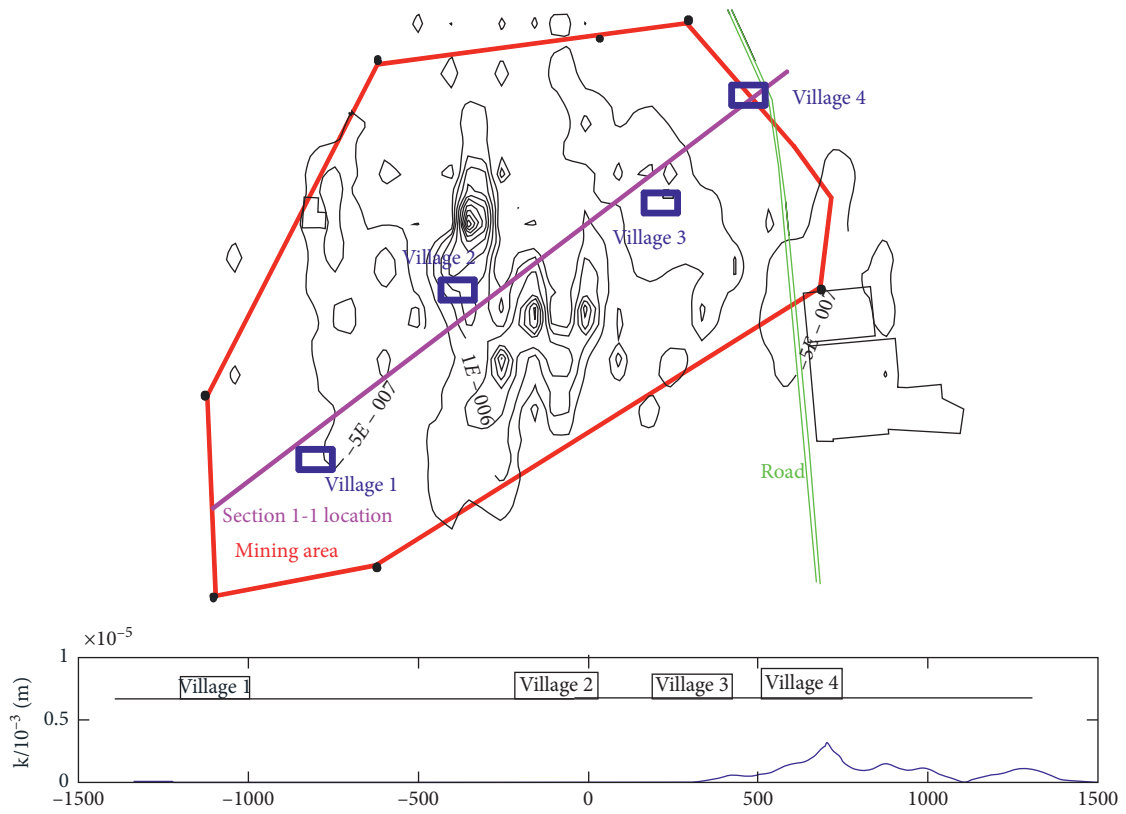


FIGURE 16: Contour map of surface curvature.

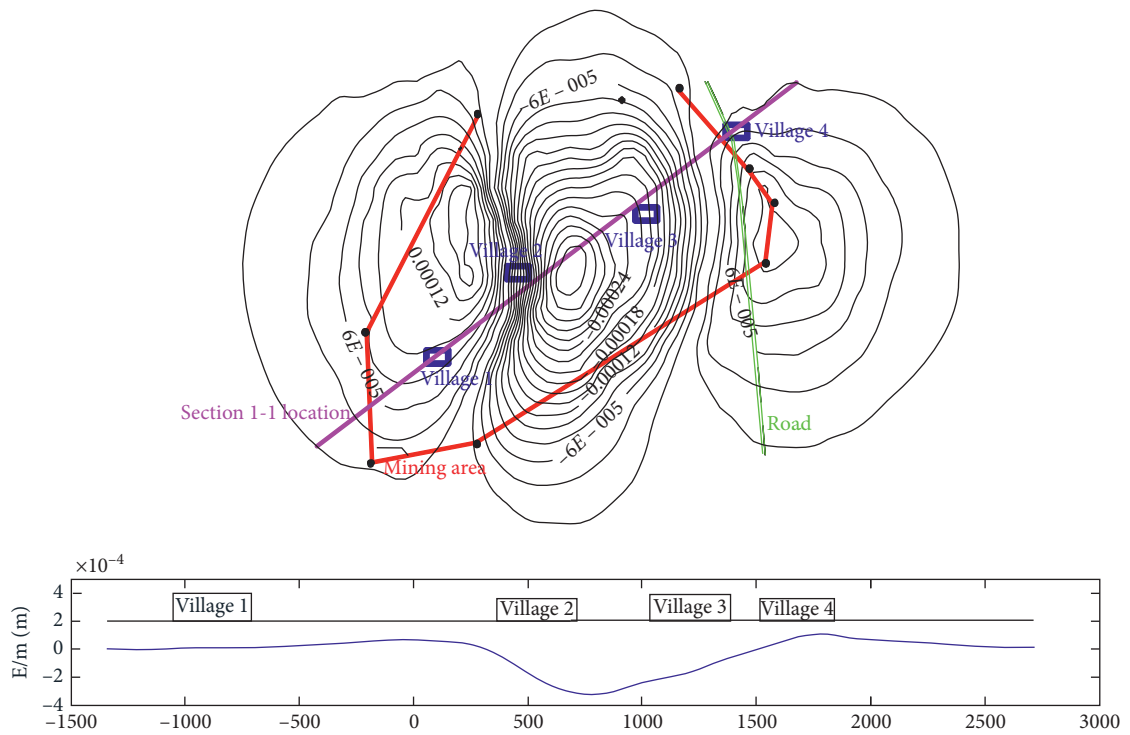


FIGURE 17: Contour map of surface horizontal deformation.

TABLE 2: Surface movement and deformation values.

Maximum subsidence (m)	Horizontal movement (m)	Tilt (mm/m)	Curvature ($10^{-6}/m$)	Horizontal deformation (mm/m)
0.350	-0.10~0.12	-0.5~0.3	-1.6~4.0	-0.38~0.18

$-1.6\sim 4.0 \times 10^{-6}/m$, and $-0.38\sim 0.18$ mm/m, which are not within the scope of influence specified in the three regulations. The mining method of the filling method has no obvious impact on the surface structures.

4. Conclusion

In this paper, the interface program between CAD and finite element software based on surface spline interpolation developed by MATLAB software is used to realize the controllable mesh of complex stratum. Based on a mine engineering example, the mine numerical model including multiple complex stratum boundaries is established. The surface movement and deformation of underground mining are analyzed emphatically.

- (1) Based on the self-developed interface program of CAD and finite element software, it can realize the controllable gridding of complex strata and provide a good foundation for the establishment of numerical calculation model.
- (2) According to the results of numerical simulation, the surface subsidence caused by underground mining is in good agreement with the measured value. The horizontal deformation, curvature, and inclination of the ground surface do not reach the critical value. The mining method of the filling method has no obvious effect on the surface structures. The filling mining can effectively control surface subsidence. Mining steps have an impact on surface subsidence. The results of the previous mining are affected by the next mining.
- (3) The developed interface program overcomes the difficulty of 3D complex formation boundary modeling. The program has the advantages of controllable unit size and node number. The program can realize area interpolation and automatic expansion of data without contour. The program effectively avoids the appearance of local high-density grid on the stratum boundary. The program improves the calculation speed of the model. The research results can provide reference for similar numerical simulation.

Data Availability

The data used to support the findings of this study are available from the corresponding author upon request.

Conflicts of Interest

The authors declare that there are no conflicts of interest regarding the publication of this paper.

Acknowledgments

The authors would like to thank Shijiazhuang Tiedao University for the support for the project research funding.

References

- [1] C. H. Tseng, Y. C. Chan, C. J. Jeng, R. J. Rau, and Y. C. Hsieh, "Deformation of landslide revealed by long-term surficial monitoring: a case study of slow movement of a dip slope in northern Taiwan," *Engineering Geology*, vol. 284, Article ID 106020, 2021.
- [2] K. J. Reinders, R. F. Hanssen, F. J. Leijen, and M. Korff, "Augmented satellite InSAR for assessing short-term and long-term surface deformation due to shield tunnelling," *Tunnelling and Underground Space Technology*, vol. 110, Article ID 103745, 2021.
- [3] H. D. Fan, L. Wang, B. F. Wen, and S. Du, "A new model for three-dimensional deformation extraction with single-track InSAR based on mining subsidence characteristics," *International Journal of Applied Earth Observation and Geoinformation*, vol. 94, Article ID 102223, 2021.
- [4] J. W. Hong, *Study on Dynamic Failure Law and Mining Subsidence Prediction System of Mining Overburden*, China University of Mining and Technology, Beijing, China, 1999.
- [5] N. Z. Xu and C. Gao, "Study on the special rules of surface subsidence affected by normal faults," *Journal of Mining and Strata Control Engineering*, vol. 2, no. 1, pp. 97–102, 2020.
- [6] D. F. Yang, Y. G. Zhang, S. Wang et al., "Analysis of the influence of hidden fault dip angle on ground pressure behavior in shallow seam roof," *Journal of Mining and Strata Control Engineering*, vol. 2, no. 4, pp. 68–78, 2020.
- [7] T. Sasaoka, H. Takamoto, H. Shimada, J. Oya, A. Hamanaka, and K. Matsui, "Surface subsidence due to underground mining operation under weak geological condition in Indonesia," *Journal of Rock Mechanics and Geotechnical Engineering*, vol. 7, no. 3, pp. 337–344, 2015.
- [8] T. Villegas, E. Nordlund, and C. D. Lindqvist, "Hangingwall surface subsidence at the Kiirunavaara mine, Sweden," *Engineering Geology*, vol. 121, no. 12, pp. 18–27, 2011.
- [9] N. L. Fazio, M. Perrotti, P. Lollino et al., "A three-dimensional back-analysis of the collapse of an underground cavity in soft rocks," *Engineering Geology*, vol. 228, no. 13, pp. 301–311, 2017.
- [10] K. Wu, M. Zhou, and Z. Q. Hu, "The prediction of ground fissure depth and width by mining," *Journal of Fuxin Mining Institute*, vol. 6, no. 6, pp. 549–552, 1997.
- [11] W. L. He and J. R. Kang, "Laws of ground movement and deformation in mountainous areas," *Journal of China Coal Society*, vol. 17, no. 4, pp. 1–15, 1992.
- [12] L. Nikolaos, P. R. Marpu, K. Pavlopoulos, and T. Ouarda, "Ground subsidence monitoring with SAR interferometry technique in the rural of Al Wagan UAE," *Remote Sensing of Environment*, vol. 216, no. 1, pp. 276–288, 2018.
- [13] P. Guarino, A. Santo, G. Forte, and M. Falco, "Analysis of a database for anthropogenic sinkhole triggering and zonation in the Naples hinterland (Southern Italy)," *Natural Hazards*, vol. 91, no. 30, pp. 1–20, 2018.

- [14] A. Scotto di Santolo, G. Forte, and A. Santo, "Analysis of sinkhole triggering mechanisms in the hinterland of Naples (Southern Italy)," *Engineering Geology*, vol. 237, pp. 42–52, 2018.
- [15] G. Z. Yin, X. F. Xian, and G. F. Dai, "Basic behaviour of strata movement in seam with deep dip angle," *Chinese Journal of Geotechnical Engineering*, vol. 23, no. 4, pp. 450–453, 2001.
- [16] X. Y. Li, J. P. Li, C. B. Zhou, and W. Xiang, "Comparative study on numerical simulation and similarity simulation of overburden deformation in abandoned stope," *Rock and Soil Mechanics*, vol. 26, no. 12, pp. 1907–1912, 2005.
- [17] F. Wang, Q. Ren, B. Chen et al., "Strata movement law based on progressive caving of the hanging wall: a case of study in Chaganaobao Iron-Zinc Mine," *Arabian Journal of Geosciences*, vol. 13, no. 21, pp. 1155–1170, 2020.
- [18] M. Sepehri, D. B. Apel, and R. A. Hall, "Prediction of mining-induced surface subsidence and ground movements at a Canadian diamond mine using an elastoplastic finite element model," *International Journal of Rock Mechanics and Mining Sciences*, vol. 100, pp. 73–82, 2017.
- [19] K. Xia, C. Chen, K. Yang, H. Zhang, and H. Pang, "A case study on the characteristics of footwall ground deformation and movement and their mechanisms," *Natural Hazards*, vol. 104, no. 1, pp. 1039–1077, 2020.
- [20] C. M. Subhash, S. Debsarma, and S. Sen, "A mathematical model for analyzing the ground deformation due to a creeping movement across a strike slip fault," *GEM—International Journal on Geomathematics*, vol. 10, no. 16, 2019.
- [21] X. Zhao and Q. Zhu, "Analysis of the surface subsidence induced by sublevel caving based on GPS monitoring and numerical simulation," *Natural Hazards*, vol. 103, no. 3, pp. 3063–3083, 2020.
- [22] D. Z. Kong, S. J. Pu, Z. H. Cheng, and G. Wu, "Coordinated deformation mechanism of the top coal and filling body of gob-side entry retaining in a fully mechanized caving face," *International Journal of Geomechanics*, vol. 21, no. 4, 2021.
- [23] D.-Z. Kong, Z.-B. Cheng, and S.-S. Zheng, "Study on the failure mechanism and stability control measures in a large-cutting-height coal mining face with a deep-buried seam," *Bulletin of Engineering Geology and the Environment*, vol. 78, no. 8, pp. 6143–6157, 2019.
- [24] P. Hadi, A. Y. Bafghi, and M. Najafi, "Impact of ground surface subsidence due to underground mining on surface infrastructure: the case of the anomaly No. 12 Sechahun, Iran," *Environmental Earth Sciences*, vol. 78, no. 14, p. 409, 2019.
- [25] J.-P. Zuo, Y.-J. Sun, Y.-C. Li, J.-T. Wang, X. Wei, and L. Fan, "Rock strata movement and subsidence based on MDDA, an improved discontinuous deformation analysis method in mining engineering," *Arabian Journal of Geosciences*, vol. 10, no. 18, p. 395, 2017.
- [26] T. Nick, R. M. Bennett, and N. Petford, "Analyses on granular mass movement mechanics and deformation with distinct element numerical modeling: implications for large-scale rock and debris avalanches," *Acta Geotechnica*, vol. 4, pp. 233–247, 2009.
- [27] X. L. Jiang, F. F. Wang, H. Yang, and P. Lian, "Dynamic response of shallow-buried tunnels under asymmetrical pressure distributions," *Journal of Testing and Evaluation*, vol. 46, no. 4, pp. 1574–1590, 2018.
- [28] F. F. Wang, X. L. Jiang, J. Y. Niu, and H. Yang, "Experimental study on seismic dynamic characteristics of shallow bias tunnel with a small space," *Shock and Vibration*, vol. 2018, Article ID 6412841, 9 pages, 2018.
- [29] Former State Bureau of coal industry, *Regulations for Coal Pillar Setting and Coal Pressure Mining in Buildings, Water Bodies, Railways and Main Tunnels*, Coal Industry Press, Beijing, China, 2000.